Effects of Metallic Coatings on Resistance Spot Weldability of Hot Stamping Steel

by

Osayande Ighodaro

A thesis
presented to the University of Waterloo
in fulfillment of the
thesis requirement for the degree of
Master of Applied Science
in
Mechanical and Mechatronics Engineering

Waterloo, Ontario, Canada, 2017

Author's Declaration

I hereby declare that I am the sole author of this thesis. This is a true copy of the thesis, including any required final revisions, as accepted by my examiners.

I understand that my thesis may be made electronically available to the public.

Abstract

Advanced high strength steels (AHSS) are being increasingly incorporated into automotive body structure to reduce vehicular weight without adversely affecting crashworthiness. Ultra-high strength steel (UHSS), a sub-set of AHSS, possess excellent anti-intrusion properties which make them very suitable for fabricating crash relevant automotive structures. The steel is usually coated as a necessary preparation for further processing. During resistance spot welding, the principal joining method for body-in-white automotive structures, the contact resistance, which is principally determined by the properties of the coating, play key role in defining welding parameters, thermal profiles, microstructure and eventually, sometimes, mechanical properties of the joint.

In this work, the contact resistance associated with AlSi and galvannealed coatings on Usibor 1500 hot stamping steel were determined using their dynamic resistance profiles. The results showed significant differences in the contact resistance values associated with the different coatings, and the trend in these values represented trends in current requirements for attaining acceptable nuggets sizes during resistance spot welding. Although peak load for tensile shear loading in static mode was similar for the AlSi and galvannealed coated sheets, there were significant differences in failure mode transition characteristics and energy absorption capabilities associated with the different coatings. Moreover, it was found that joints formed from dissimilar combinations of AlSi and galvannealed coated sheets exhibited poorer mechanical properties than either of AlSi or galvannealed coated sheets.

Acknowledgements

I would like to acknowledge and thank my supervisor, Prof. Norman Zhou for his time, efforts and support in guiding me through the journey in this research. I would also like to thank Dr. Elliot Biro for the regular monthly meetings and other times of contact, through which I was helped to stay on track. Members of the steel research in particular and the entire members of CAMJ group are also appreciated for all the fruitful discussions.

Many of the activities involved in this work required the assistance of some technical staff in the Mechanical and Mechatronics Engineering Department, and I am indeed grateful to Mark Griffith in the Materials Testing Laboratory, Jorge in the Engineering Machine Shop and Dr. Yiquan Ding in the Electron Microscopy Laboratory.

I am grateful to Professor Mike Worswick of the Department of Mechanical and Mechatronics Engineering for giving me access to the hot-stamping facility, and to Eckert Budziareck, Andy Barber, Neil Griffith and a host of other technical staff for their unflinching support in diverse ways.

I also acknowledged and appreciate financial support from Natural Science and Engineering Research Council of Canada (NSERC) and ArcelorMittal.

Table of Contents

List of Figures

List of Tables

1 Introduction

1.1 Background

Light weighting has been a requirement in the automotive industry in recent times, in response to the need for enhancement of fuel efficiency of vehicles and reduction in CO_2 emission, while maintaining crashworthiness, for the safety of occupants in the event of a crash. These requirements have motivated the rapid development of advanced strength steels (AHSS) and enhancement of joining and forming technologies. AHSS for automotive body-in-white construction is advantageous due to their high strength and excellent formability, which enables the use of thinner gauges for achieving the required performance. For crash relevant structures needed for anti-intrusion applications such as A-pillars, bumpers and reinforcements, ultra-high strength steel (UHSS) are required (1, 2). However, as strength increases formability decreases, i.e., more demand on forming pressure and dies. The use of hot stamping steel (or hot press forming steel) is one way of addressing formability of UHSS.

Hot stamping steels are formed at high temperature, when they are relatively soft and have low strength. Due to the high temperature treatment they are coated to prevent them from oxidation and decarburization. However, the choice of coating is very important because it moderates the chemistry of the steel substrate (3, 4) and affects weldability of the steel.

Weldability is one of the key parameters for selection of steels in the automotive industry since material joining is one of the major manufacturing processes. Resistance spot welding (RSW) is widely used during body-in-white (BIW) assembly of automobiles (5-8), and one of the parameters governing RSW is the total resistance of the sheet stack, which is significantly influenced by the coating.

Usibor® 1500, a hot stamping UHSS, is commercially available in aluminum-silicon (AlSi) based coating as well in Zn based, i.e. galvanized (GI) and galvannealed (GA) coating systems (9, 10). These coatings impart different characteristics on sheets coated with them. Moreover, it is inevitable not to join sheets having dissimilar coatings. However, there has not been found any report comparing the influence of these coatings on mechanical performance of the weldment of a given substrate. This is the motivation for this work, which studies the influence of AlSi and GA coatings on the properties of hot stamping steel, Usibor® 1500, resistance spot welded joint.

1.2 Research objective

The objective of the research work reported here is the study of the influence of AlSi and GA coatings on the weldability and mechanical performance of resistance spot welded hot stamping steel, Usibor® 1500. To achieve this objective the following tasks were performed.

1. Development of a method, based on dynamic resistance analyses, for quantifying the values of electrical resistance associated with key position/components in the sheet stack during RSW as influenced by the coating.
2. Investigation of comparative effects of coating type on the microstructure and mechanical performance of the resistant spot welded hot stamping steel.
3. Investigation of the weldability and properties of resistance spot welded joint formed using dissimilar combination of AlSi and GA coated Usibor® 1500 sheets.

1.3 Significance of this study

The work presented in this thesis is focused on gaining deeper understanding of the effects of AlSi and GA coating on resistance spot welded hot-stamping steel. The major direct benefits derivable from the results are as follows:

1. The welding community in general will be more knowledgeable and proficient in designing for welded structures and the practice of welding, especially welding of coated steels with high martensite content.
2. The results from this work can be implemented by the steel industry in compounding and improving the chemistry for steel manufacturing.
3. The primary users of Usibor, the automotive industries, will find the results from this work helpful for increasing the content of UHSS in vehicle design and construction, thereby promoting the realization of the concept of the future steel vehicle.

1.4 Report outline

This report is structured into five chapters and the reference section. Chapter 1 is the introduction, where the background information is presented, including the importance of this work, the objective and scope of the research.

In chapter 2, an extensive literature is presented, including an overview of advanced high strength steels (AHSS), with special emphases given to hot stamping steels. This chapter also covers effects of alloying elements on properties of base material, coating of steels, coating application methods and influence of coating type on substrate chemistry. It is concluded with discussions on the principle of resistance spot welding, effects of parameter selection on welded steel microstructure and dynamic resistance data interpretation and utilization. Chapter 3 is devoted to experimental details, characterization and data analyses methods. In chapter 4, the results and discussions of experimental works are presented, and finally in chapter 5, the conclusion, summary and recommendations for future work are presented.

2 Literature Review

2.1 Interaction of coating with welding processes

Coating of automotive sheet steel is advantageous for protection against corrosion and oxidation. For hot stamping steels coating is also a more cost effective option for protecting against decarburization and scaling (11, 12). However, during further processing of the coated sheet some other effects may arise. One such situation is the occurrence of liquid metal embrittlement (LME) of steel during welding of zinc coated steel (11, 13, 14). LME can occur when steel is subjected to tensile load at high temperature, in the presence of liquid zinc; these factors are simultaneously present during welding, especially resistance spot welding (RSW). Although LME normally may not be detrimental to the strength of RSW joint, the cracks generated degrade the aesthetic quality of the joint and are undesirable (15, 16).

During RSW of Zn coated steel, interaction of Zn with the Cu electrode caps causes degradation of electrode tip life (17-19), by alloying with the Cu electrode, and forming brittle brass which eventually chips off from the cap, making the electrode face to increase. This results in reduction in current density and nugget size, and the need to redress the tip at accelerated rate.

In the case of AlSi, studies from laser welded AlSi coated 22MnB5 showed that without ablation, the joints were weak when welded to itself (20) or carbon steel (21). However, when the coating was ablated before laser welding, there were no issues with weld quality (22). In a case of gas tungsten arc (GTA) welded ferritic stainless steel 409L, increase in fusion zone hardness was reported (23).

Coatings interact with welding processes, and the interaction may manifest in various ways such as alteration of welding parameters, weld quality, weld performance, etc., and the manner of interaction between substrate and coating is unique. Therefore, for a given substrate, different coatings could shift quality and performance significantly. This thesis is focused on acquiring fundamental understanding of the characteristics and performance of resistant spot welded hot stamping steel, as influenced by galvannealed and AlSi coatings.

2.2 Hot stamping steel

The manufacturing of light weight vehicles with the dual aim of reducing fuel consumption thereby reducing emissions to the environment and improving crashworthiness/safety relies strongly on the use of advanced high strength steels (AHSS). Conventionally, steels having yield strength between 210-550 MPa are designated as high strength steels (HSS) while higher strengths are designated as advanced high strength steels (AHSS), some of which are dual phase (DP) steel, Transformation Induced Plasticity (TRIP) steel, martensitic steel (MS), etc. (24). Figure 2-1 shows a spectrum of current AHSS. These steels are strengthened by various strengthening mechanisms and are characterized by multiple phases, which enable them to exhibit good combination of high strength and formability. However, as strength increases, formability becomes more difficult because forming load also increases, and dimensional accuracy tends to reduce due to spring-back effect.

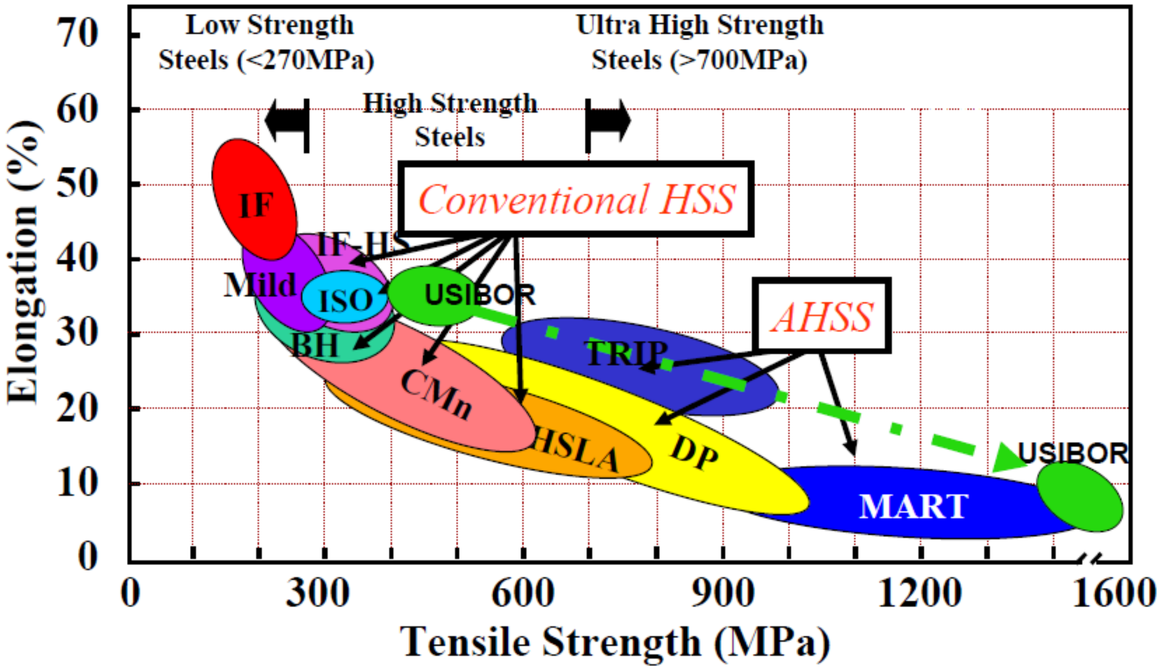

Figure 2-1   Spectrum of Automotive sheet steel (24)

A sub category of AHSS is the ultra-high strength steels (UHSS). Although there is no specific definition for UHSS, steels having yield strength higher than 560 MPa or tensile strength higher than 700 MPa are generally regarded as UHSS (24, 25) Usibor® 1500 (henceforth referred to as Usibor) is an ultra-high strength steel grade 22MnB5, and is the most commonly used steel grade for hot stamping (25, 26). In as-received (AR) condition the microstructure is a mixture of pearlite and ferrite, which is relatively soft, but after hot stamping it is transformed to martensite, which is a much harder and stronger material. Figure 2-2 shows some structural members currently being produced or are candidates to be produced from UHSS: bumper beams, door intrusion beams, roof and side rails, door beam and A-and B- pillars (24, 26, 27).

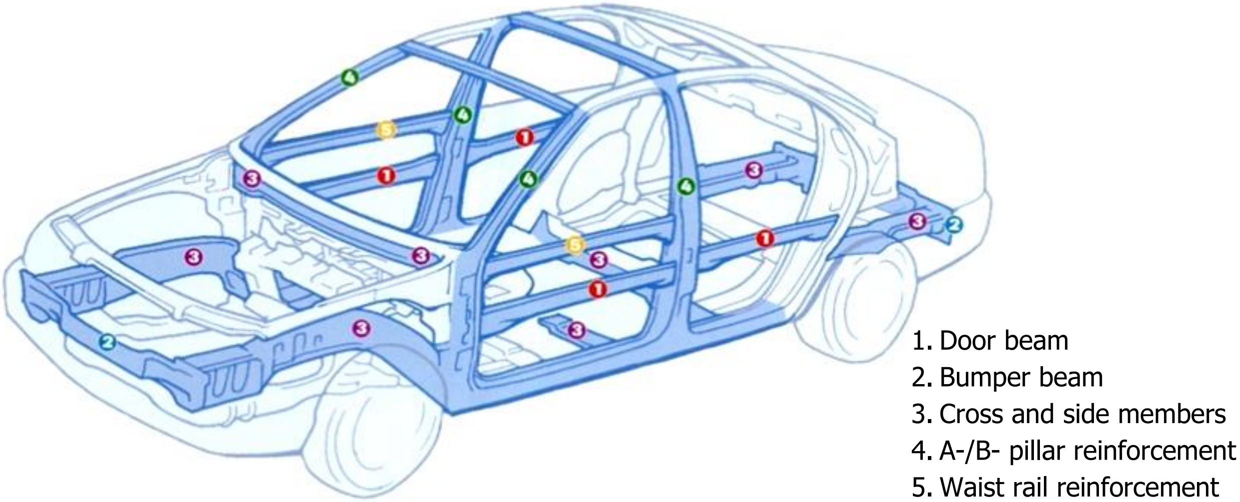

Figure 2-2 Ultra high strength steel structural components in a car body (27)

2.2.1 Hot stamping process

Hot stamping (also called press hardening) is conventionally used for producing ultra-high strength steels from hardenable steels grades. There are generally two types of hot stamping: direct and indirect hot stamping. In the direct hot stamping process the steel blank is heated to austenitization temperature (between 880°C – 930°C) and soaking for between 4-10 minutes. At this state, the steel is soft, with a low yield strength of about 200 MPa (10, 28). It is now quickly transferred into a die and formed into the desired shape and quenched to room temperature simultaneously at a rate above the critical quenching rate. This process transforms the soft microstructure to hard and fully martensitic microstructure. In contrast, during indirect hot stamping, the blank is first cold drawn to approximately 90 – 95% of the final shape before heating to austenization and finally quenching in a die to the final shape and hardened state. Due to the low yield strength at austenitization, forming load is low and spring back is reduced or eliminated, resulting in improved formability. Figure 2-3 shows sketches of the different hot stamping processes.

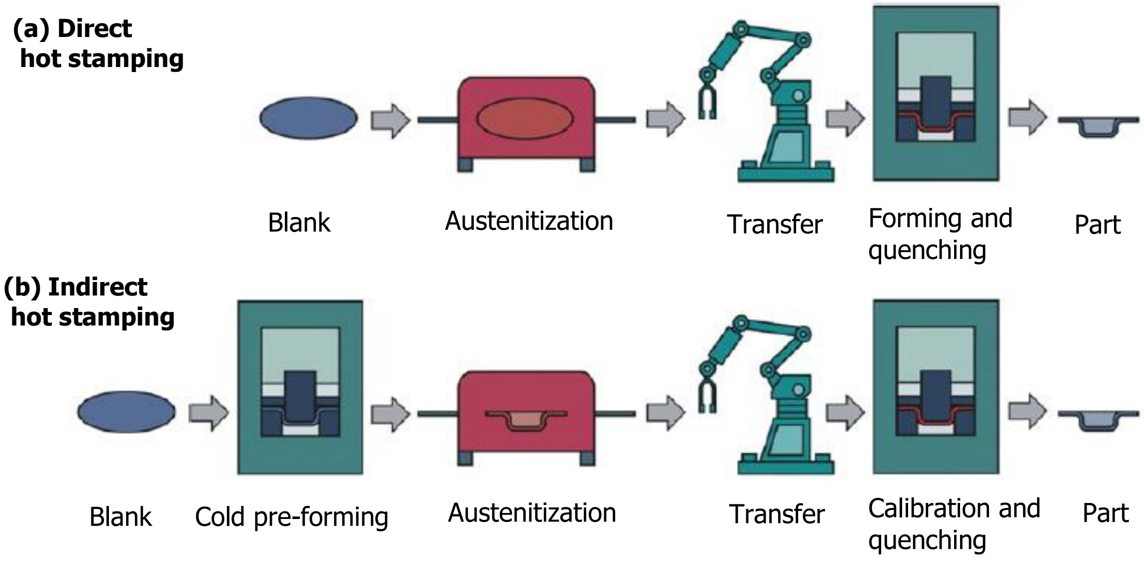

Figure 2-3 Basic hot stamping processes: (a) direct, (b) indirect (26)

The cooling rate is a key parameter governing hot stamping process because the final microstructure after quenching depends on it. Figure 2-4 shows the continuous cooling transformation (CCT) diagram for Usibor, including different cooling rates. For cooling rates greater than the critical (~ 27°C/sec. for Usibor) fully martensitic microstructure and the highest strength can be attained. For cooling rates less than the critical, other microstructures such as bainite, ferrite or pearlite may be obtained, which will result in lower strength but better ductility. Figure 2-5 shows a summary of the entire hot stamping process and Table 2-1 shows typical mechanical properties of Usibor in as received and hot stamped states.

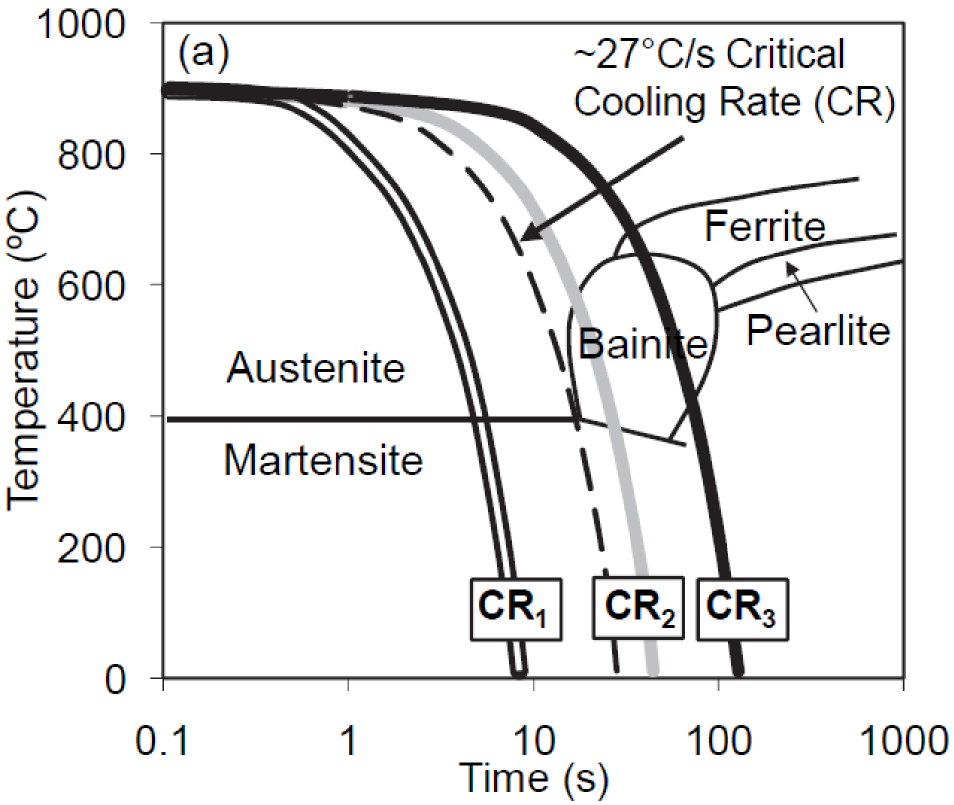

Figure 2-4 Continuous cooling transformation diagram for Usibor including 3 different cooling rates CR_1, CR_2 and CR_3. (29)

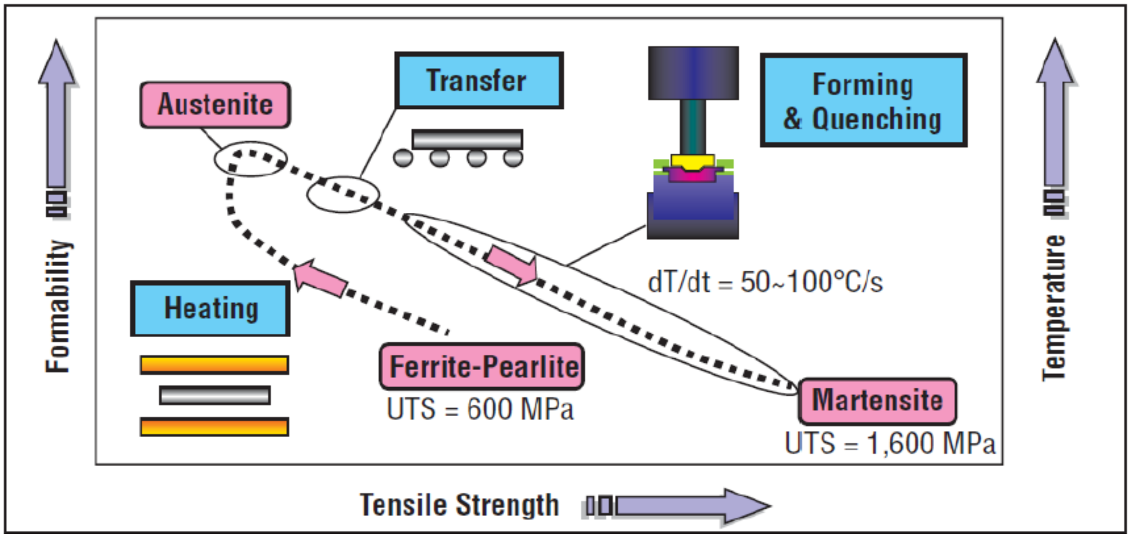

Figure 2-5 Change in tensile strength and microstructure during hot stamping (30)

Table 2-1 Typical mechanical properties of Usibor

	YS (MPa)	UTS (MPa)	Elongation (%)
As-received	400	600	25 (ISO)
Hot stamped	1000	1500	6 (ISO)

Aside from cooling rate, hardenability of hot formed steels also depends on the alloying elements. Usibor (also called boron steel) typically contains between 0.002-0.005 percent boron. It is known that boron is the most potent hardenability agent (26, 31), and addition of 0.003% gives a hardenability increase equivalent to 0.6% Mn, 0.7% of Cr, 0.5% of Mo and 1.5% of Ni (25). The effect and functions of other alloying elements will be discussed next.

2.3 Effects of alloying elements in steels

Alloying elements are incorporated into steel to control properties and performance of interest. The effects of these elements will be highlighted with respect to AHSS.

Carbon – The major hardening element in steel. For up to about 0.85 wt % C, hardness and tensile strength increases but ductility and weldability decrease. Too low carbon content may result in formation of ferrite, so carbon and other alloying elements are used (32).

Manganese – A moderate hardenability agent which increases strength in ferrite, but the increases is dependent upon carbon content. Mn tends to segregate, promotes variations in hardness and microstructure, and may form inclusions that are detrimental to toughness (32). Increasing Mn content decrease weldability and ductility.

Phosphorus – This element (just as sulphur) occurs naturally (or unintentionally) in steel. It is a very potent hardenability and strengthening agent, but detrimental to plasticity (33). It also offers some corrosion resistance.

Silicon – Principally a deoxidizer, moderate hardenability agent and effectively enhances strength and hardness of ferrite. Si also increases strength in quenched and tempered steels and pearlitic steels where added plasticity is not sought (33, 34).

Copper – Copper does not interact with carbon: the two elements are essentially immiscible. Therefore, all copper in mild steels will be dissolved or precipitated in ferrite, resulting in a slight hardening effect. Addition of Cu in combination with Ni is used to enhance galvanizability of Si-Mn steels (35).

Nickel – Significantly enhances toughness of ferrite in tempered steel. It also strengthens ferrite and increases hardenability and impact strength (33, 36).

Chromium – Mainly added to increase corrosion and oxidation resistance. Cr also increases hardenability but gives the least hardness increase in ferrite (33, 34, 37).

Aluminum – Excellent deoxidizer. Al is also used to effectively control austenite grain growth by forming fine dispersions with oxygen (or nitrogen) (33).

Niobium – Principally added for grain refinement by retarding recrystallization of austenite, thereby increasing yield strength and toughness (38).

Molybdenum – A very potent hardenability agent. Mo may produce secondary hardening during tempering of quenched steel, depending on tempering conditions and composition (31, 33).

Vanadium – A very potent grain refiner by elevating austenite coarsening temperature. Vanadium enhances strength and is a deoxidizer. It is also a very potent hardenability agent and exhibits high resistance to softening during tempering (31, 33).

Zirconium – Used for improving inclusion characteristics. Zr causes sulphide inclusions to be globular rather than elongated. It refines the grains and also enhances hardness (39).

Titanium – Used for grain refinement and improvement of inclusion characteristics. Similar to Zr, Ti causes sulphide inclusions to be globular rather than elongated and enhances impact toughness. It reduces hardenability and also functions as a deoxidizer (40)

Boron – The most potent hardenability agent, used in very little quantities (ppm) for the sole purpose of hardenability (32).

Nitrogen – Principally used for forming nitride inclusions (by combining with Al, Ti, V, and other nitride forming elements), which are finely dispersed in the matrix to restrict austenite grain growth and coarsening (31).

The choice of alloying composition for automotive steels is mainly made for the purpose of attaining predetermined mechanical properties. However, because automotive steels are usually coated, the choice of coating is also factored into the alloy design stage in order to avoid property degradation either in service or during further processing. This means that the choice of coating significantly affects the choice of substrate alloying chemistry.

2.4 Coating application

Coating of automotive steels serves primarily for protection against corrosion and oxidation. It also assists paintability for exposed auto body parts (41). Coating is done commercially by passing the substrate through a bath of molten metal in a continuous flow layout. Prior to entry into the coating bath the cold rolled sheet steel must be thoroughly cleaned of residual oil film and other impurities to ensure that the coating adheres perfectly to the steel surface. It is then taken through the annealing process to recrystallize and generate the microstructure required to meet the expected mechanical properties, before entering the coating bath. Figure 2-6 shows a sketch of the Sendzimir-type continuous coating line (CCL) used in industry (41, 42). On the

CCL all processes related to coating, such as cleaning, degreasing, annealing, hot-dipping, thickness quality control and final inspection and coiling are carried out in a continuous flow fashion.

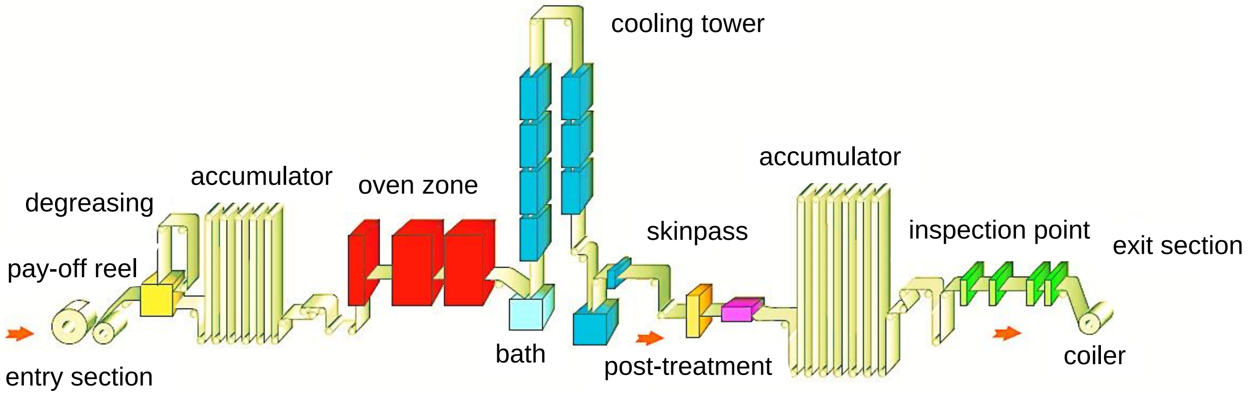

Figure 2-6 Diagram of Sendzimir-type hot dip continuous coating line (CCL) (42)

Annealing is a highly controlled process involving carefully designed heat treatment; it includes heating and holding at specified temperatures, and controlled cooling, as dictated by the required final microstructure. Although the annealing is carried out in a reducing chamber (usually charged with a mixture of hydrogen-nitrogen gas), the medium unavoidably contains a small concentration of oxygen and water vapor. Oxidation of elements such as Mn, Si, Cr and Al, that have higher affinity for oxygen than iron, form oxides on the surface of the steel substrate. (43, 44). This could cause poor wetting of the substrate during hot dip and result in bare spots and other surface defects. Moreover, the chemistry of the coating determines its adhesion to the steel surface, in the presence of the generated surface oxides. Therefore, the annealing process is controlled specifically to conform to the requirement of the intended coating as regards wettability and adhesion. In attempt to get rid of the surface oxidation the dew point of the annealing atmosphere could be controlled. For example, increasing the dew point causes oxygen permeability into the steel substrate to increase, and this results in transition from surface to internal selective oxidation (45). Internal oxidation has been known to degrade mechanical properties of steels; in particular, it causes low surface hardness and reduced strength. Internal oxides are also stress raiser, which are known to act as crack-initiation sites during fatigue loading (45, 46). Therefore, the susceptibility of the alloy composition of the substrate steel to selective internal or external oxidation must be considered, and alloy composition tailored in conformity with the coating, in order to avoid coating defects or degradation of mechanical properties. It can be inferred therefore that coating type influences mechanical properties of substrate since it influences substrate alloy composition and annealing specifications.

Usibor hot stamping steel is commercially available in galvanized (GI) and galvannealed (GA) coatings as well as aluminium-silicon (AlSi) coating. A brief discussion of these coatings and their application methods are presented next.

2.4.1 Hot dip galvanized coating

Zinc coating provides a two-fold protection against corrosion on steel. First is the barrier protection through the metallurgical bond with the steel surface which separates the steel from the corrosion environment. Secondly, galvanic protection is also provided under ambient conditions since Zn is less noble (i.e. more electronegative) than steel. In this case, the Zn coating will sacrificially corrode to protect the steel if the steel is exposed at a cut edge or the coating is scratched or cracked (4, 41).

Zn coating is carried out commercially by hot-dip galvanizing (HDG) process using the Sendzimir-type continuous galvanizing line shown in Figure 2-6. The steel surface needs to be completely clean for Zn to react metallurgically with it. Therefore the steel is first taken through degreasing, pickling and fluxing, after entry into the line. This is followed by annealing heat treatment. The substrate now enters the molten Zn bath maintained at between 445 and 455° C. The line speed is monitored to control the coating thickness. At the exit section of the coil from the bath, the coated stripe is stripped with air knifes and cooled to maintain the coat thickness and arrest further reaction between Zn and Fe. Other parameters that control coating thickness, morphology and quality are immersion temperature, coating bath chemistry as well as substrate alloy composition (47-49).

During immersion of the substrate into the Zn bath, various reactions between Fe and Zn occur, and on cooling, a heterogeneous assembly of different phases is bonded to the steel. The outermost layer (farthest from the substrate) is eta (η) phase; a solid solution of 0.03% Fe in pure Zn. The next is the zeta (ζ) phase, $FeZn_{13,}$ having Fe content of between 5-6 wt%, then the delta (δ) phase, $FeZn_{10}$, with Fe composition range between 7.0-11.5 wt%. The gamma (Γ) phase Fe_3Zn_{10} is the closest intermetallic layer to the steel substrate, having Fe content between 23.5-28 wt%. Figure 2-7 shows the microstructure of Zn coating formed on low carbon steel immersed at 450°C for 300 s.

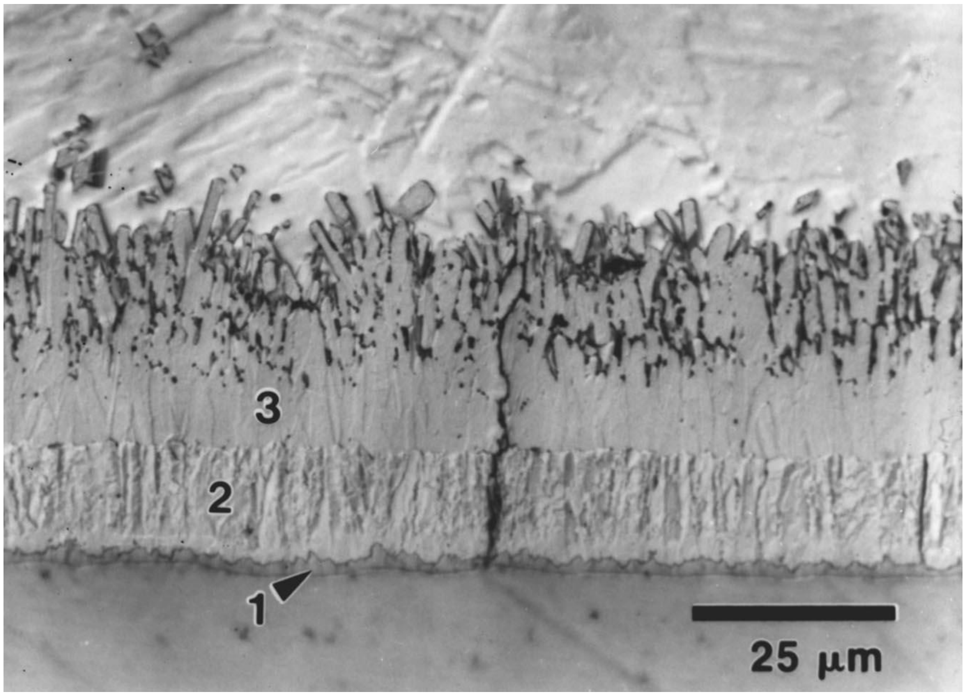

Figure 2-7 Microstructure of Zn coating formed after 300 s immersion in a 450°C bath on ultra-low carbon steel substrate. (1) gamma (Γ) phase, (2) delta (δ) phase (3) zeta (ζ) phase (41)

Problems usually arise during galvanization of Si and Mn containing steel substrates, in that the coating thickness abnormally grows, making the steel not amenable to further processing (44). In order to improve some desired qualities of Zn coating, several other additives such as Al, Mg, Pb, Ni, etc. or a combination of elements are added to the Zn bath. In particular, low additions (< 1%) of Al to the Zn bath has been found to be most effective for obtaining a more ductile coating by suppressing the formation or size of the more brittle Fe-Zn phase through the formation of predominantly Fe_2Al_5 (and some $FeAl_3$) intermetallic layer called the inhibition layer (4, 41, 47, 50, 51). In practice, 0.1 – 0.3 wt% (typically 0.2 wt%) Al is added to Zn galvanizing baths to enhance coating quality (4, 41, 47, 52). To further enhance coating quality the galvanized sheet may be subjected to annealing process to produce galvannealed (GA) sheet.

2.4.2 Galvannealing

Galvannealing is the process of subjecting galvanized (GI) steel to annealing at a temperature around 500°C to produce fully alloyed Fe-Zn intermetallic phases. The coating bath typically contains between 0.12 to 0.14% dissolved Al (53). The galvannealed (GA) coating exhibits superior corrosion resistance, improved paintability and weldability than the GI. (54, 55). GA coatings could be described as (55):

- Type 0 – which is under alloyed coating composed predominantly of zeta (ζ) phase.
- Type 1 – the optimum alloyed coating having less than 1µm gamma (Γ) layer and an overlay of delta (δ) phase interspersed with small amounts of zeta (ζ) phase.
- Type 2 – which is overalloyed coating having a gamma layer more than 1 µm thick and an overlay containing delta (δ) phase with basal plane cracks perpendicular to the coating/substrate interface and an occasional top layer of zeta phase.

Figure 2-8 shows the various types (0, 1and 2) of coating obtainable in a galvannealing process. Processing variables, coating bath and substrate chemistries are usually adjusted to attain type 1 coating, which gives the best formability, paintability and weldability (55, 56).

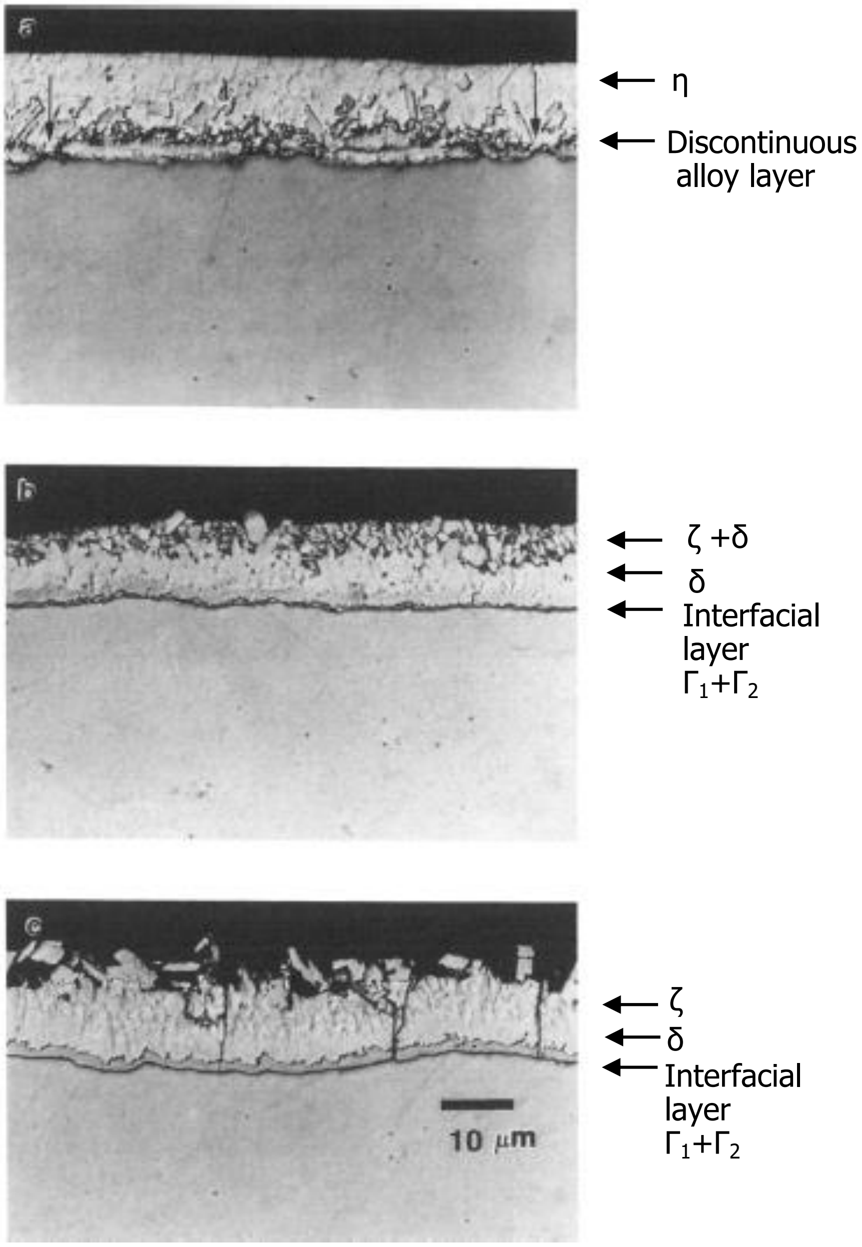

Figure 2-8 SEM images of (a) type 0, (b) type 1, and (c) type 2 GA coatings (55)

2.4.3 Aluminium-silicon coating

Aluminium coating treatment (aluminizing) is a well-known practice for protecting steel against oxidation and decarburization at high temperature. Formation and growth of Fe-Al diffusion layer, comprised of high temperature intermetallic phases adjacent to the steel substrate prevents the substrate from further reaction. This is “type 2” aluminized coating; the coating bath consists of pure Al (10). However, due to the rapid rate of reaction between Al and Fe, the rapid growth of Fe_2Al_5 intermetallic compound, which is inherently hard and brittle, causes the thickness of this diffusion layer to increase rapidly. Thick and brittle intermetallic layer hinders forming and bending operations which sheet steels are usually subjected to (57). Studies have shown that Si addition to Al coating bath retards the formation and growth of the intermetallics by forming a thin Fe-Al-Si barrier layer on the steel surface (58). Thus AlSi coating is a widespread high temperature resistant coating applied on hot press forming (HPF) steels. They are applied by hot-dipping (hot dip aluminizing), just as galvanizing, and they provide equivalent corrosion resistance under normal operating conditions. It has been shown that the temperature of the coating bath does not have significant effect on the alloy layer thickness, and Si concentration between about 6–11 wt% yield similar effect on thickness reduction (58). Thus, “type 1” aluminized coatings are formulated near the eutectic composition; usually around 7-11 wt% Si. However, industrial formulation for HPF steel coatings consists of around 87% Al, 10% Si and 3% Fe (10, 26). Si in the coating bath also promotes the development of a flat substrate/ interface layer, enhance coating adhesion and elevated temperature oxidation resistance (57). Figure 2-9 shows a microstructure of as-coated “type 1” AlSi coating. It consists of a brittle intermetallic Al-Fe-Si layer adjacent to the steel substrate, over which pure AlSi is overlaid.

Whatever the coating system AlSi, GI or GA, during hot forming of the steel, the coating also undergoes significant microstructural and morphological changes. These changes set the properties that determine the ease (or parameters) for further processing of these coated sheets. Properties of immediate concern in this investigation are the electrical resistivities and thermal properties, and their effect on properties of the RSW joint.

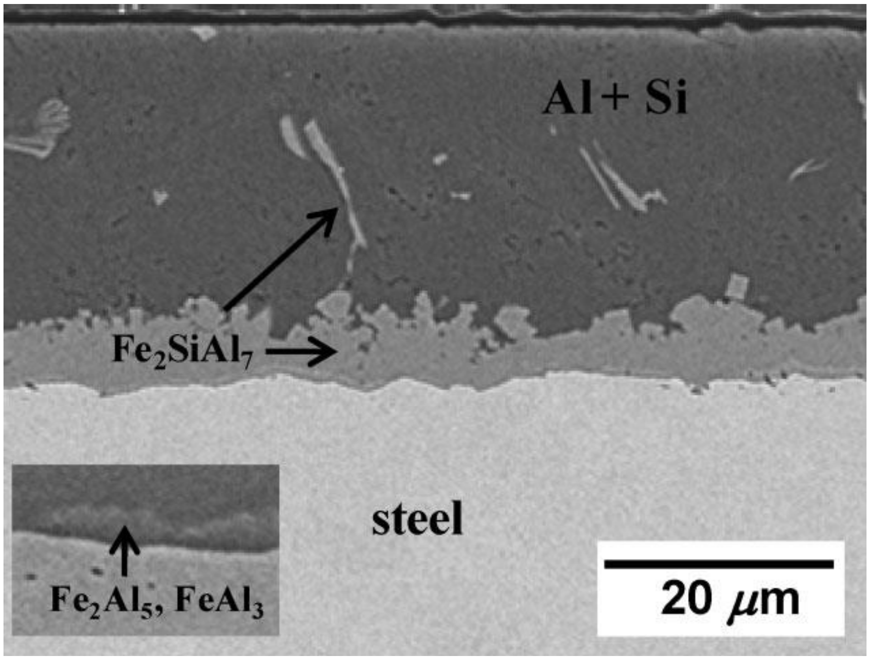

Figure 2-9 Cross-sectional SEM of a type 1 aluminized coating (10)

2.5 Resistance spot welding

Resistance spot welding (RSW) is an assembly/joining process used in many industrial sectors such as energy, shipbuilding, aerospace and automotive. It was invented by Elihu Thomson in 1877 (59), and is now the major sheet metal joining process in the automotive industry (other methods are laser beam welding-LBW and gas metal arc welding- GMAW). Most modern automobile body-in-white (BIW) structures contain between about 2300 to over 6000 spot welds (59, 60), because of the advantages of RSW: low cost, high operating speed, suitability for automation, and does not require the use of consumables; such as filler wire or shielding gas (61).

2.5.1 Principle and process of resistance spot welding

RSW is based on Joule’s first law which gives an expression for the quantity of heat generated when an electric current flows through a resistive conductor according to the equation (neglecting heat losses) (62, 63)

$$Q = I^2.R.t, \quad \text{-----} \quad 2.1$$

where (Q) is the quantity of heat, I is the current, R is the resistance and t is the duration of the current. Figure 2-10 shows the basic set up for RSW. In the simplest form, two metal sheets are clamped between two (water cooled) electrodes, current flows through the electrodes across the sheets, generating enough heat to melt the sheets at their faying interface to produce a molten weld pool. As soon as current stops flowing, the weld pool solidifies rapidly, forming a nugget (the size of which increases with welding time) that permanently joins the sheets together.

According to Eqn. 2.1, the electrical resistance of the sheet stack-up is a factor for heat generation. From the set-up shown in Figure 2-10 various resistances are involved. R_2 and R_4 are the bulk resistances of the substrate metal sheets to be welded, R_1 and R_5 are contact resistances at the electrode/sheet (e/s) interface, R_3 is the contact resistance at the sheet/sheet (s/s) interface. The total electrical resistance is the sum of the contributions from all these resistance components. However, Figure 2-10 is representative for welding of bare (i.e. uncoated sheets). Figure 2-11 is a sketch of an expanded view of the sheet stack, highlighting the coating on the surface of the sheets. The coating is now the major contributor to the total resistance and determinant of the RSW parameters.

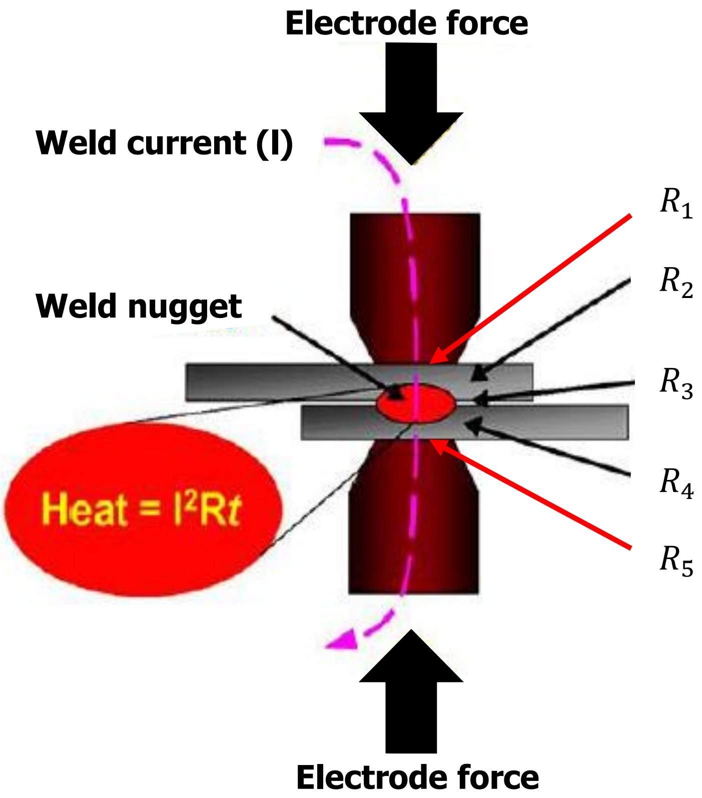

Figure 2-10 Schematic shows basic set-up for resistance spot welding. Adapted from (64)

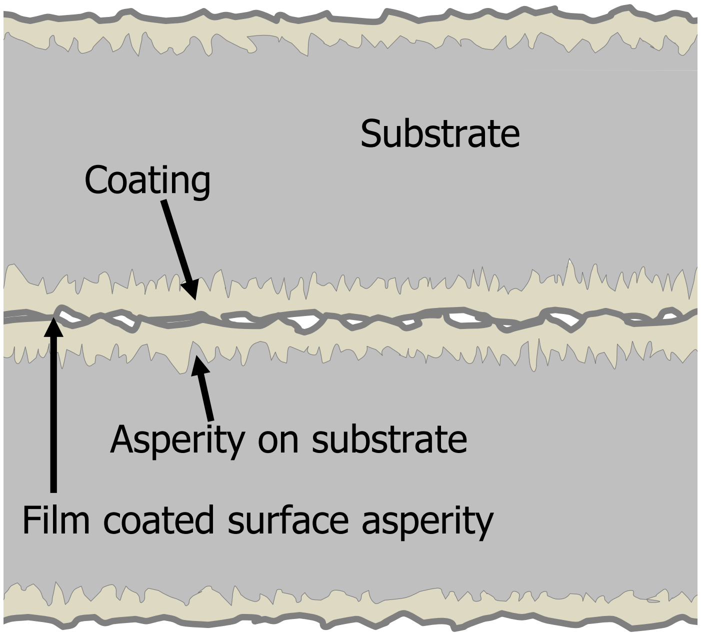

Figure 2-11 Sketch of sheet stack highlighting coating on surface

2.5.2 RSW process parameters

During RSW some parameters (weld force, squeeze time, weld time, hold time and off time) are controlled by the operator to achieve the desired weld quality.

Weld force – The weld force applied via the electrodes is necessary primarily to hold the sheets in intimate contact at the faying interface so as to ensure electrical conductivity across the sheets. The magnitude of the weld force affects the electrode/sheet (e/s) and sheet/sheet (s/s) contact resistances. Generally, low electrode force brings about low contact area between the surfaces, resulting in high contact resistance. Also, if weld force is too low expulsion of molten metal may occur before nugget grows to the full size. On the other hand, increasing the weld force causes more surface contact thereby reducing contact resistance. However, there exists a limiting force beyond which the contact resistance remains uniform (60, 65). If the weld force is too high for the set-up undesirably deep indentation (above 25% of sheet thickness (66)) may occur, and may generate regions of stress concentration. Moreover, unnecessary high welding force enhances electrode deformation, thereby reducing electrode life. Therefore, weld force should be properly chosen during RSW, even though it does not appear in Joule heating relation (Eqn. 2.1). Figure 2-12 shows an RSW time cycle. Weld force is applied from the beginning of the squeeze time to the end of hold-time.

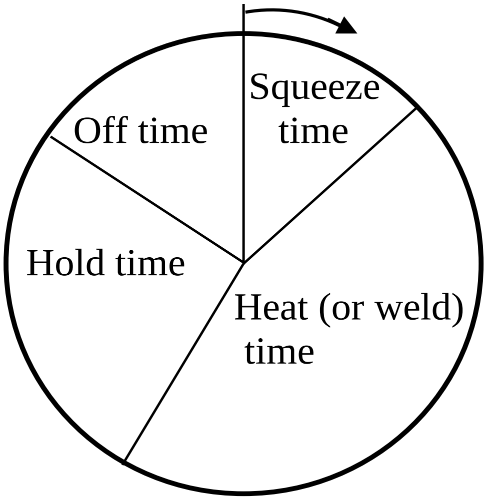

Figure 2-12 Basic RSW time cycle (67)

Squeeze time – During this time the electrodes clamp the sheets together to attain good electrical contact. Squeeze time should increases with thickness of the sheet-stack.

Heat time (or weld time) – This is the duration of current flow represented in Eqn. 2.1, and is measured in milliseconds (for direct current machines) or number of cycles (for alternating current machines). If heat time is insufficient, nugget may not be formed or may not attain the acceptable size. Excessive heat time may cause expulsion, excessive indentation, poor joint strength and shortened electrode life.

Hold time – When the weld time elapses, clamp pressure is maintained by the electrodes to give enough time for solidification of the molten nugget, enabling the joint to develop structural strength. Hold time determines the cooling rate and therefore determines the final hardness microstructure around the weld regions. Insufficient hold time could lead to unnecessary porosity in the nugget.

Off time – This is the time for the electrodes to release the workpiece, return to their home position, and ready for the next cycle.

2.5.3 Weld lobe

Weld quality is usually controlled by using a selected combination of welding parameter, and every set of materials to be welded has a range of parameter sets with which acceptable welds can be obtained. These parameter sets are enclosed in a weld lobe diagram, which is usually constructed using the current – time domain at a fixed force level. A sketch of a weld lobe diagram is shown in Figure 2-13. Knowledge of the weld lobe for a set of materials allows the use of different weld parameter within the lobe for attaining similar weld quality. The width of the lobe curve at a given time value shows the permissible welding current range. The wider the current range and the larger the area enclosed by the boundaries of the weld lobe, the more desirable because of the greater ease of producing acceptable welds based on the wide range of possible parameter combinations.

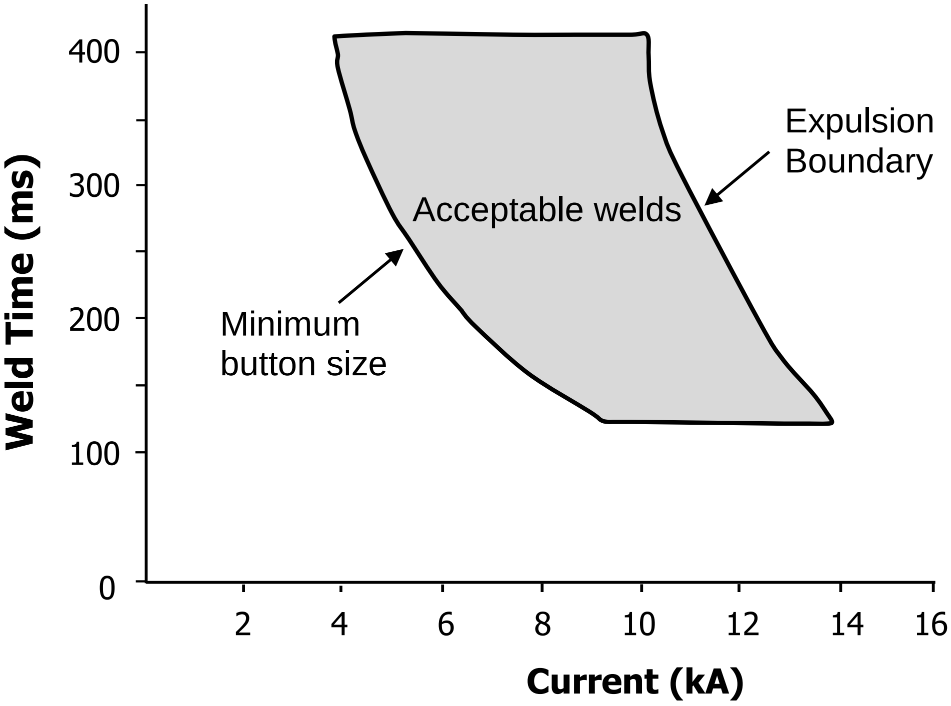

Figure 2-13 Schematic of a weld lobe diagram

2.6 Resistance spot weldability

Weldability is a critical criterion for selection of automotive steels, and resistance spot weldability is conventionally evaluated using three criteria: physical and metallurgical attributes, mechanical performance and failure mode (62, 68). Figure 2-14 shows basic features of a resistance spot weld, for illustration of the discussions that follow.

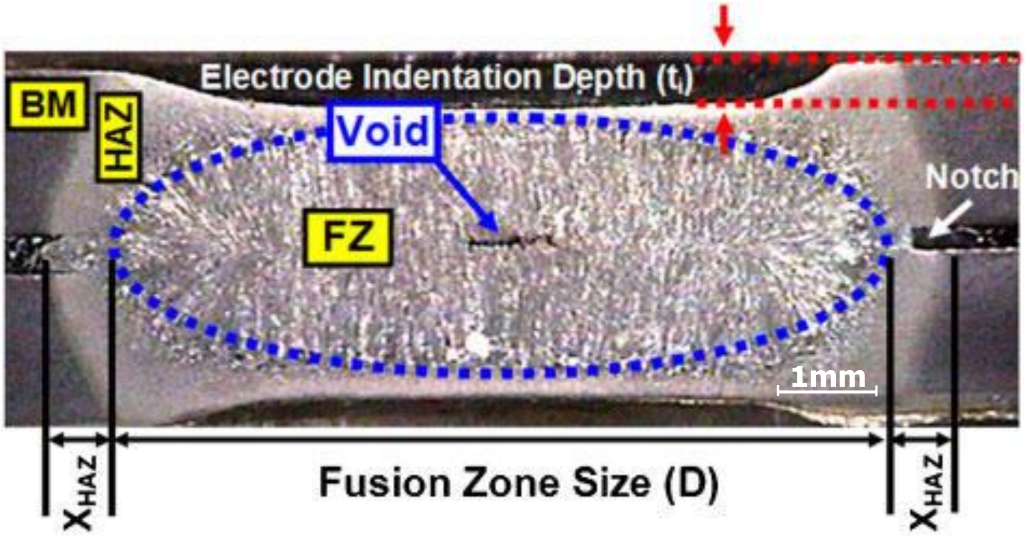

Figure 2-14 Features of a spot weld (69)

2.6.1 Physical and metallurgical attributes

Weld nugget or fusion zone size – This is the most important factor in determining the quality of a spot weld (69, 70). It is determined by the net heat input which in turn is governed by the selected welding parameters for a given material. The larger the nugget size, the higher the strength of the weld, therefore the better the weld quality and weldability for a given set of parameters and material.

Penetration depth – This is the width of the nugget in the sheet thickness direction. The requirements on penetration are usually very loose; ranging between 20 and 90% for various automotive and aerospace industries (62). Generally, high penetration depth is preferred provided it does not create large indentation.

Void in weld nugget – This arises from two sources: by expulsion or by solidification shrinkage (62, 68). The presence of voids increases the tendency of the weld to fail interfacially due to reduction in effective load bearing area. However, a high welding force prevents/ reduces formation of void.

Indentation depth – This is caused by the plunging of the electrodes, and depends on the weld force, heat input, electrode/sheet interface temperature and deformability of the material. It may affect mechanical properties, depending on the size since it causes stress concentration around the weld (71). The recommended practice by the American Welding Society (AWS) is that indentation depth should not exceed 25% of the sheet thickness (66).

Shape of the notch at the faying interface – Notch acts as a natural crack at the circumference of the nugget, the shape of the notch; sharp versus square can influence the failure behavior; sharp cracks are more likely to cause interfacial failures (71, 72)

HAZ size – The size of HAZ is determined by the net heat transfer by conduction from the fusion zone to its surroundings, and it affects the ductility of the welded joint.

Hardness of FZ and HAZ – This is controlled by weld thermal cycle as well as chemical composition and microstructure of BM (68).

2.6.2 Mechanical performance

Parameters for evaluating mechanical performance of spot welds are obtained through mechanical testing, which reveal important weld characteristics such as weld button size, weld strength or failure mode. Figure 2-15 shows a representative tensile-shear (TS) load-displacement curve of a spot weld. The product of load and the corresponding displacement is the energy absorption, and summation of energy from the origin to the peak load is equivalent to the area under the load-displacement curve, which equals the energy absorbed at failure. These parameters are used for quantitative analysis of weld mechanical performance, and high values are positive indicators of weldability.

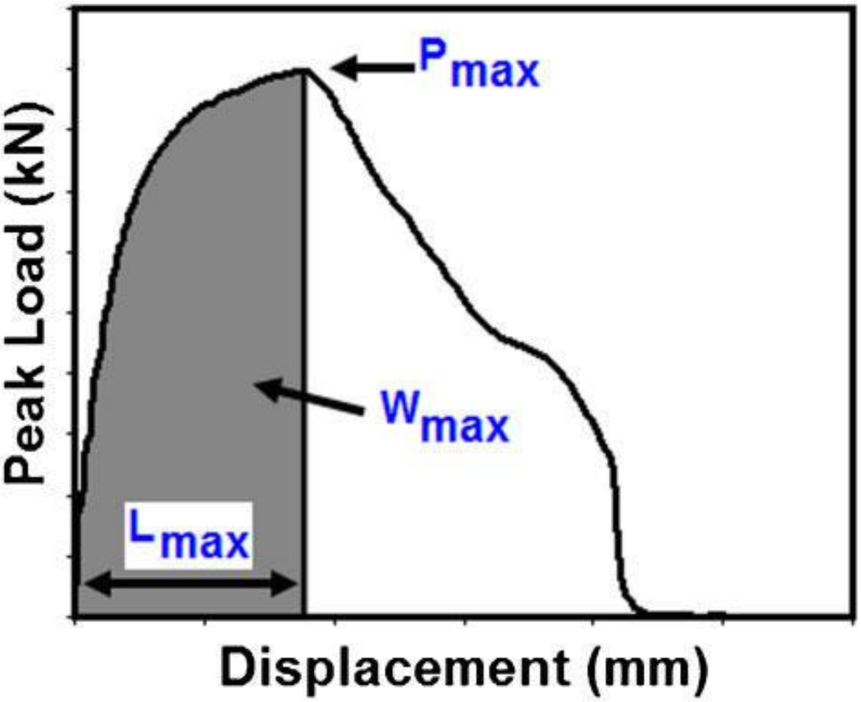

Figure 2-15 Typical load-displacement curve during TS test showing extracted parameters for evaluation of mechanical performance (69)

2.6.3 Failure mode

Failure mode is a qualitative measure of RSW joint quality in the manufacturing environment. Two extreme modes are identified as: pull-out (PO) and interfacial (IF) mode (73-76). However, in AHSS other non-traditional intermediaries between these extremes have been mentioned (68, 74, 77).

Interfacial (IF) mode – In this mode fracture propagates through the joint FZ, causing complete separation of the sheets. This failure mode is generally considered unfavorable for crashworthiness (73, 78, 79).

Pullout failure (PO) mode – This occurs when the nugget pulls out as a unit from the sheet. In this case, fracture propagates along the periphery of the weld, either the HAZ or BM, rather than through the FZ, and a button and hole are formed. Generally the PO failure mode exhibits more satisfactory mechanical behaviour, therefore it is often preferred (73, 80). Figure 2-16 shows a schematic representation of these failure modes.

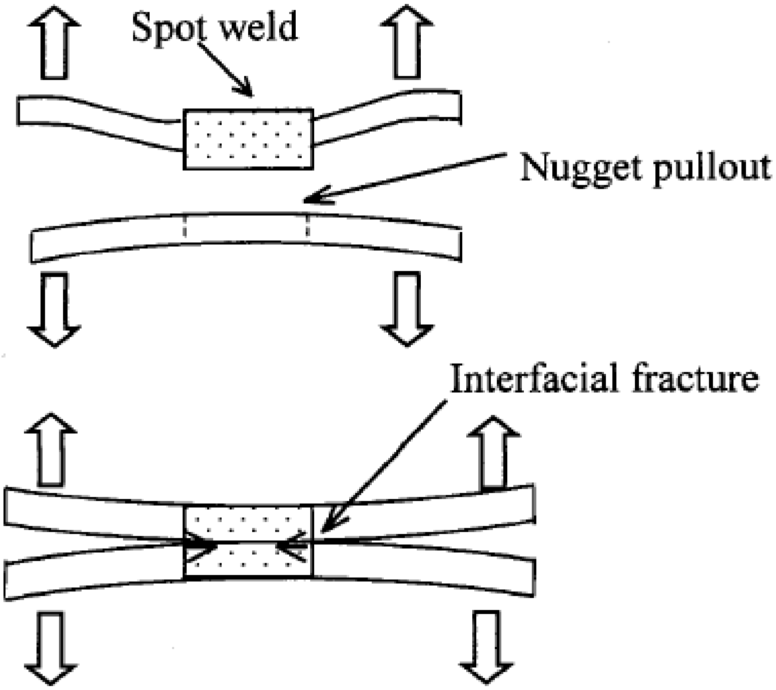

Figure 2-16 Schematics of failure modes of spot welds: pull-out and interfacial (79)

When a spot weld is under load there is usually competition between IF and PO failure modes, which are governed by the different mechanisms of tensile and shear forces. The eventual failure mode is determined by the condition that is met first. As a matter of standards, the American Welding Society (AWS), Society of Automotive Engineers (SAE) and the American

National Standards Institute (ANSI) (81) jointly recommend an empirically determined relation for computing critical nugget size required for transition from IF to PO failure mode given by $d = 4\sqrt{t}$, where d is the critical nugget size and t is the sheet thickness. Efforts have also been exercised to produce analytical versions of the relation between failure mode and weld/material attributes. Result from the work of Chao (79) shown in Figure 2-17 illustrates the trends of these two failure modes. In the equations, P_f is the failure load, τ_f is the shear fracture stress or shear strength of the heat affected zone and K_c is the fracture toughness of the nugget. It is seen that as the nugget increases in size, a critical value (called the critical size or critical diameter) is reached after which the failure mode transitions from IF to PO, and nugget sizes larger than this critical size continue in the PO failure mode. Generally, low critical nugget size is an indication of good weldability, but the higher the strength of the steel grade, the higher will be the critical nugget size.

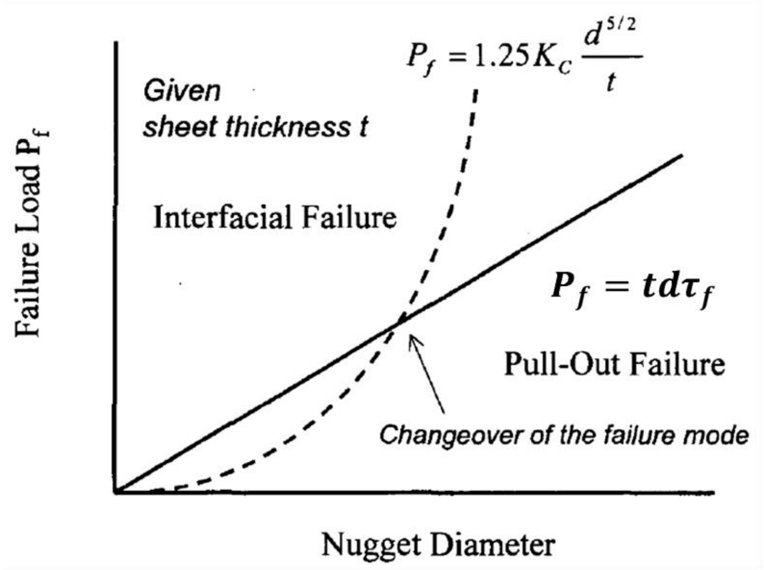

Figure 2-17 Schematic diagram showing competition between interfacial failure (broken line) and nugget pullout failure (solid line) (79)

2.7 Welding metallurgical transformations

The features of a spot weld were shown in Figure 2-14, and the physical attributes were discussed in section 2.6. This section is focused on the metallurgical attributes of the FZ and the HAZ of the spot weld. Firstly, the Fe-Fe_3C (iron-cementite) phase diagram shown in Figure 2-18 is introduced to aid this discussion.

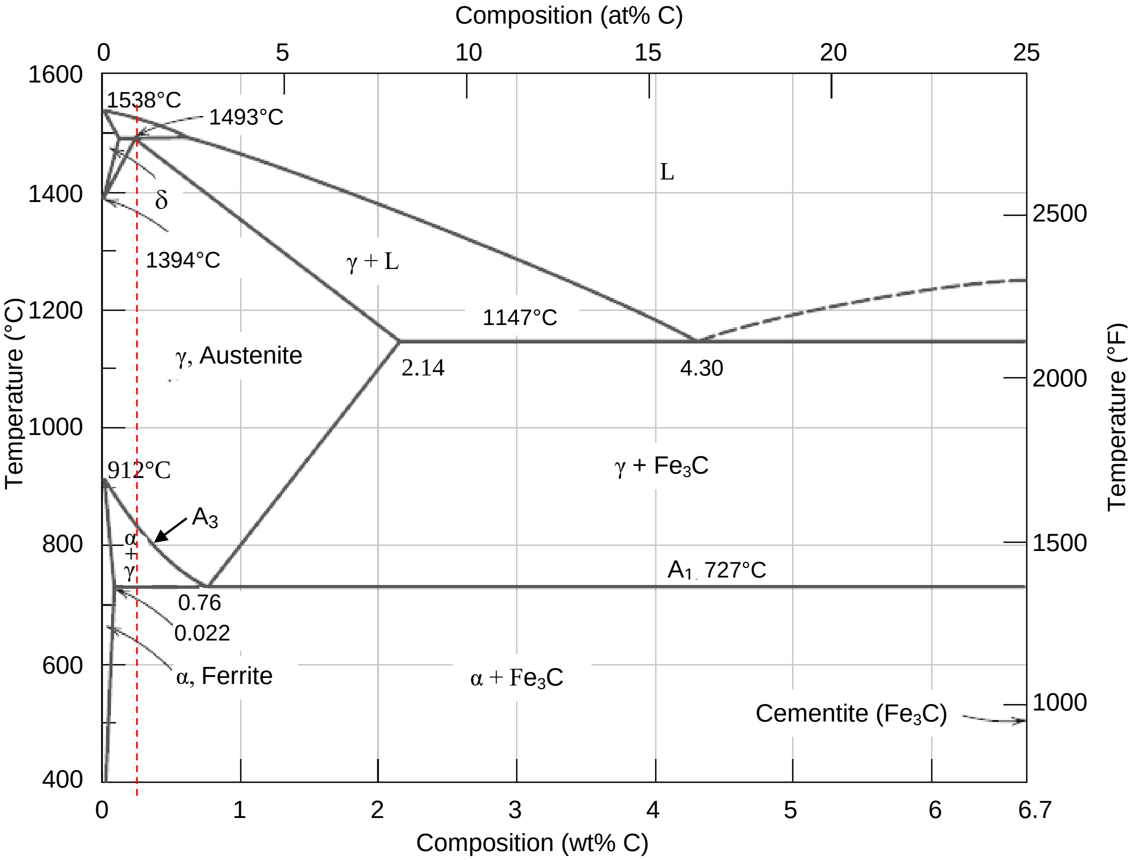

Figure 2-18 The Fe-Fe3C phase diagram (82)

Carbon composition in Usibor is approximately 0.23 wt%, and the position is shown by the broken vertical line on the phase equilibrium diagram of Figure 2-18, so that the phase of existence of Usibor at any temperature (within the temperature range shown) may be predicted. At room temperature steel normally exist as a mixture of ferrite, a body centered cubic (BCC) structure and cementite (Fe_3C). When Usibor or any hypoeutectoid steel (i.e. steel having less than 0.76 wt% C) is heated and the temperature increases beyond the eutectoid temperature, A_1 (= 727°C), the ferrite phase begins to transform to austenite phase, which has face centered cubic (FCC) structure. At the critical temperature A_3 transformation to austenite is complete, and beyond A_3 the steel remains completely austenite until melting begins and completes on further increase in temperature. The reverse is the case when the steel is cooled from the liquid state to room temperature under equilibrium conditions. However, during fast cooling, equilibrium is not achieved and the austenite does not have sufficient time to reject the excess carbon dissolved in the FCC structure. Therefore, instead of transforming to ferrite and cementite, some of the austenite could transform to martensite or bainite or both. During RSW, the very high cooling rate encountered usually completely transforms austenite to martensite.

Heat supply during RSW causes fusion at the FZ. However, due to the thermal conductivity of the metal sheet, areas surrounding FZ are heated up to varying temperatures. Therefore, different regions around the spot are subjected to different temperature histories, which can be captured in their temperature profiles. Figure 2-19 shows simulated temperature profiles across the FZ, HAZ and BM of a spot weld. As expected, the FZ attains the highest temperature, and the temperature diminishes across the HAZ, to the BM. This causes metallurgical changes across the weldment in proportion to their thermal profiles. Figure 2-20 shows an example of these metallurgical changes for hot stamping steel. It is obvious that different microstructures now exist at different sections of the weldment, and these microstructures exhibit different properties, such as hardness and strength accordingly.

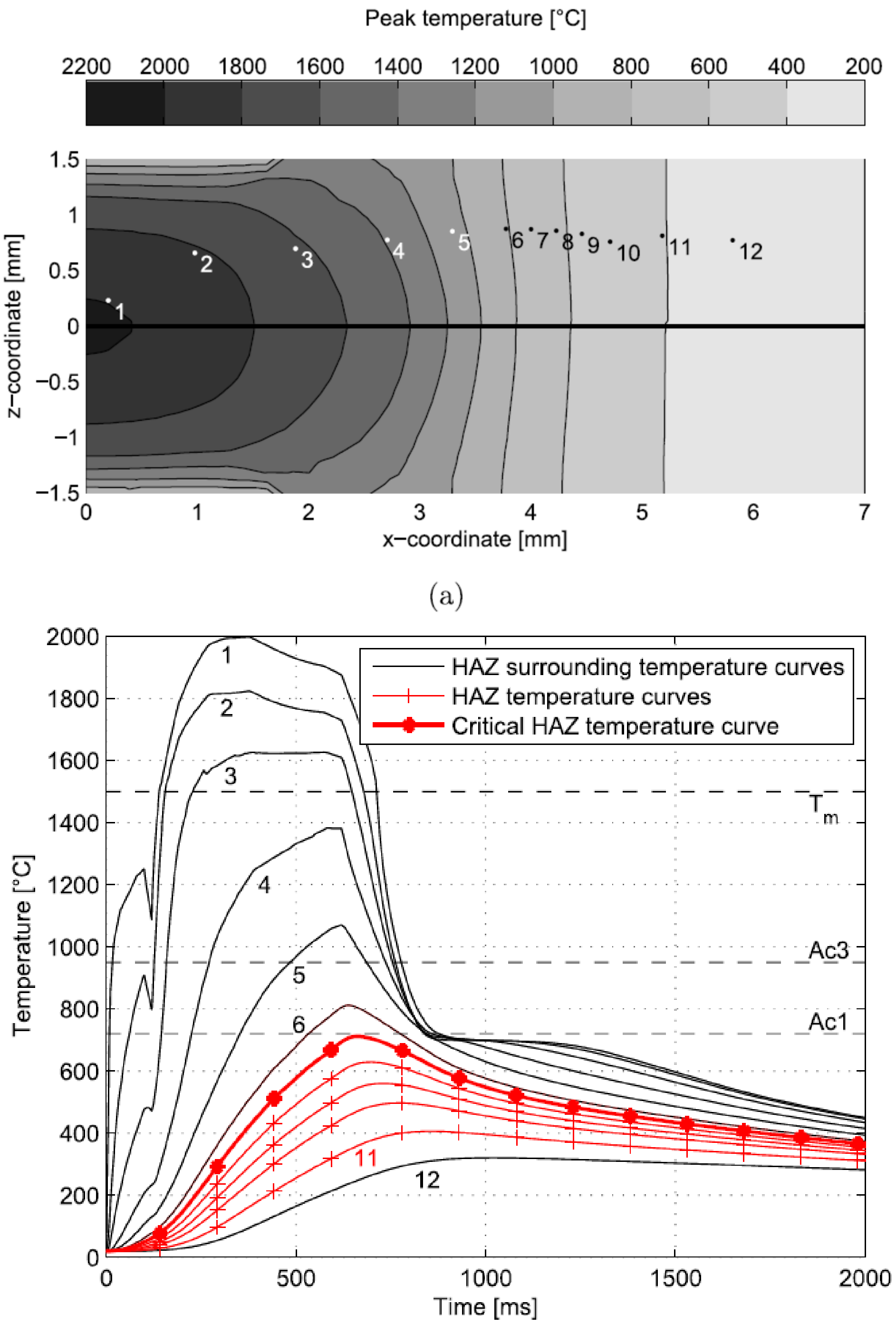

(a)

(b)

Figure 2-19 SORPAS® simulation results: predicted peak temperatures in the weld area (a) and temperature curves at selected locations (b) (83)

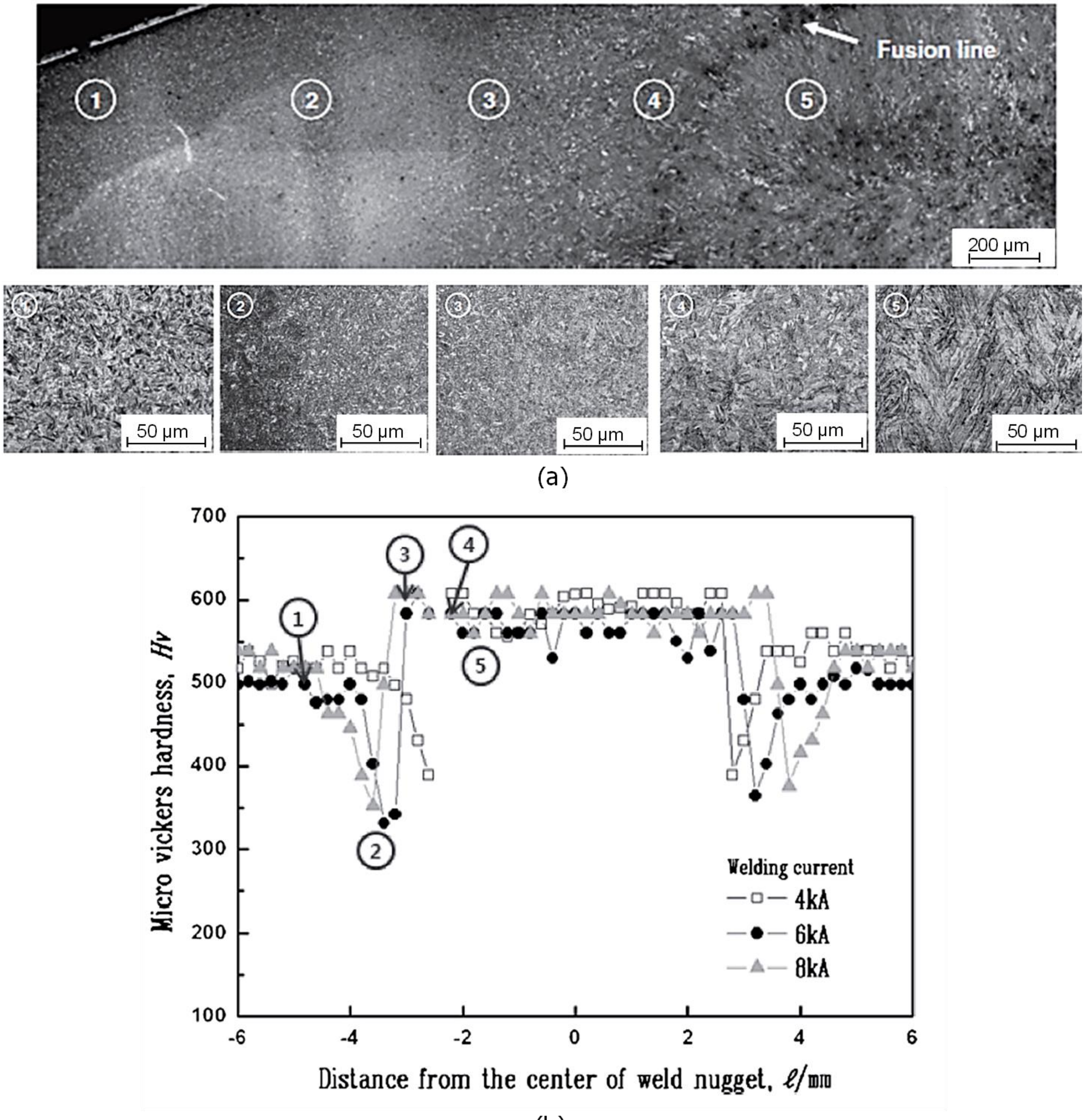

(b)

Figure 2-20 (a) Cross section optical micrograph of spot welded UHSS with welding current 6kA: (1) BM, (2) tempered zone, (3) intercritical and fine grain HAZ, (4) coarse grain HAZ and (5) FZ; (b) corresponding microhardness profile (84)

2.7.1 Microstructure evolution in fusion zone

Two factors govern the microstructural evolution of the FZ in RSW: chemical composition and cooling rate.

Chemical composition – FZ chemistry is dependent on the composition of the BM and their fractions melted during RSW. For similar materials and similar thicknesses, the FZ composition is similar to the BM, but for dissimilar materials the FZ composition depends on the melting ratios of the different sheets which in turn depend on their resistivities and thicknesses (62, 68).

Cooling rate – The cooling rate during RSW is governed by the rate of heat dissipation from FZ by two mechanisms, which are: axial direction through the water-cooled electrodes and radially through the BM. Kim and Eager (85) showed that the ratio of axial heat loss rate to radial heat loss rate is proportional to the ratio of electrode diameter to the square of sheet thickness. Thus the relative dimensions of the weld size, electrode face and sheet thickness are key factors in microstructural evolution in FZ of spot welds. Cooling rate also depends on the alloying elements (68, 86, 87), but because the FZ is subjected to cooling rate much higher than the critical during RSW, microstructure of most AHSS such as martensitic and hot stamping steels are fully martensitic (88, 89).

2.7.2 Hardness evolution in fusion zone

Hardness of FZ is a principal metallurgical factor that governs the mechanical properties of the joint, and it is determined, according to the rule of mixtures, by the fractions of the phases and their individual hardness (90, 91). It also known that the phases are influenced by the welding parameters and chemistry of the materials (92).

Generally, carbon increases the hardenability of steels and also increases the hardness of martensite (62, 93). Therefore carbon content has been used for prediction of hardness of FZ of welds especially for traditional lean chemistry steels containing mainly carbon and lean fractions of other alloys. Yurioka et al. (90, 93, 94) derived empirical relation between carbon content and martensite hardness as:

$$H_m = 884C(1 - 0.03C^2) + 294 \text{ ---2.2}$$

where H_m is the hardness of martensite and C is the carbon wt.%. However, for steels containing higher carbon contents and higher concentrations of alloying elements, such as AHSS, Equation 2.2 becomes less reliable for predicting hardness. Due to the ability of other alloying elements to enhance the effectiveness of carbon on hardenability (62), the carbon equivalent (CE) for transformable steels was developed. One such CE equation was by Yurioka et al. (94), and Khan et al. (93) used this CE to produce an analytical linear relationship for predicting FZ hardness given as:

$$Hv_{FZ} = 630CE_Y + 188 \text{ ---2.3}$$

where Hv_{FZ} is the FZ hardness and CE_Y is the Yurioka carbon equivalent given as:

$$CE_Y = C + A(C).\left\{5B + \frac{Si}{24} + \frac{Mn}{6} + \frac{Cu}{15} + \frac{Ni}{20} + \frac{Cr+Mo+Nb+V}{5}\right\} \text{ -------------------------- 2.4}$$

and $A(C) = 0.75 + 0.25\tanh[20(C - 0.12)]$ is an accommodation factor, which approaches 0.5 for carbon contents less than 0.018% and increases to 1.0 with carbon contents above 0.18% (93, 94). Thus, for the fusion zones of AHSS, hardness after RSW can be predicted.

2.7.3 Transformations in the HAZ

Figure 2-19 and 2-20 have been used to show how temperature profiles and microstructural feature respectively, vary across a spot weld. Figure 2-21. Shows corresponding schematic of hardness profile of the HAZ. From a metallurgical viewpoint the HAZ can be divided into three sub-zones: supercritical, intercritical and subcritical HAZ (62, 68).

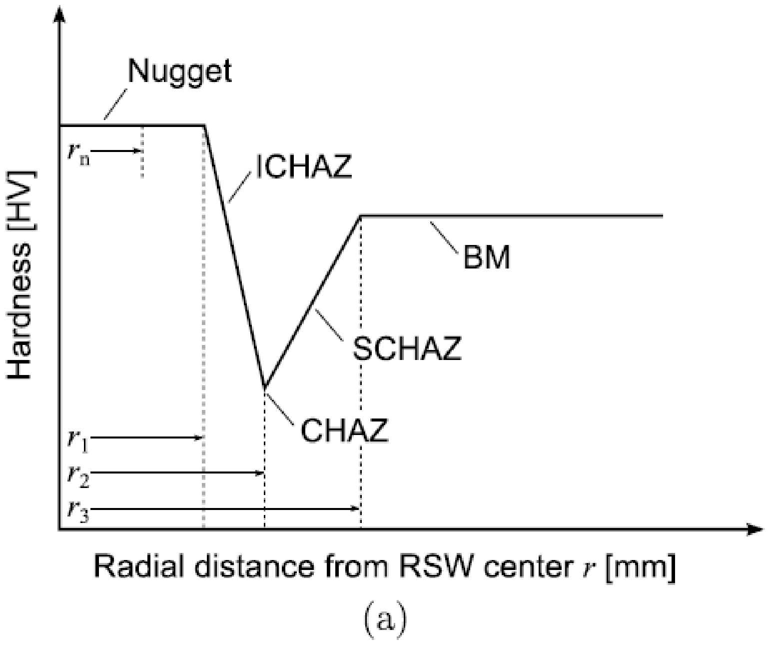

Figure 2-21 Schematic overview and nomenclature of hardness around RSW (83)

Figure 2-21 will be used for discussing the properties of HAZ. The material within $r < r_n$ is the nugget (which has been discussed). Between $r_n < r < r_1$ is the supper critical HAZ, where the material is subjected to temperatures above upper critical temperature (A_{C3}), (see Figure 2-18 or 2-19), therefore, austenite is the stable phase. Since austenite grain growth is very sensitive to temperature and time, microstructure within this zone varies significantly, and can be divided into two parts: coarse grain HAZ (CGHAZ) which is closest to the fusion line (also called grain growth region), and fine (or refined) grain HAZ (FGHAZ). These two regions are demarcated by the grain coarsening temperature. The extent of grain growth in the CGHAZ is determined by the temperature reached above the grain coarsening temperature and the duration. Its large grain size, high cooling rate and rich carbon content promote the transformation to martensite after RSW (68). Thus, it is common to see CGHAZ hardness higher than FZ hardness in some AHSS spot welds. The intercritical HAZ (ICHAZ) region occupies between $r_1 < r < r_2$, and is generated by peak temperatures between lower critical temperature (Ac_1) and upper critical temperature (Ac_3) (68, 83, 84). The material in ICHAZ has been partially austenitized and rapidly cooled, resulting in a final microstructure of a mixture of martensite and tempered variant of the initial BM. In the subcritical HAZ (SCHAZ) region; $r_2 < r < r_3$, the peak temperature has been below Ac_1, resulting in tempered microstructure. Sometimes it is difficult to distinguish this region from the BM, but in some cases, fine precipitates may appear in this region (62, 69, 83, 84, 95). The critical HAZ (CHAZ) is the point of lowest hardness, where the maximum temperature has been closest to Ac_1, and beyond r_3 $(r > r_3)$, the material is not affected metallurgically by the welding process.

2.8 Martensite tempering and HAZ softening

HAZ softening occurs due to tempering of martensite. Martensite is a supersaturated structure, therefore when heated the thermal energy supplied causes it to decomposition into ferrite and cementite as excess carbon diffuse from the supersaturated martensite. The degree of tempering, i.e. HAZ softening and size of the entire HAZ region depends on the peak temperature, duration of exposure and alloying chemistry (and composition) (31, 33, 34). For example, from the hardness profiles shown in Figure 2-20, it can be deduced that the HAZ size increased as the welding current increased, as can be seen that the HAZ width increased in the order: 4kA< 6kA < 8kA, knowing that the highest heat input (and highest temperature) occurred during welding with 8kA current.

2.8.1 Effects of alloying elements on HAZ softening

Alloying elements have considerable influence on the kinetics and mechanism of the transformation, i.e. tempering of martensite. Generally, the presence of any element retards the rate of softening during tempering but different elements are potent to different degrees in this regard (33, 96). For example, Si, Mn and Ni retard the rate of softening of martensite during tempering, where Si has the most significant effect, while Ni is least significant, for equal percentage content of these elements (33). Carbide forming alloying elements such as Cr, Ti, V, Ni, W and Mo, also retard the rate of softening during tempering, but by a different mechanism, in that they stabilize both the transition carbides (e.g. -iron carbide) and the supersaturated martensitic structure to a higher tempering temperature and by considerably delaying the precipitation and growth of cementite (FeC). (31). Thus, Coarsening of cementite in the tempering temperature range 400-700°C, which leads to significant loss of hardness, can be hindered effectively when alloying elements such as Si, Cr, Mo and W are present in steels in sufficient quantities.

2.8.2 Effects of coating on HAZ softening

It was discussed earlier that the choice of alloying elements for the steel substrate is necessarily moderated by the choice of coating. Therefore, the effects of the coating can be linked to the alloying elements necessary for the application of the coating. Also, the electrical resistance and thermal properties of the coating which control the thermal history of the HAZ may have some influence on HAZ softening, but this has not been studied.

2.9 Dynamic resistance

During RSW, changes in metallurgical and thermal properties of the sheet stack result in change in electrical property (resistance) of the stack-up. Record of this changing resistance produces a dynamic resistance profile (DRP), which is material sensitive, and may be used for process study.

In order to utilize DRP as a study tool, the general fundamental characteristics need to be understood, since such profiles are characteristic of material and welding parameters. For example, Figure 2-22 shows the DRP measured between the electrodes of three different materials: mild steel, stainless steel and aluminium; their distinct characteristics are obvious.

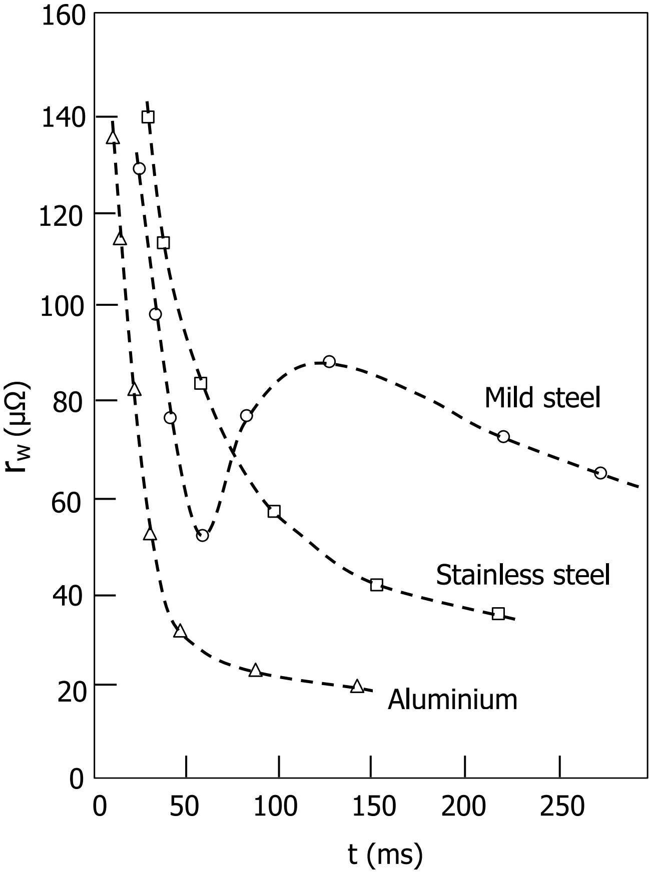

Figure 2-22 Typical dynamic resistance curve of mild steel, stainless steel and commercially pure aluminum (97)

Dickinson et al. (98) characterized the DRP for plain carbon steel, by dividing the profile into six stages, based on the shape and distinct phenomenon observed during each stage. In order to proffer an explanation for the observed profile, a theoretical representative curve and events associated with each stage of the curve were generated as shown in Figure 2-23. Using this figure, stage I represents a sharp drop in resistance due to breakdown of surface film insulation, stage II represents surface heating when asperities are softened and contact area increased, causing resistance to decrease further until a minimum point, alpha (α), is reached. During stage III heat is now concentrated on the bulk material, causing the resistivity, and hence resistance, to increase. As the temperature increases, stage IV is reached when melting of the specimen begins.

As melting progresses, contact area decreases as the molten metal spreads, mechanical collapse and shortening of current path also occur, causing the resistance curve to go through a maximum point (β) and to continue to decrease. In stage V the volume of molten metal steadily increases and mechanical collapse continues, resulting in steady decrease in resistance. Stage VI could be reached if the volume of molten metal increases beyond what can be contained under the applied electrode force and constraining solid metal, causing expulsion to occur, which will be registered as a sharp drop in resistance.

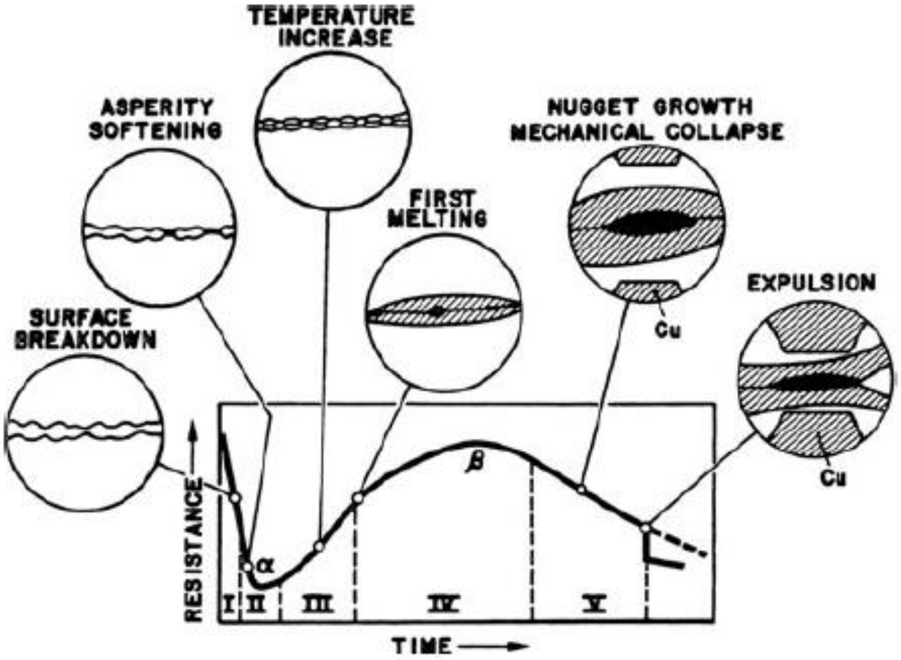

Figure 2-23 Theoretical dynamic resistance curve (98)

Following similar procedure but using slightly different boundaries, Gedeon et al. (99) proposed four and six stages for uncoated and galvannealed (GA) steels respectively. Other works on dynamic resistance study of Zn based coated steels have also been reported by Gedeon and Eager (100) and Ma et al. (101). These works indicate that the ability to characterize the resistance profile for a material can lead to better understanding of the RSW of the material.

Thus, there have been reports of using DRP for studying RSW process for various materials (102-104),weld quality control (97, 105) and estimating nugget size (106).

AlSi and GA coatings have different electrical resistances, therefore they behave characteristically under pressure and heat (RSW conditions). Since the resistance profile during RSW depend on the type of coating and the steel, DRP study of the different coated steels could be useful for characterizing and monitoring the joining stage during RSW.

3 Experimental Details

3.1 Materials

AlSi coated and GA hot-stamping steels, Usibor, 1.2 mm thick were used in this work. Alloying compositions and calculated carbon equivalents (CE_Y) of the substrates are shown in Table 3-1. (CE_Y was calculated using Equation 2.4). The materials were investigated in both as-received (AR) and hot-stamped (HS) conditions. Hot-stamping was done at (900°C) for 6 minutes (14). All the HS GA sheets were sandblasted after hot-stamping to thoroughly clean the surfaces, as practised in industry (26).

Table 3-1 Alloying compositions of AlSi and GA coated Usibor in wt %

Element	**Wt.%**	
	Al-Si	GA
C	0.225	0.221
Mn	1.16	1.17
P	0.013	0.012
S	0.002	0.003
Si	0.190	0.252
Cu	0.009	0.038
Ni	0.005	0.017
Cr	0.206	0.179
Sn	0.001	0.003
Al_{sol}	0.039	0.037
Al_{total}	0.042	0.038
Ca	0.0019	0.0013
Nb	0.001	0.002
Mo	0.002	0.005
V	0.004	0.006
Zr	0.002	0.002
Ti	0.034	0.026
B	0.0030	0.0025
N	0.0056	0.0064
CE_Y	0.48	0.48

3.2 Welding process

RSW was performed using a Centerline Ltd. manufactured Mid Frequency Direct Current (MFDC), 144/180-kVA welder shown in Figure 3-1. Welding electrodes were RWMA Group A, Class II, domed-flat nose, face and body diameters are 6mm and 16mm respectively. AR and HS specimens were welded after cleaning with acetone. Single pulse was applied at a weld force of 4.4 kN, hold time of 150 ms and cooling water flow rate of 4 litres/min. The weld time was varied to observe different stages during the welding process.

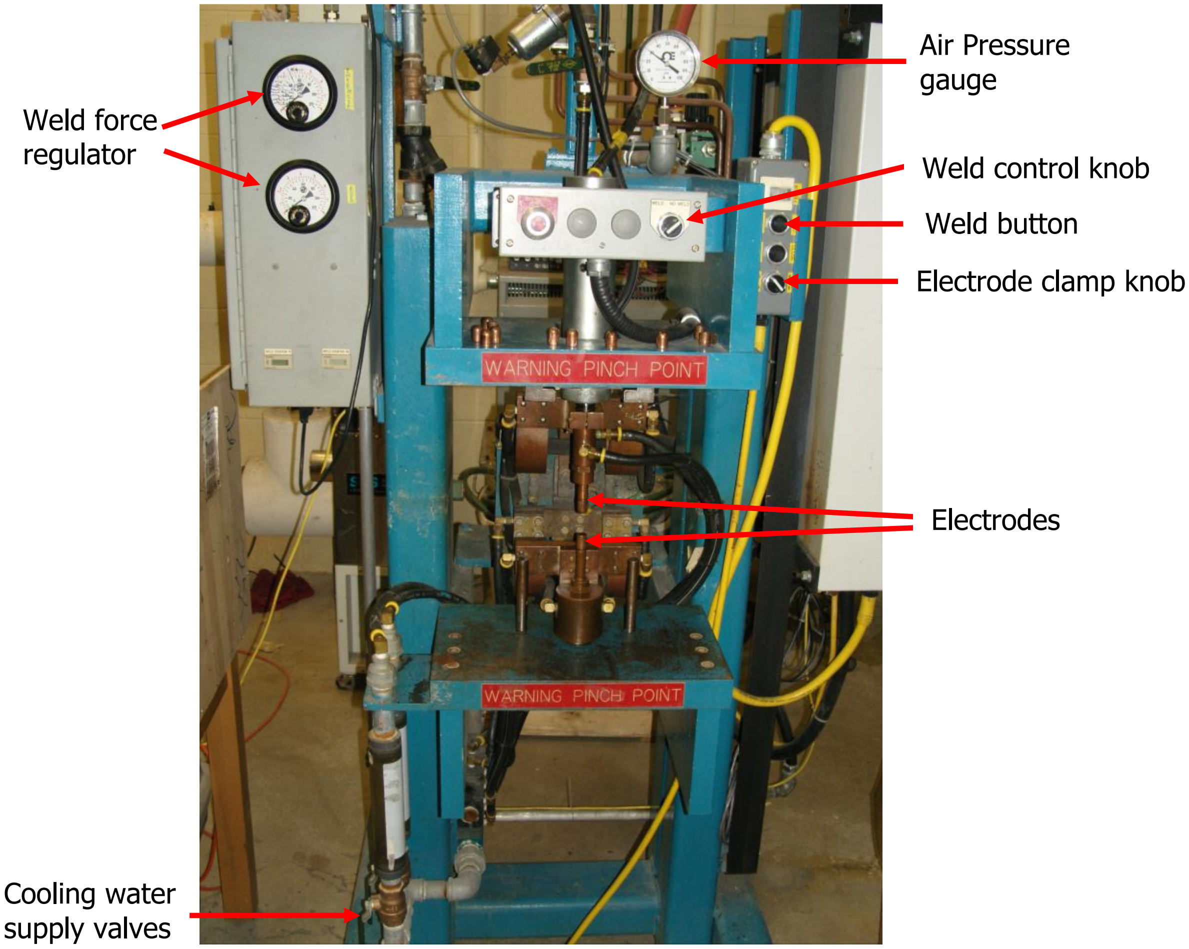

Figure 3-1 MFDC RSW machine

3.3 Electrical resistivity and resistance measurements

The GA coating was first removed by soaking 25 mm by 300 mm strips in a solution of HCl (ratio HCl:H_2O was 1:3) for about 10 hours, when the reaction was observed to have ended. AlSi coating was removed by soaking in a solution of NaOH obtained by dissolving 10g of NaOH in a litre of water. Electrical resistivity data were afterwards obtained according to the ASTM standard B193-02. Four measurements were made for each of the specimens: AlSi and GA coated sheets in AR and HS conditions, using Agilent 34420A Nanovolt/micro ohm meter. Static electrical resistance data were also obtained for all specimens using four-point measurement method according to ISO 18594:2007 (E) standard. The set-up for the measurements is shown in Figure 3-2, having a TEKPOWER 3465A and Agilent 34411A multimeter used for DC power supply and voltage measurements respectively, and the connections to the electrodes of the MFDC resistance spot welding machine. Clamping force was 4.4 kN. Dynamic resistance profiles data were acquired through the GeniusHWI 516W welder controller. During resistance profile acquisition, various values of currents were run for various times to establish specific data points. Specimens corresponding to each data point were observed visually and microscopically for characterising the dynamic resistance profile.

Figure 3-2 Equipment set up for 4-point static resistance measurement

In order to determine the values of components of the resistance, dynamic resistance profiles for single sheet set-ups (without a faying interface) were also used. Figure 3-3 shows the schematics of the set-ups for double and single sheet.

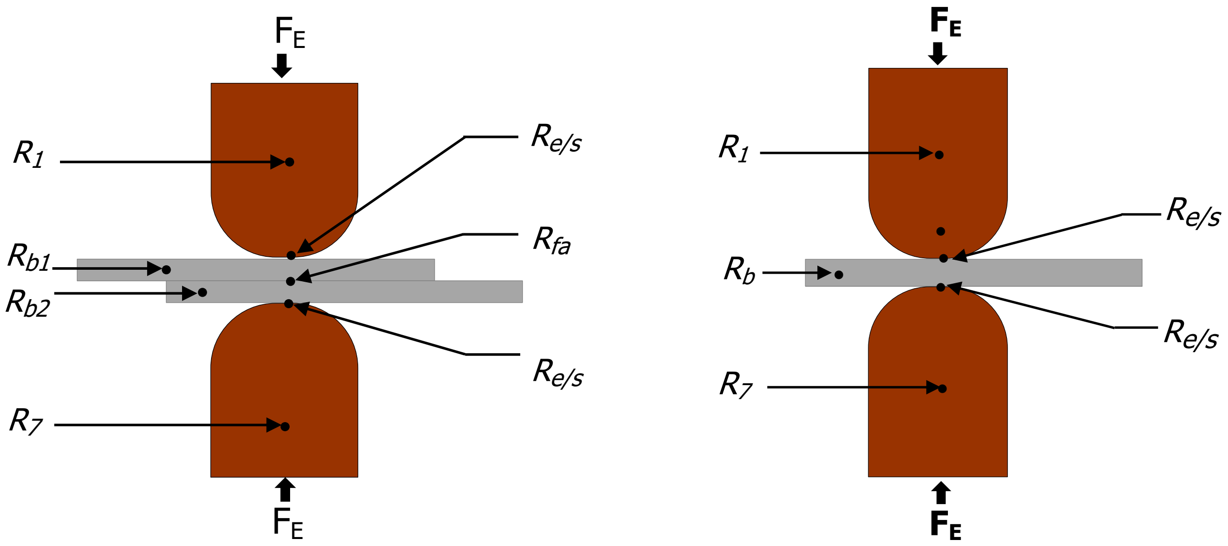

Double sheet stack with an interface

Single sheet without interface

Figure 3-3 Schematics showing double and single sheet set-ups

3.4 Metallography and microstructure

Metallographic sections were prepared to obtain specimens for determining coating thickness, weld size, hardness and microstructural examinations. Nital reagent (5 % nitric acid in 95 % ethanol) was used for etching. Weld sizes were measured using stereoscope. Scanning electron microscope (JEOL JSM 6460) was used for measuring coating thickness and for microstructural examinations. EDX (Oxford Instrument Microanalyses System) fitted to the electron microscope was used to identify elemental compositions in the coatings.

.

3.5 Hardness measurements

Hardness profiles were obtained using Vickers micro-hardness tester following AWS/SAE/D8.9-2012 standard (81), using 500 g load for 15 seconds dwell time. The profiles were obtained diagonally across the sheets through the fusion zones for all specimens, and indentations were spaced 0.2 mm apart except near the heat affected zones (HAZ) where indentations were more closely spaced at 0.1 mm apart to capture the hardness profile more accurately. Hardness mapping was done for the base metals in the as-received and hot-stamped conditions. Hardness mapping was also done around the welded area of the AlSi/GA (HS) joints to measure differences in hardness of the AlSi and GA sides of the specimen more accurately.

3.6 Mechanical tests

Tensile tests coupons were made by shearing 100 mm × 30 mm strips from as received and hot stamped sheets. For each test, two sheets were welded with a 30 mm overlap, containing a single centrally located spot weld. Similar sheet combinations of AlSi/AlSi, GA/GA as well as dissimilar combinations of AlSi/GA were welded and used for the tensile-shear tests. Tests were performed on an Instron universal testing machine at a cross-head speed of 1 mm/min. After mechanical testing, fusion zone diameters were measured either on faying interfaces or pull-out buttons of failed coupons.

4 Results and Discussions

4.1 Coating microstructure

Figures 4-1a and b show AlSi and GA coatings respectively. Nearest the substrate/coating interface of Figure 4-1a, EDX on the area marked "A" shows elemental composition of 60.4, 22.5 and 17.1 wt. % for Fe, Al and Si respectively. These are usually a mixture of intermetallic phases (IMCs) rich in Fe due to the closeness to the steel substrate, and the composition depends on the Si content and coating procedure (107, 108). Other IMC formations which are usually less rich in Fe are also seen as islands away from the interface. For the portion marked "B" EDX shows compositions of 89.4 and 10.6 wt. % for Al and Si respectively. This indicates pure coating composition without IMC formation close to the surface of the coating. On Figure 4-1b, EDX on the section "1", at the substrate/coating interface, revealed 81 and 19 wt. % elemental compositions of Zn and Fe respectively. For the area marked "2", elemental compositions were 89.9 and 10.1 wt. % for Zn and Fe respectively. These values indicate that regions "1" and "2" are composed of gamma and delta phases which have compositions ranging between 17-19.5 wt. % Fe, and 7.0-11.5 wt. % Fe respectively (18, 41).

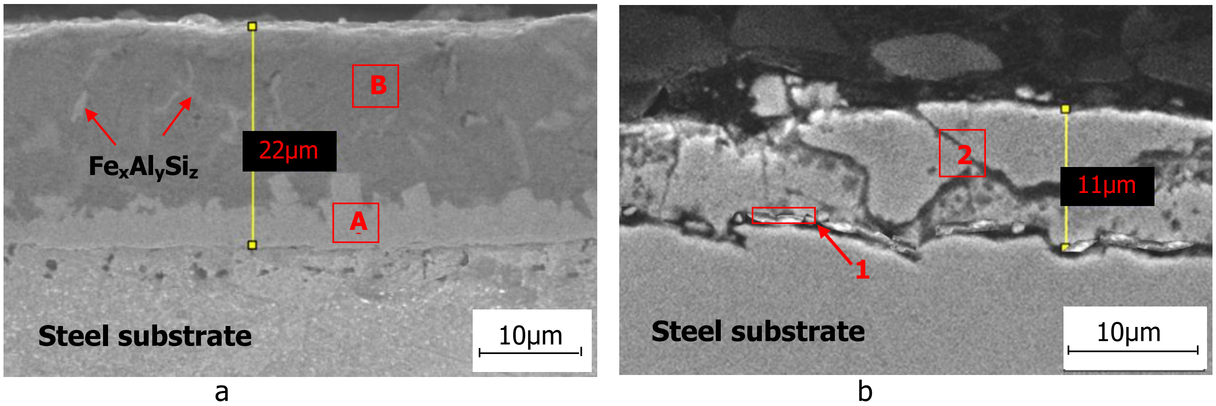

Figure 4-1 Coating microstructure in as-received conditions for: (a) AlSi and (b) GA

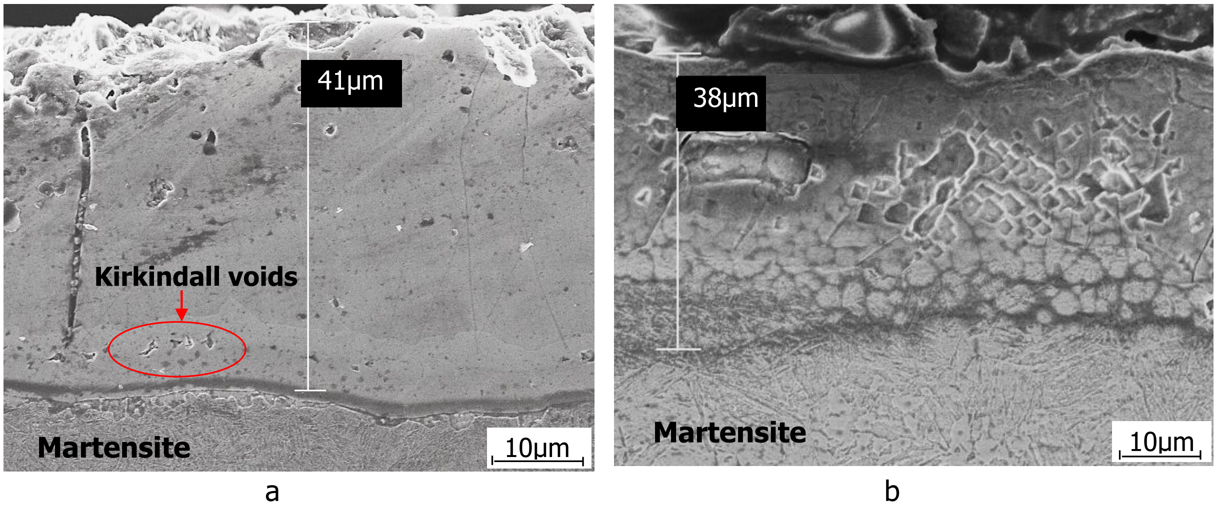

Figure 4-2 Coating microstructure after hot-stamping: (a) AlSi and (b) GA

After hot-stamping at 900° C for 6 minutes, coating microstructure changed and coating thickness increased. For the AlSi coating (Figure 4-2a), cracks approximately normal to the steel/coating interface are generated due to brittleness and thermal expansion mismatch of the new phases (109). Kirkindall voids generated as a result of surplus vacancies arising from differences in diffusion coefficients of Fe and Al are also seen. (108, 110). Another source of voids in the microstructure is due to differences in densities between the emergent phases; as phases of low density transform into high density phases (109). These microstructural features have significant implications on the electrical resistance and weldability of the material.

A few microstructural changes were observed in the GA coating after hot-stamping. The coating thickness increased (compare Figures 4-1b and 4-2b), but no new phases were seen, as at the hot-stamping temperature, all the phases of the coating melted, according to the Fe-Zn phase diagram shown in Figure 4-3, and when quenched, the phases are reformed, however, their distribution and proportions were altered (relative to the as-received condition).

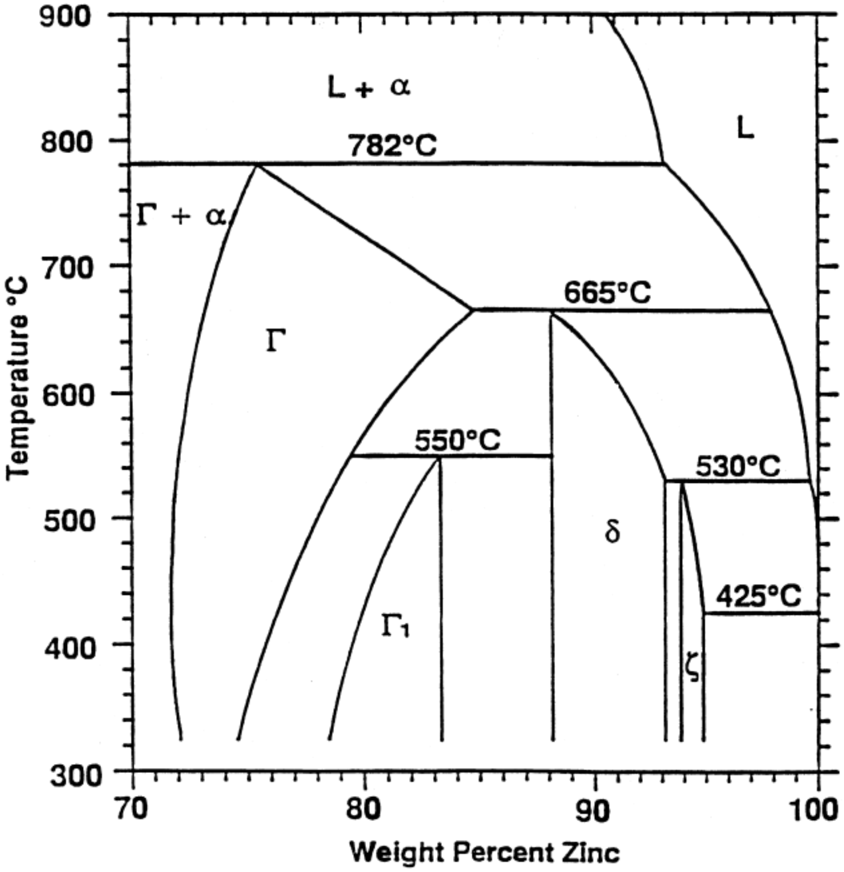

Figure 4-3 Zn-rich end of the Fe-Zn phase diagram (41)

4.2 Substrates microstructure and hardness

The microstructures of both AlSi and GA coated specimens consist of similar phases in both AR and HS conditions. The AR microstructure is comprised of ferrite with islands of pearlite (107, 111), as shown in Figure 4-4a. After hot-stamping, the microstructure transformed to martensite, as shown in Figure 4-4b. AR hardness for AlSi coated specimen is 164 ± 6.97 HV, which is slightly less than 184 ± 8.52 HV for GA coated specimen. After hot-stamping, hardness increased to 496 ± 11 HV and 494 ± 18 HV for AlSi (HS) and GA (HS) specimens respectively.

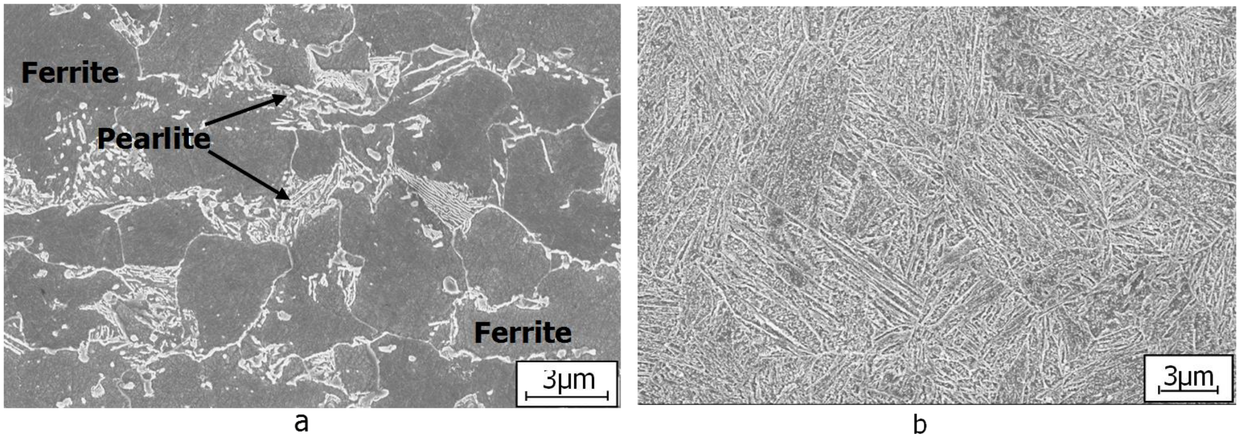

Figure 4-4 (a) As-received microstructure showing pearlite and ferrite phases and (b) fully martensite phase after hot-stamping

4.3 Resistivity and static resistance

The resistivity of the substrate in as-received condition for both AlSi and GA coated specimens are similar (without significant difference), having a value of (23.02 ± 0.36) × 10^{-8} Ωm, while the resistivity for the hot-stamped condition for both specimens is (23.78 ± 0.45) × 10^{-8} Ωm at 95% confidence interval.

Static electrical resistance values for AlSi, GA and the combination AlSi/GA are shown in Figure 4-5. The differences exhibited by these specimens must have been influenced by the different coatings, since the resistivities of the substrates are identical. The apparent higher resistance of the AlSi (AR) is considered to be due to the presence of thin film of Al_2O_3 on the surface of the coating (107). To clarify the apparent higher AlSi electrical resistance, dynamic resistance profiles were utilized. During the initial stage of RSW, an ‘alpha-point’ is reached when the surface film/oxide layer is completely broken and the resistance drops significantly to permit the full welding current to flow (98, 102, 104). Beyond the alpha-point, influence of oxide layer does not exist, so that the true electrical resistance of sheet stacks can be compared. Figure 4-6a shows early stages (first 25 ms) of dynamic resistance profiles for AlSi (AR) and GA (AR) for various welding currents. It is seen that the GA (AR) specimen actually has higher electrical resistance than the AlSi (AR).

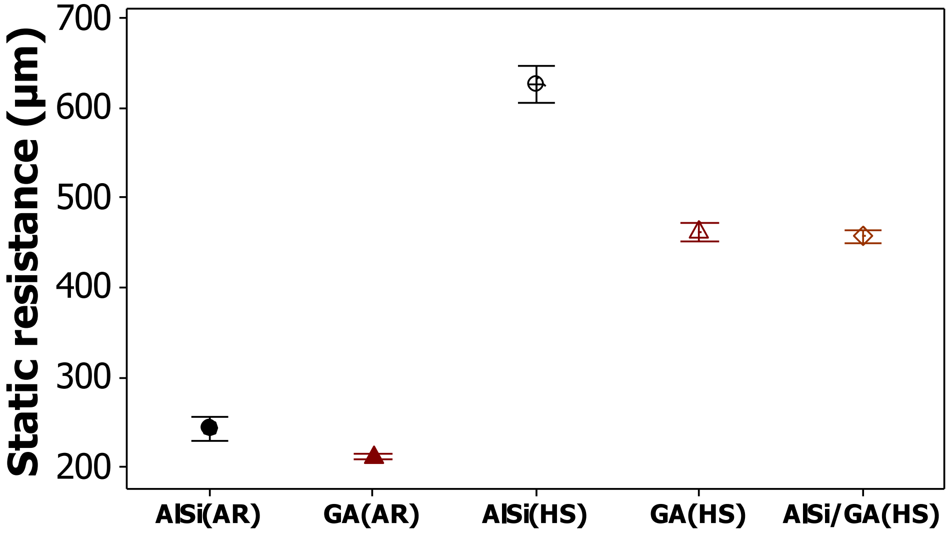

Figure 4-5 Static electrical resistances of the specimens

In hot-stamped condition, build-up of surface films and oxides as well as increase in coating thickness contributed to increased electrical resistance; this is supported by Figures 4-5 and 4-6. The AlSi (HS) exhibits significantly higher resistance than the GA (HS) specimen because after hot-stamping, the AlSi coating is transformed to high resistivity phases: Fe_2Al_5 and FeAl (112-114). Also, these phases are much harder than the phases present in as-received condition (107, 112, 115), and electrical contact resistance increases with surface hardness (116). Thus, all hot stamped specimens possess higher electrical resistance than as-received specimens. These resistance values significantly influence current and nugget formation during RSW.

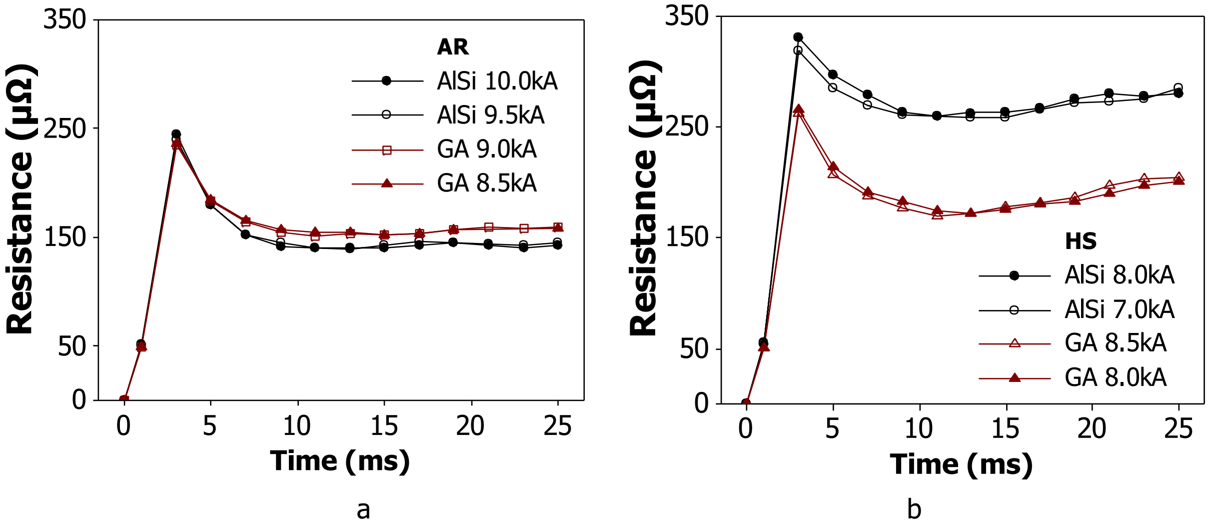

Figure 4-6 Early stages of dynamic resistance for specimens welded using shown currents: (a) as-received and (b) hot-stamped

4.4 Dynamic resistance stages for AlSi coated steel in hot-stamped condition

Stages encountered for electrode-to-electrode profile dynamic resistance for hot-stamped AlSi coated steels are first presented in this section. Current used was 7.5 kA.

Stage 0 (Surface heating) – There is an initial rise in resistance during RSW due to heating effect as current begins to flow, causing voltage build-up, to attain the surface oxide film breakdown voltage (97, 98, 100). Figure 4-7 shows this stage on the dynamic resistance profile for hot-stamped AlSi, in this case using a current of 7.5 kA. This stage is not mentioned in the models by Dickinson et al. (98) and Gedeon and Eager (100). However, it is very important to identify this stage because firstly, it establishes the existence of an initial heating stage before the first peak, and secondly, it helps explain the reason the initial peak dynamic resistance values are different from measured static resistance values.

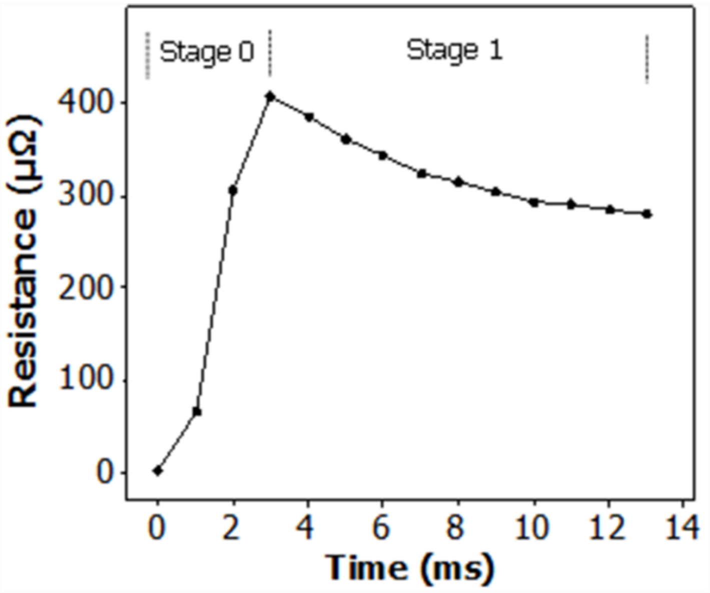

Figure 4-7 Dynamic resistance profile for stages 0 and 1 for AlSi (HS) using 7.5kA

Stage 1 (Surface film breakdown) – This stage is characterised by a sharp drop in resistance due partly to fritting, a complex process of oxide film insulation breakdown (97, 100, 104), and partly to some asperity collapse. During this stage, heating is concentrated at the surface oxide film layer since no appreciable current flows through, therefore the sheet stack remains at room temperature (94, 96). Figure 4-8 shows the microstructure at the end of stage 1 (13ms).

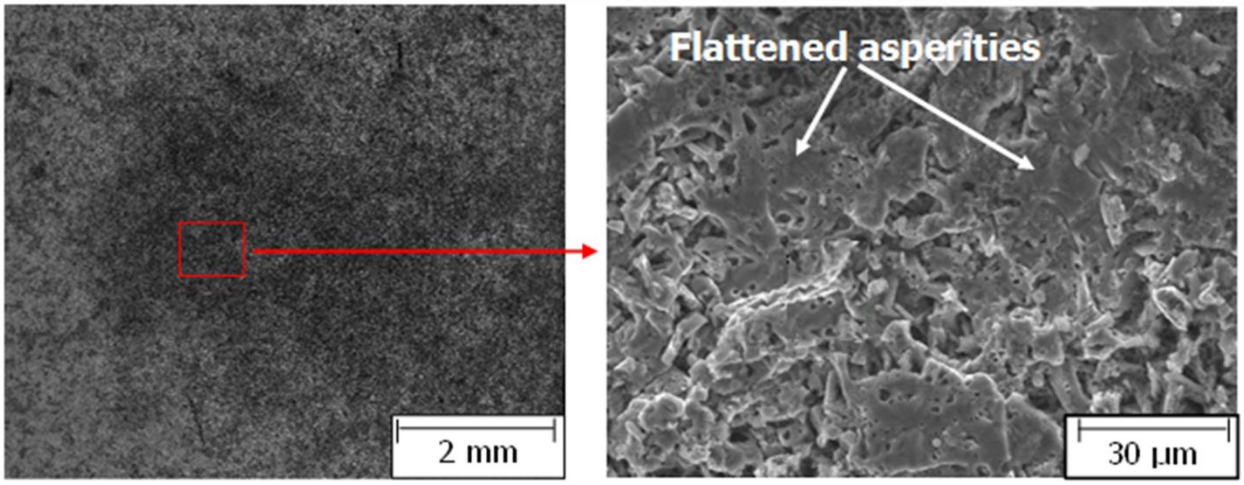

Figure 4-8 Faying interface of AlSi (HS), welded at 7.5 kA for 13ms, showing some flattened asperities. Microstructure corresponds with end of stage 1in Figure 4-7

Stage 2 (Heating and softening of the coating) – During this stage heating is concentrated on the coating at the faying and electrode/sheet (e/s) interface. Some bulk heating also takes place, resulting in a rise in the dynamic resistance profile. The major microstructural feature of this stage is pronounced collapsing of asperities due to softening of the coating as the temperature rises. The curve and image shown in Figure 4-9 represent the resistance profile and microstructure at the faying interface up to the end of stage 2, i.e. 20 ms. Flattening of asperities causes reduction in resistance, but heating of the coating and bulk material cause resistance to rise, resulting in a net rise in dynamic resistance profile.

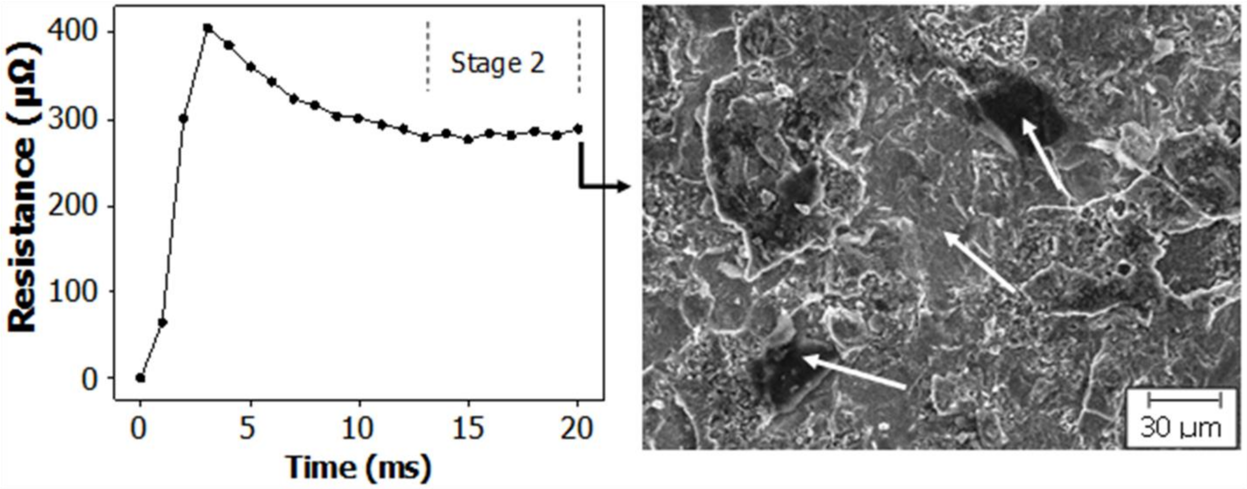

Figure 4-9 Stage 2, rising portion of the resistance profile due to heating of AlSi (HS) coating, and microstructure at the faying interface at end of stage 2 (i.e. 20 ms), showing pronounced asperities flattening (arrows) due to softening of the coating

Stage 3 (Coating melts) – As heating and softening continues beyond stage 2, the coating begins to melt (especially at the faying interfaces). The microstructure at the beginning of this stage (which is also the interface between stages 2 and 3) is shown in Figure 4-10b. As coating melts, it spreads, increasing the contact area, causing decline in resistance. Also, electrode pressure squeezes the molten coating away from under the electrodes as the bulk sheets move closer, reducing the current flow path; this also causes reduction in resistance. Eventually, net resistance peaks and begins to decline shortly after coating begins to melt. Figure 4-10a shows the dynamic resistance profile for AlSi (HS) up to end of stage 3 (31 ms). Figure 4-10c shows the microstructure at a faying interface corresponding to 31ms of weld time at 7.5 kA, revealing that the molten coating has been displaced (from under the electrode).

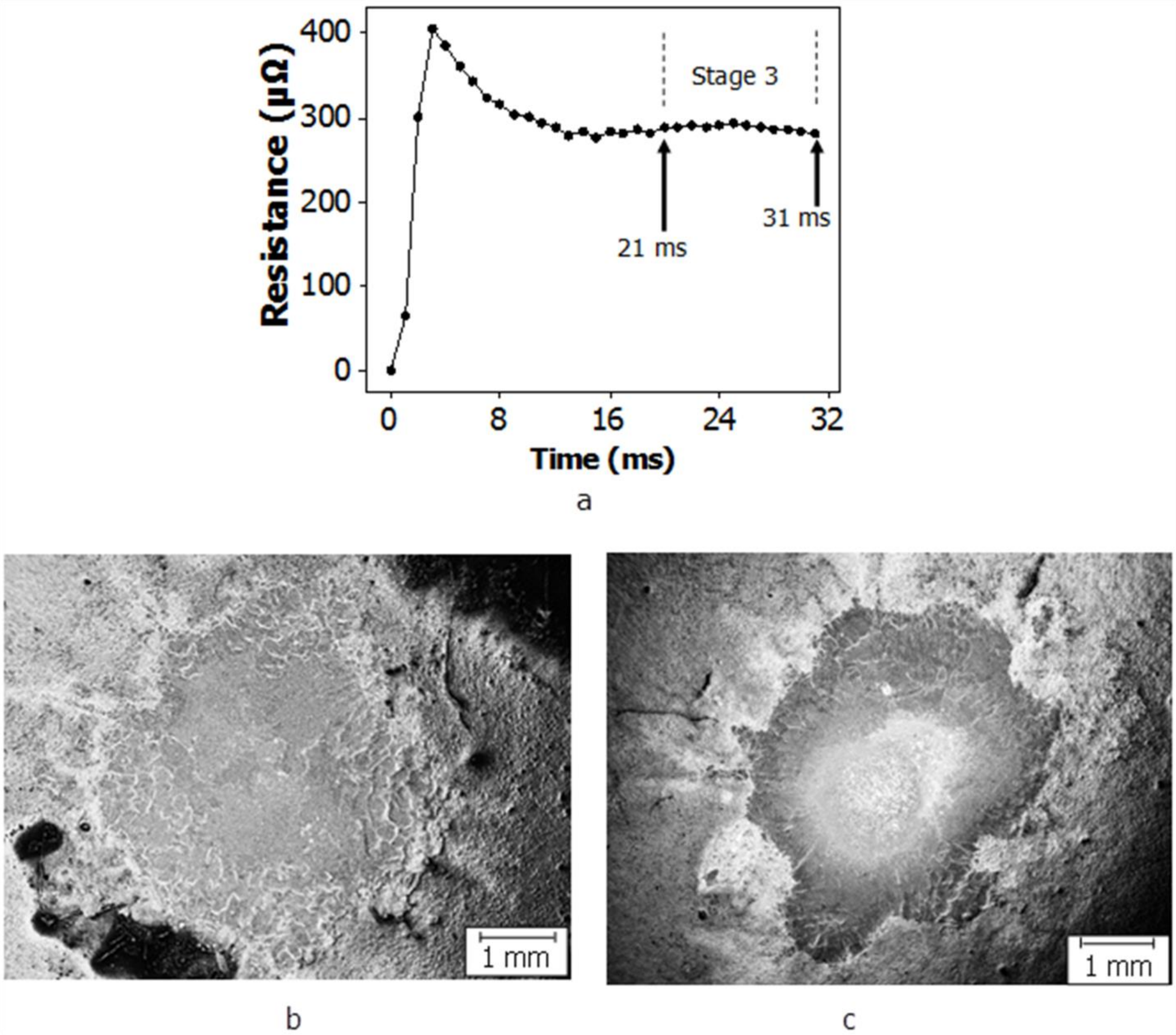

Figure 4-10 Stage 3: (a) Dynamic resistance profile for AlSi (HS) using 7.5kA weld current, showing the peak and subsequent decline as the coating melts and spreads, (b) Microstructure of faying interface at beginning of stage 3 (21 ms), showing molten coating, (c) Microstructure corresponding to the end of stage 3 (31 ms), showing displaced coating.

Stage 4 (Bulk heating/melting) – After coating is displaced from the faying interface heating is now concentrated on the bulk steel substrate. The resulting sheet/sheet (s/s) interface resistance and increase in bulk resistance due to increase in resistivity with temperature cause an increase in total resistance. However, as more coating is displaced from under the electrodes and electrodes dip into the coating at the e/s interfaces as coating softens with increasing temperature, current path reduces and contact area increases, causing resistance to reduce. Increasing temperature with time also causes more asperity flattening at the e/s interface, contributing to lowering the total resistance. Figure 4-11b shows an image at a faying interface with BM exposed after 46 ms. As heating of bulk sheets continue, another phase change (melting) begins; the commencement of nugget formation, as shown in Figure 4-11c. Nugget formation causes (gradual) elimination of the faying interface resistance, contributing also to a reduction in resistance. However, melting causes increase in resistance of steel due to increase in resistivity with melting (117). Significant increase in resistance associated with heating and melting of steel during stage 4 should appear as a hump on the dynamic resistance (100, 104, 118) but due to the opposing directions of resistance components, the hump may not be obvious in the dynamic resistance profile; this is the situation in Figure 4-11a.

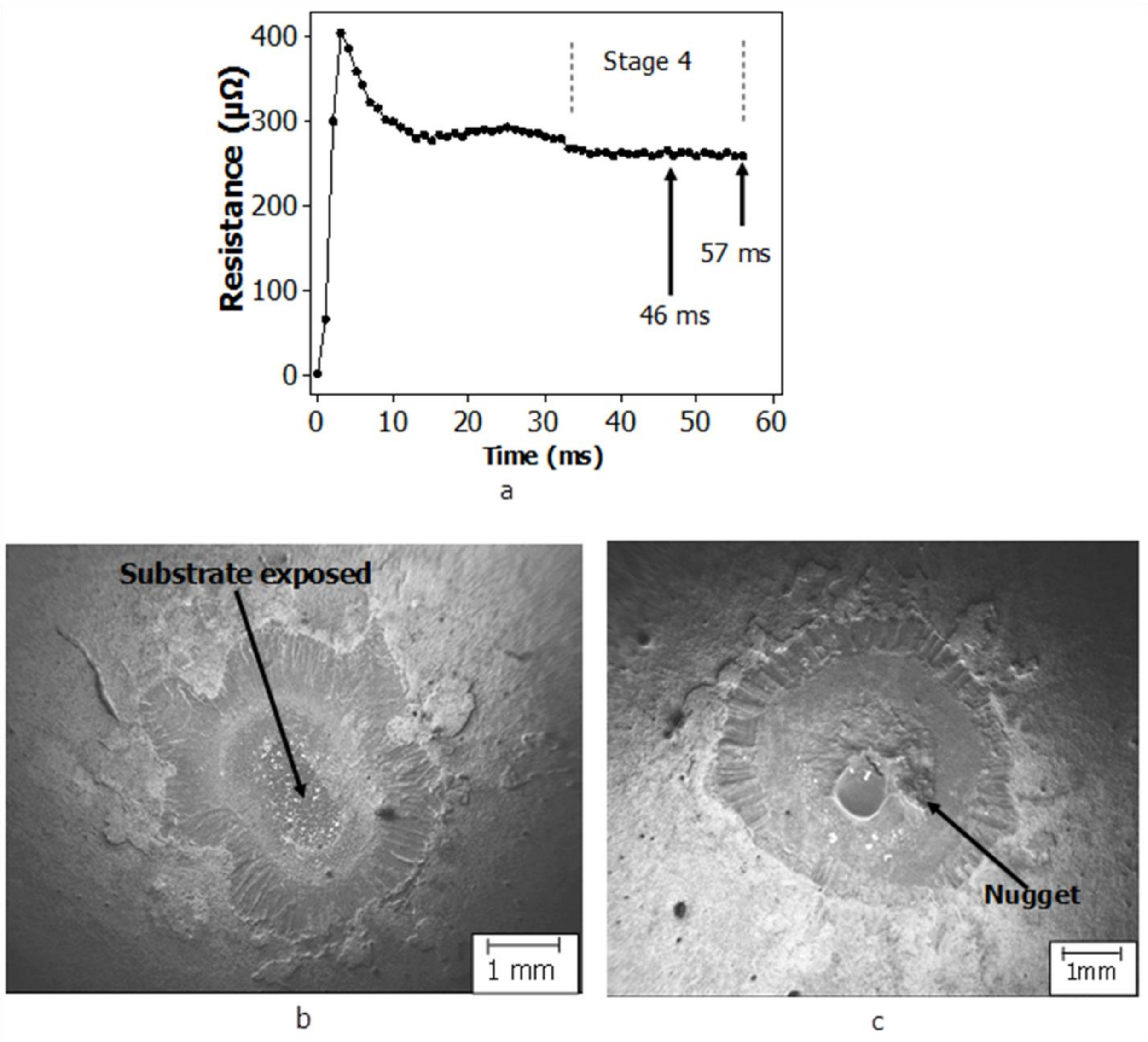

Figure 4-11 Stage 4: (a) Dynamic resistance profile for AlSi (HS) welded at 7.5kA when heat is concentrated on the BM, (b) Microstructure of faying interface corresponding to 47 ms of welding shows a portion of the BM after the coating has been displaced, (c) microstructure of faying interface corresponding to 57 ms showing nugget formation.

Stage 5 (Nugget growth) – Shortly after commencement of melting, and nugget progresses in size, significant volume of molten metal now exists. This reduces rigidity of the stack and causes electrode close-up movement, leading to indentation and reduction of current flow path. Also the contact area increases as the nugget grows. These effects cause the resistance profile to peak and begin a downward trend as shown in Figure 4-12.

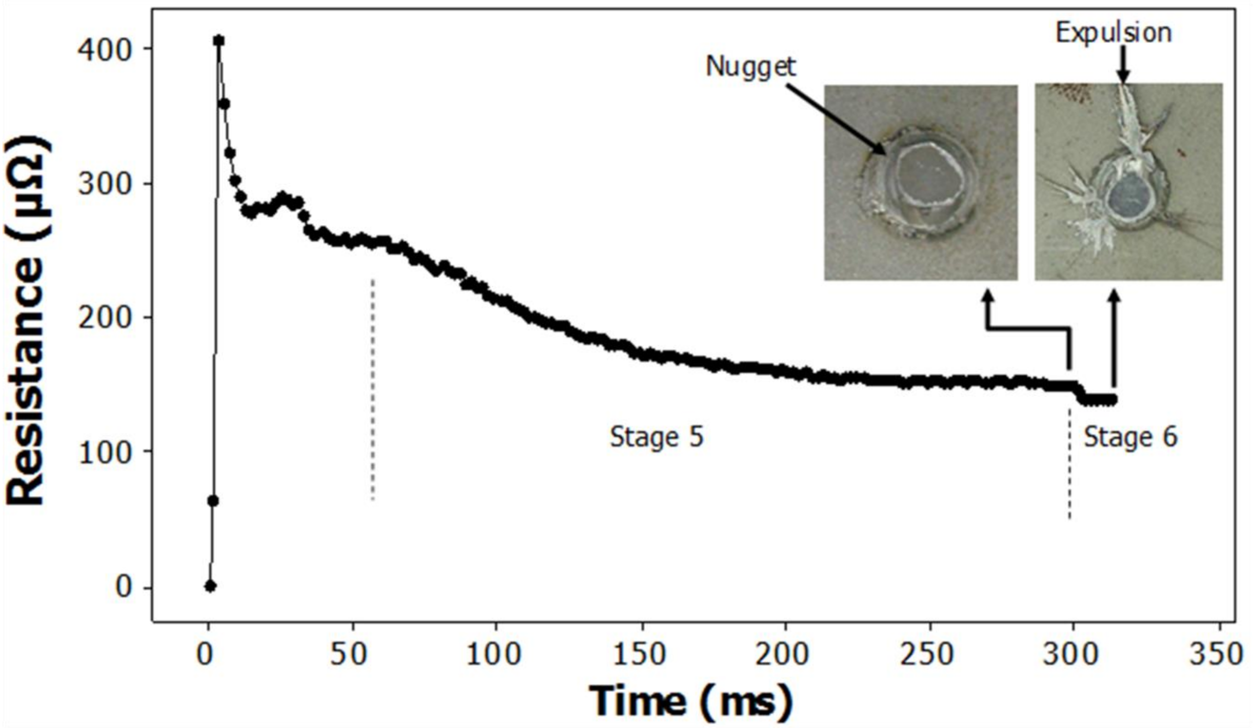

Figure 4-12 Resistance profile for AlSi (HS) welded at 7.5kA, showing up to stages 5 and 6.

Stage 6 (Expulsion) – This stage may not be reached; it is included for completeness. Expulsion stage may be reached if heating continues and nugget growth continues to a size when the molten metal pressure can no longer be contained under the electrode pressure. This situation can be caused by excessive current or time, and it leads to expulsion of molten metal, which is characterized by sudden drop in resistance during the nugget growth stage. It also shows up as severe indentation on the welded joint. Expulsion also occurs if the current is excessive; in this case the nugget will not necessarily grow to optimal size before expulsion occurs. This could occur as a result of very high heating rate that creates localized high pressure which causes expulsion. Expulsion causes loss of material and consequent loss of strength of the joint. Figure 4-12 also includes stage 6, showing a nugget exhibiting expulsion due to excessive weld time. Similar experiments were also conducted for AlSi in the as-received condition as well as for GA coated specimens in both as-received and hot stamped conditions. Figure 4-13 shows profiles for specimens in as-received and hot stamped conditions for AlSi and GA specimens. It shows that both coating types produce similar dynamic resistance profiles, regarding the number of stages, but the features/stages in the profiles are sharper and more detectable for materials in the hot-stamped conditions due to the higher resistance and higher coating thickness for the hot stamped materials. Summary of a generalized model for dynamic resistance profile for coated steel using mid-frequency-direct-current (MFDC) power supply is shown in Figure 4-14.

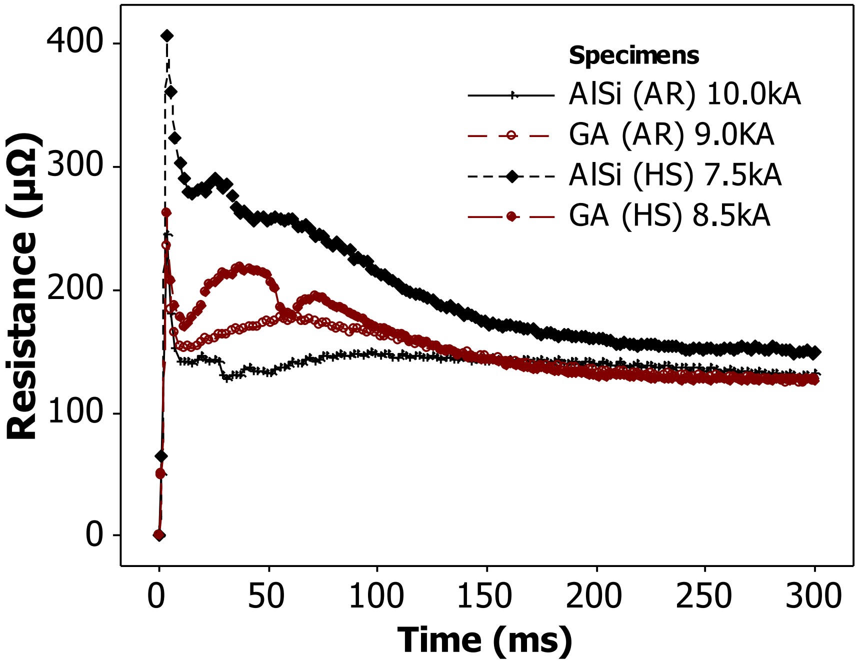

Figure 4-13 Dynamic resistance profiles for all specimen types, and their welding currents

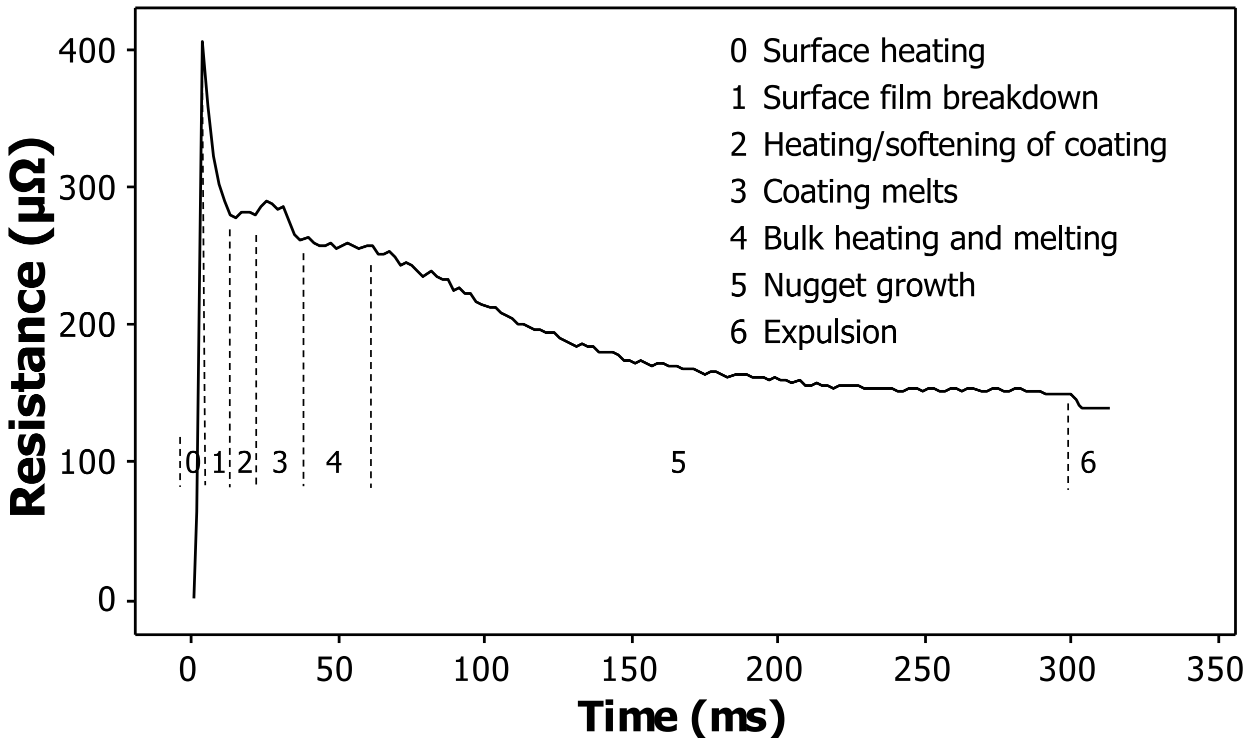

Figure 4-14 Generalized dynamic resistance profile for coated steels using MFDC supply

4.5 Determination of resistance components

To determine the values of resistance components, RSW for single sheet set-up (as shown in Figure 3-1) was also carried out. Figure 4-15 shows the dynamic resistance profiles for three single sheets (S1, S2 and S3), and three double sheets (D1, D2 and D3) for AlSi and GA specimens. It was observed that the end of stage 1 was coincident in their profiles for both the double sheets and single sheet set-ups. This makes it possible to carry out the evaluation at the coincident point, when the surface film has no influence and the set-up is at room temperature. Equations 4.1 through 4.4 were employed for computing the components of resistance:

$$R_b = \rho \frac{l}{A} \quad \text{---} \quad 4.1$$

$$2R_{e/s} + R_b = R_{T1} \quad \text{---} \quad 4.2$$

$2R_{e/s} + 2R_b + R_{fa} = R_{T2}$ -- 4.3

$R_{fa} + R_b = R_{T2} - R_{T1}$ --- 4.4

R_b is the bulk (BM) resistance, ρ is the resistivity of BM, A is the surface area under the electrode, $R_{e/s}$ is the electrode/ sheet interface resistance, $R_{T1}$is the total resistance for a single sheet set-up, R_{T2} is the total resistance for double sheet set-up and R_{fa} is the faying interface resistance. The mean differences between the resistances of the single and double sheets at the end of stage 1 are shown on each specimen set in Figure 4-15; these represent the mean values of $R_{T2} - R_{T1}$ of Equation 4.4. The current path through double sheets is 2.4mm (each sheet is 1.2 mm thick, coating thickness is negligible). Equations 4.1 through 4.4 enable the computation of the resistance component values. Figure 4-15 shows the graphs of the computed values of the faying interface and electrode/sheet interface resistances at the beginning of welding.

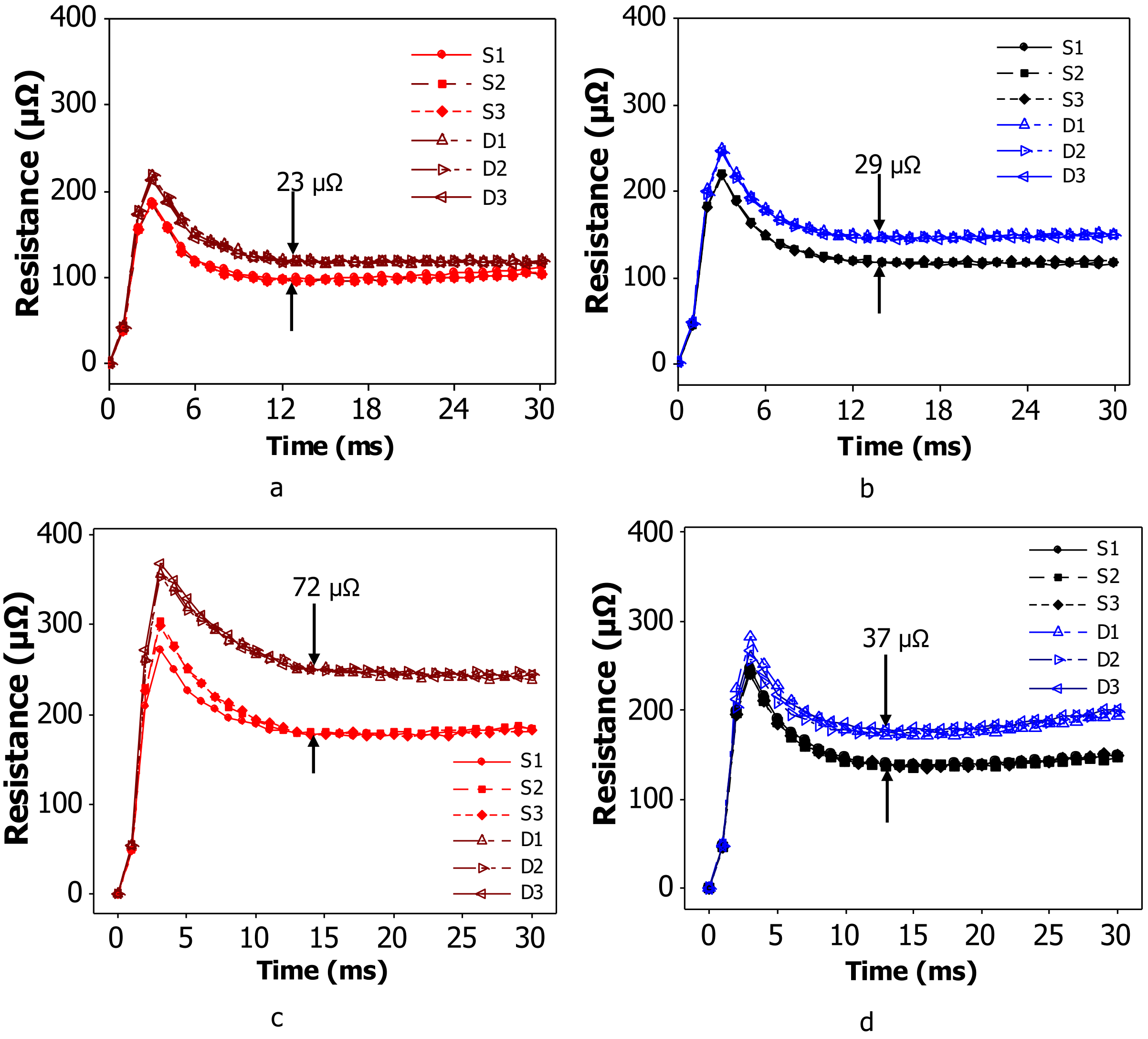

Figure 4-15 Comparison of dynamic resistance profiles for single and double sheets during early stages of RSW process: (a) AlSi (AR), (b) GA (AR), (c) AlSi (HS), (d) GA (HS). S1, S2, S3 are profiles for single sheets, D1, D2, D3 are profiles for double sheets

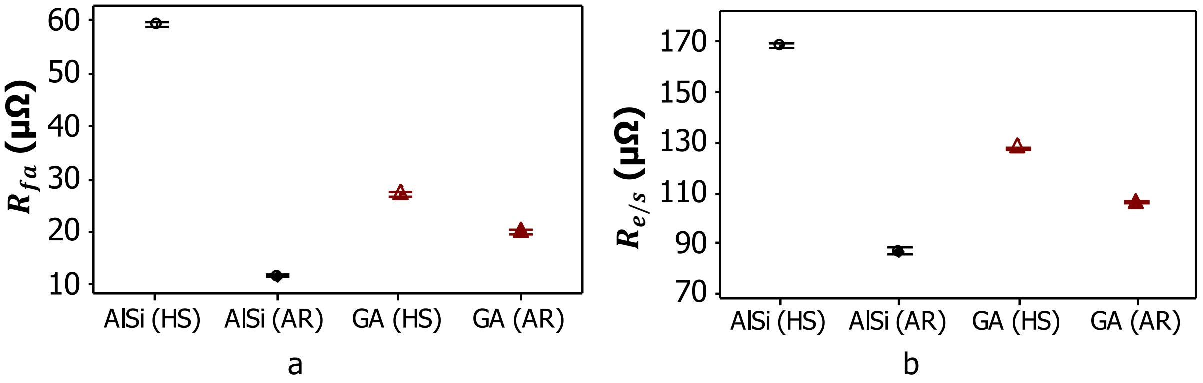

Figure 4-16 Components of resistance of coated specimens (at 95% confidence interval)

From Figure 4-16a it is evident that the faying interface resistance for the HS specimens are higher than for the AR specimens. This is as expected since the surfaces are usually rougher after hot stamping. In the case of AlSi, the coating is entirely transformed into new phases: Fe_2Al_5 and FeAl (107, 108). The hardness of the FeAl phase is between 400 and 520 HV (107, 112), while the hardness of the Fe_2Al_5 is between 900 and 1150 HV (107). However, the hardness of AlSi (AR) coating is between 62 and 68 HV (115). Since the phases after hot-stamping are much harder, apparent contact area in the hot stamped condition will be smaller, causing the contact resistance to increase. For the GA coating, during hot stamping at 900°C the different phases no longer exist (beyond 782°C), but the liquid phase and solid solution of Zn in α-Fe exist. Thus the slight increase in R_{fa} for the GA coated steel after hot-stamping is partly due to higher surface hardness and partly due to increased thickness of the coating layer. The numerical values from Figure 4-16a give more insight into the RSW process. They indicate the relative magnitudes of current required for welding the specimens since nugget formation usually begins from this region (119). This is consistent with the work reported here, where 7.5 kA and 8.5 kA welding currents were required to produce full nugget sizes (5.9 mm) for AlSi (HS) and GA (HS) sheets, while 10.0 kA and 9.0 kA were required to produce similar sized nuggets for AlSi (AR) and GA

(AR) specimens respectively. The dynamic resistance profiles for these welds are also shown in Figure 4-13, where it is seen that the emergence of the stages is consistent with the trend in R_{fa}: for example, stage 4 (beginning of nugget formation) occurred at the shortest time for the AlSi (HS) specimen and longest time for the AlSi (AR) specimen. Figure 40b shows the trend in $R_{e/s}$. The distribution follows similar pattern to R_{fa}: hot stamped materials having higher $R_{e/s}$ values, and AlSi (HS) much higher value than all others.

Figure 4-16b may be useful for predicting the relative rate of electrode degradation since the rate at which degradation (by softening and deformation) occurs depends on the maximum temperature attained at the e/s interface (6). It could also serve as an indicator of likelihood of degradation of the electrodes consequent upon segregation of phases due to high heating rate at the electrode interface.

4.6 Nugget formation and sizes

Figure 4-17 shows nugget sizes for the specimens for various welding currents and 300 ms welding time. For the as-received specimens, no nugget was formed before 6.3 kA current. Using 6.5 kA welding current, 3.5 mm nugget was formed for the GA (AR) specimen. The least current that generated a nugget (of 1.5 mm size) for the AlSi (AR) specimen was 7.5 kA. For the hot-stamped materials, nuggets were formed with much smaller current values as shown in Figures 4-17a and 4-17b for as-received and hot-stamped materials respectively. The horizontal lines shown on Figures 4-17a and 4-17b at 4.38 mm (given by $4\sqrt{t}$, where *t* is the sheet thickness) represent the minimum weld size specified by AWS/SAE/D8.9-2012 standard (81), for a satisfactory weld. It can be seen therefore from Figure 4-17a that lower welding current is required to form satisfactory welds for the GA (AR) than for the AlSi (AR) coated materials.

From Figure 4-17b, the reverse is true, in that after hot-stamping, the AlSi (HS) specimen required lower welding current than the GA (HS) specimen since the former now possesses higher electrical resistance. Generally, trends in current requirement are predictable from trends in dynamic resistance profile presented in Figure 4-13.

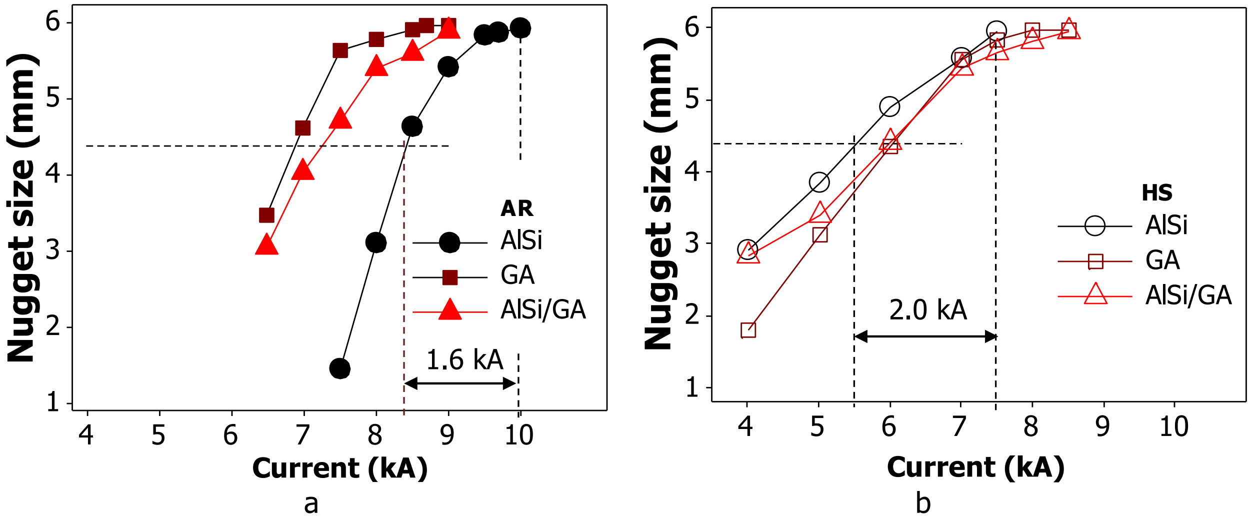

Figure 4-17 Nugget sizes versus current for: (a) as-received and (b) hot-stamped materials

From the current required to form the minimum acceptable nugget size to the maximum current before expulsion begins (nugget sizes for expulsion currents are not shown in Figure 4-17), the welding current range is obtained. As shown in Figure 4-17a, the welding current range for AlSi (AR) is 1.6 kA. Similarly, the welding current ranges for GA (AR) and AlSi/GA (AR) are 2.2 kA and 1.8 kA respectively. Current ranges for the HS specimens shown in Figure 4-17b are 2.0 kA for AlSi (HS) and 2.5 kA for both GA (HS) and AlSi/GA (HS). Therefore, HS specimens exhibited wider current ranges than AR specimens. Also, the GA specimens exhibited wider current range than the AlSi specimens in both AR and HS conditions. Also, as shown in Figure 4-17, all the specimen types attained similar optimal nugget sizes, even though at different welding currents and different conditions (AR and HS).

4.7 Hardness profiles

Figures 4-18a and 4-18b show hardness profiles for the welded AR and HS specimens respectively. BM hardness appears fairly similar for AR specimens. But from hardness mapping results stated earlier, BM hardness for the GA (AR) is slightly higher with a mean value of 184 HV compared with a mean value of 164 HV for AlSi (AR). Along the fusion zone (FZ), hardness lies within similar average. For the HS specimens, hardness values are similar in the BM region (as presented earlier), and along the FZ. Due to transformation to martensite after hot-stamping, the hardness of the BM increased. But during RSW, softening occurred at the sub-critical heat affected zone (SCHAZ) due to tempering of martensite, making the SCHAZ exhibit the lowest hardness values in the profiles for all the specimens as shown in Figure 4-18.

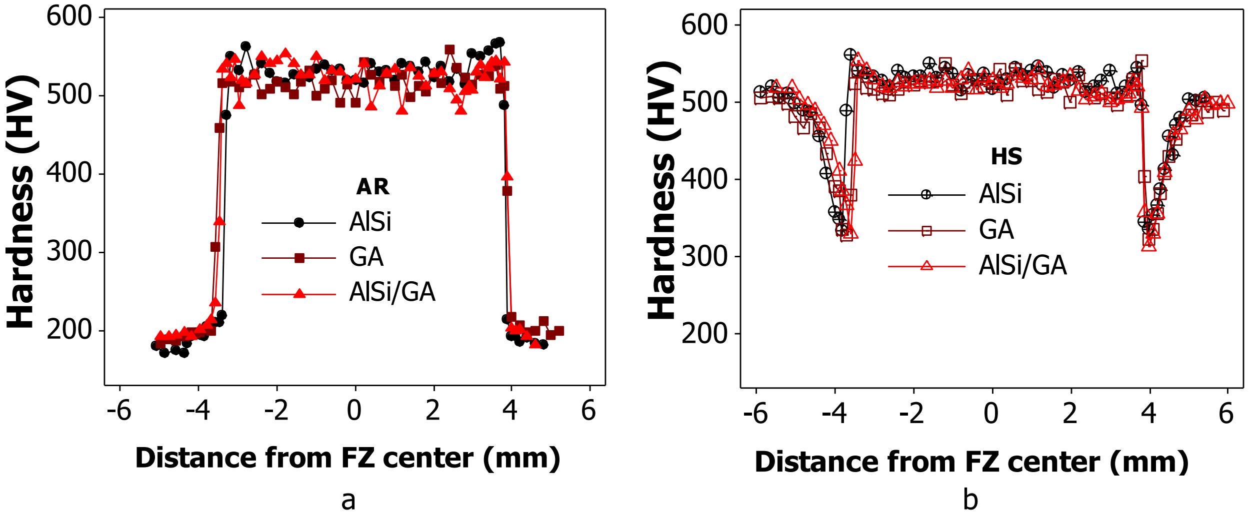

Figure 4-18 Hardness profiles for RSW specimens in: (a) as-received and (b) hot-stamped conditions

4.8 Tensile-shear load and failure mode

Figure 4-19 shows the tensile-shear (TS) peak loads against current. It is seen that the peak load for the AlSi and GA coated specimens are identical, but attained at different welding currents. Also, peak the HS specimens attained higher peak loads than AR specimens. This is attributed to their stronger martensite microstructure compared to the pearlite and ferrite microstructure in AR specimens. From the (AR) portion of Figure 4-19 (which also indicates the failure mode), the earliest pull-out (PO) mode failure for AlSi (AR) occurred at 8.5 kA, while for the GA (AR) and AlSi/GA (AR), earliest PO failure mode was at 7.5 kA. Seeing that the peak load for AlSi (AR) at 8.5 kA is lower than for GA (AR) at 7.5 kA, it can be asserted that the AlSi exhibits PO failure mode at lower load than GA coated specimen. Further, comparing this AR portion of Figure 4-19 with Figure 4-17a, (nugget size vs current), it will be noticed that AlSi (AR) welded at 8.5 kA and GA (AR) welded at 7 kA have similar nugget size (4.5 mm) and similar failure load. However, the AlSi (AR) exhibited PO failure mode while the GA (AR) exhibited interfacial failure (IF). PO failure mode is desirable and preferred for RSW joints (73, 76) because of shock reduction and total energy absorption capability (even though energy calculation is limited to peak load in practice). Transition from IF to PO failure mode is governed by ductility around the joint, which promotes necking and subsequent PO failure (120).

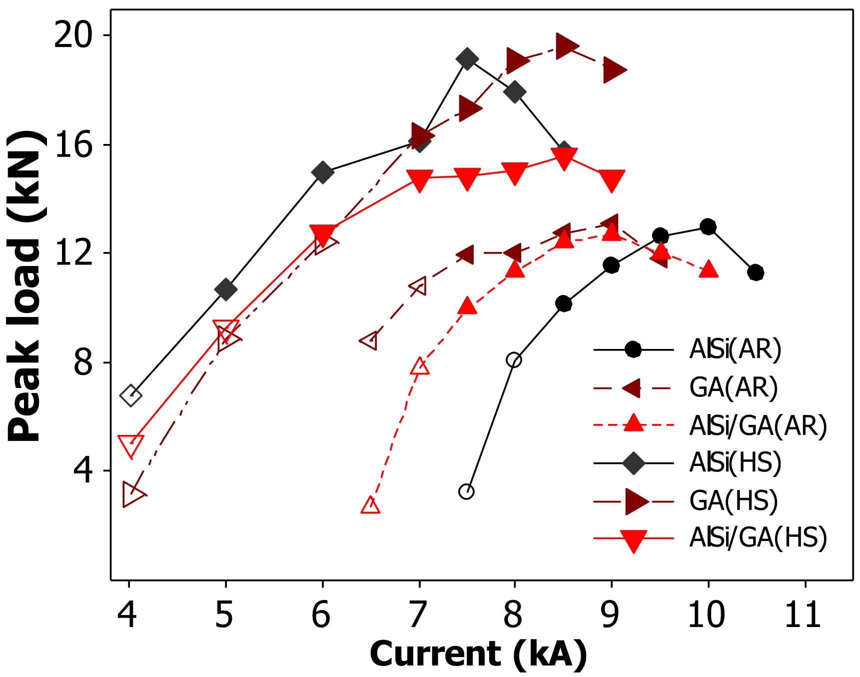

Figure 4-19 Tensile-shear loads for as received (AR) and hot-stamped (HS) materials. The hollow symbols represent interfacial failure (IF), while the filled symbols represent pull-out failure (PO)

Also for the HS specimens, transition from IF to PO failure mode occurred at lower load and lower welding current for the AlSi (HS) than GA (HS). The earliest recorded PO failure occurred for AlSi (HS) at 9.9 kN and 5 kA welding current. For GA (HS) it occurred at 16.1 kN and 7 kA, while for AlSi/GA, earliest PO failure occurred at 12.4 kN and 6 kA. Early transition from IF to PO mode in the AlSi coated specimens can be attributed to relative softness and the causes of softness will be discussed in relation to the effect of alloy composition and heat input.

4.8.1 Effects of alloy composition

It was stated earlier that the AlSi (AR) material has a hardness of 20 HV less than the GA (AR) material. This should contribute significantly to the early failure mode transition exhibited by the AlSi (AR) specimen. The GA coated specimen is composed of significantly higher amounts of Si, Cu and Ni, as displayed in Table 3-1. These elements are known to increase hardness of ferrite phase. Therefore the GA coated specimen should be expected to exhibit greater resistance to plastic deformation at the joint, which leads to delayed failure mode transition. Moreover, Si is known to retard cementite growth, thereby resisting softening in the HAZ (121) and increasing hardness of tempered martensite at all tempering temperatures (122). Figure 4-20 shows the effects of some alloying elements on hardness (i.e. softening) during heat treatment of steel at 316°C (600°F); the effect of Si is seen to be very significant.

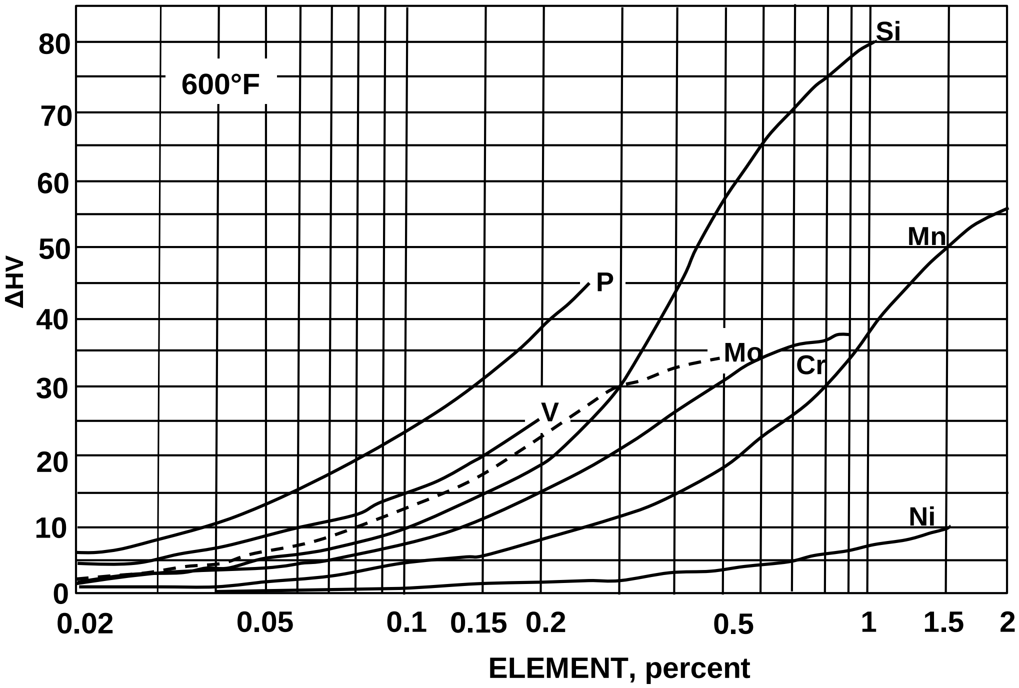

Figure 4-20 Effect of elements on the hardness of martensite tempered at 316°C (600°F) for 1 hour. ΔHV is the measure of resistance to softening (122)

The chemistry of the GA coated specimen also shows significantly higher proportion of molybdenum and vanadium, which are strong carbide formers and high temperature alloying elements, even though their concentrations are small (which is usually the case for micro-alloying elements). They are known to cause work hardening and retard HAZ softening (31, 33, 123). The potency of some alloying elements (including molybdenum and vanadium) in retarding softening during high temperature tempering of martensite are shown in Figure 4-21. Although the AlSi coated specimen is richer in Cr, the contribution of Cr to hardness or strength is minimal relative to other elements (31), and its effect in retarding tempering of martensite is less the effects of either vanadium or molybdenum.

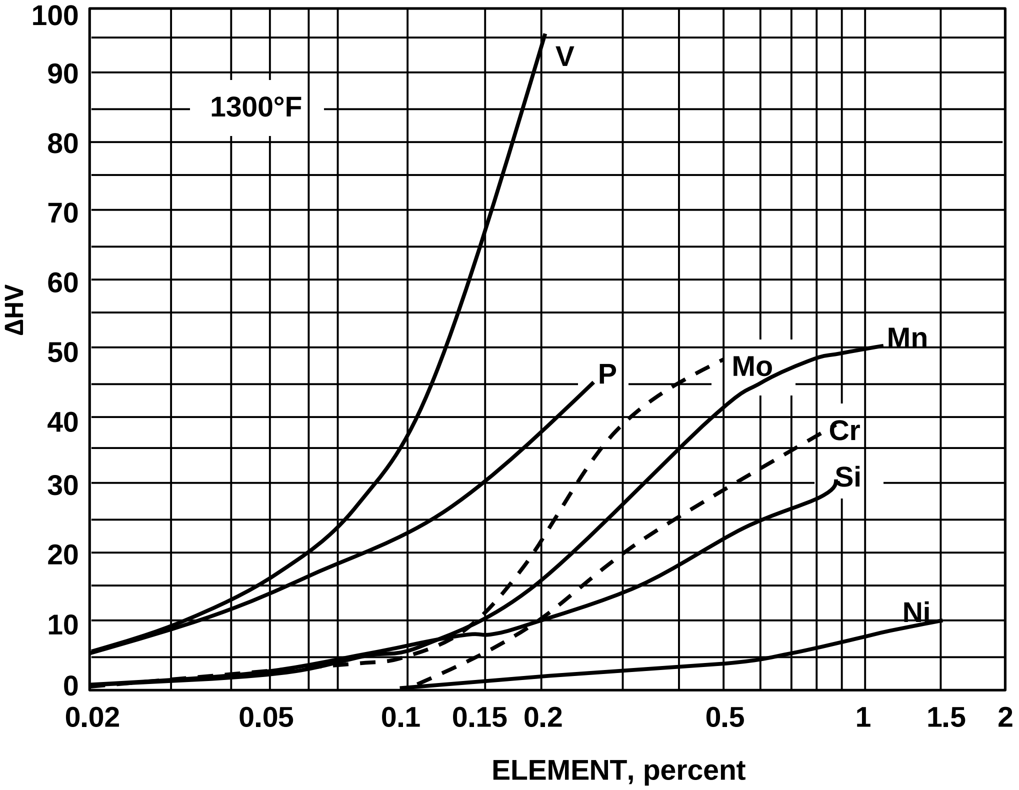

Figure 4-21 Effect of elements on the hardness of martensite tempered at 704°C (1300°F) for 1 hour. ΔHV is the measure of resistance to softening (122)

4.8.2 Effect of heat input during welding

HAZ softening increases with increasing heat input. To compare the heat input during RSW of AlSi and GA coated specimens, the heating rate required to generate equivalent nugget sizes were evaluated (the values were obtained from the data acquisition system, and could also be computed using equation 2.1 and the dynamic resistance profiles). The nugget sizes chosen are those within the welding range. Figure 4-22a shows heating rates required to generate 4.5 mm nugget for AlSi (AR) and GA (AR) specimens, and Figure 4-22b shows heating rates required to generate 5.9 mm nugget for AlSi (AR) and GA (AR) specimens. It is seen that in both cases, heating rate was higher for the AlSi (AR) coated specimens.

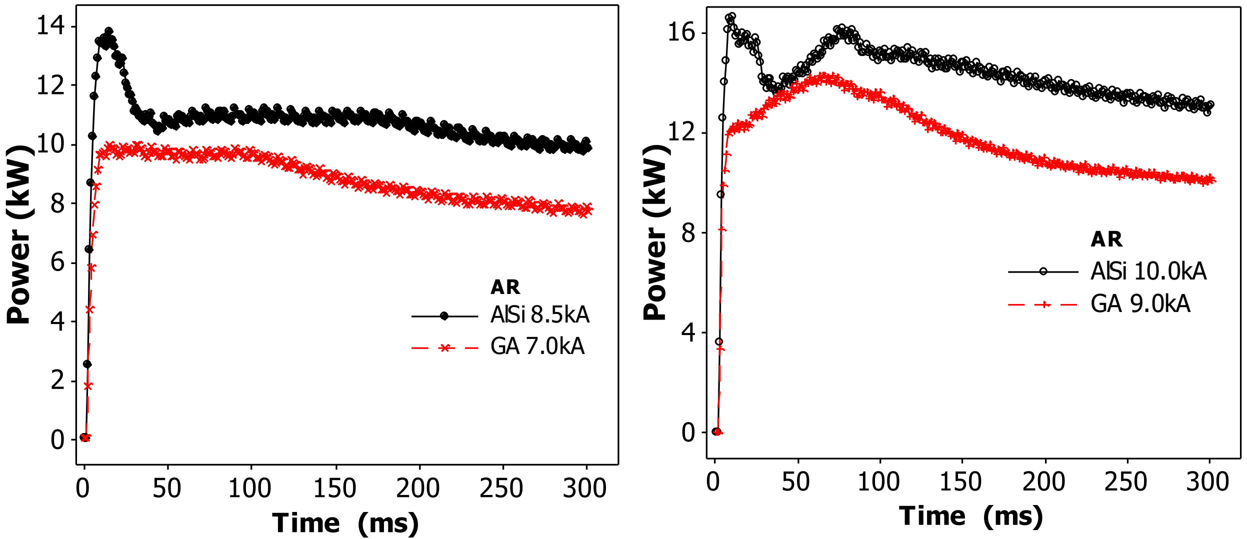

a

b

Figure 4-22 Comparing heating rate required for AlSi (AR) and GA (AR) for generating equivalent sized nuggets: (a) 4.5 mm nugget and (b) 5.9 mm nugget.

Similar analyses were done for the hot stamped specimens, and the results are presented in Figure 4-22. It is seen that for both as received and hot stamped specimens the heating rate is higher for the AlSi coated specimens. The combined effects of the difference in heating rate and alloy composition are responsible for the difference in failure mode transition, because they enhance ductility of the AlSi coated specimens more than the GA coated specimens, which consequently resulted in early transition from IF to PO failure mode in AlSi coated specimens.

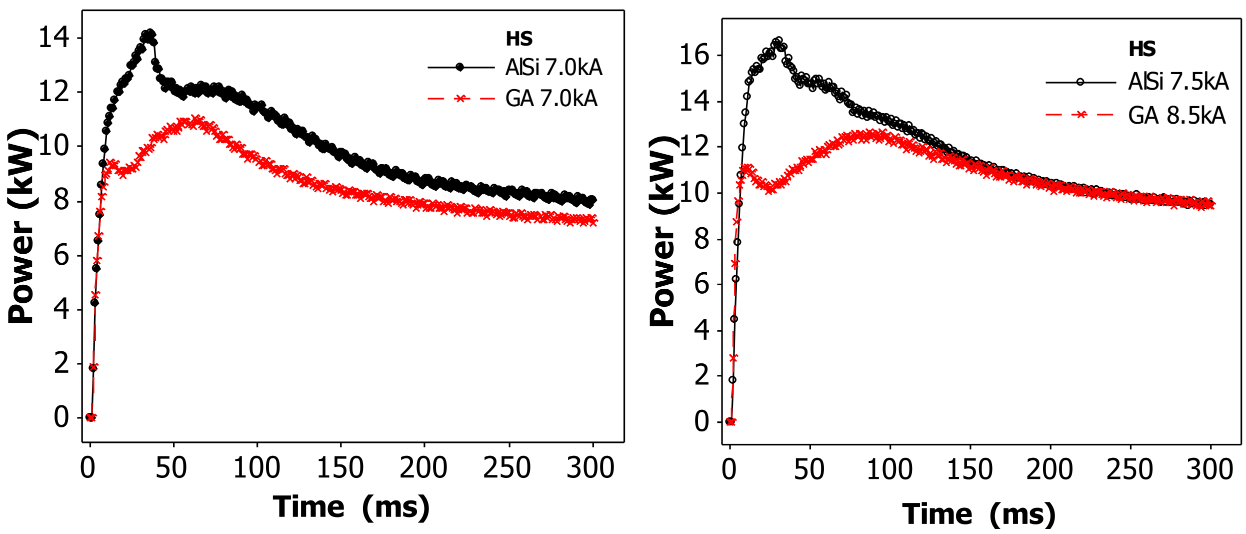

a

b

Figure 4-23 Comparing heating rate required for AlSi (HS) and GA (HS) for generating equivalent sized nuggets: (a) 5.6 mm nugget and (b) 5.9 mm nugget.

Figure 4-24 shows typical failure modes: IF and PO, associated with as-received materials. For the PO failure mode shown, necking prior to failure of the AlSi specimen is obvious, but not for the GA specimen. Figure 4-25a shows typical PO failure mode in AlSi (HS) and GA (HS) specimens while Figure 4-25c shows IF failure mode. Of particular interest is the failure mode shown in Figure 4-25b, for AlSi/GA (HS) dissimilar welds, where failure initiated on the AlSi side and the pull-out button remained on the GA sheet for all the specimens. This will be discussed in more details in section 4.10.

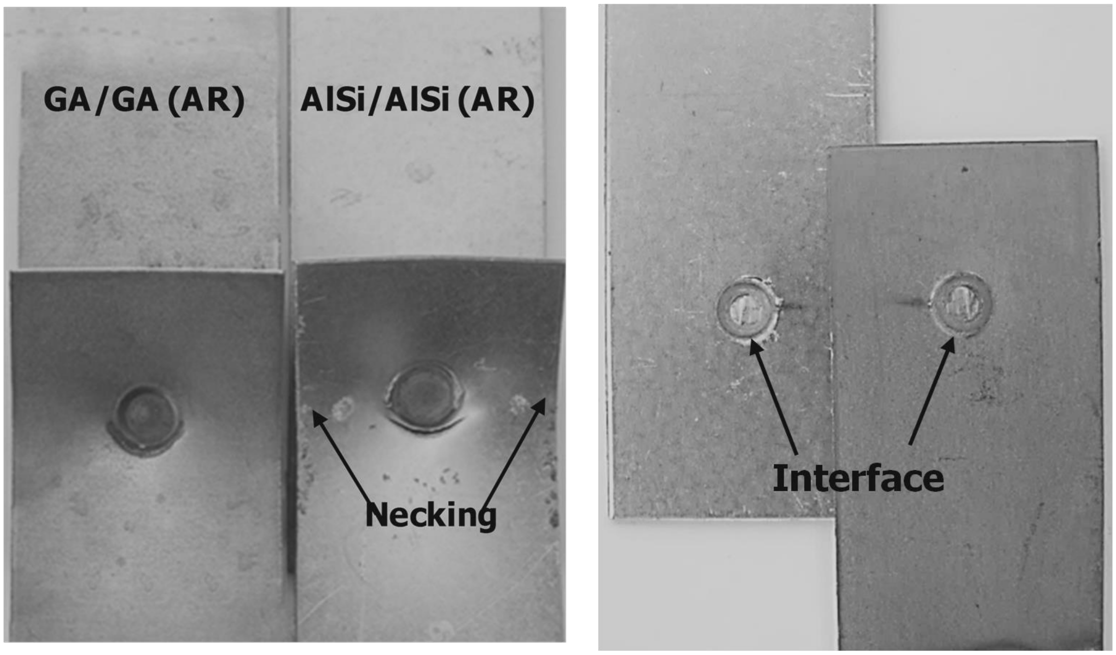

Pull-out failure

Interfacial failure

Figure 4-24 Tensile-shear coupons showing pull-out and interfacial failure modes in as-received coupons. More pronounced necking seen in pull-out mode on AlSi (AR) than GA (AR).

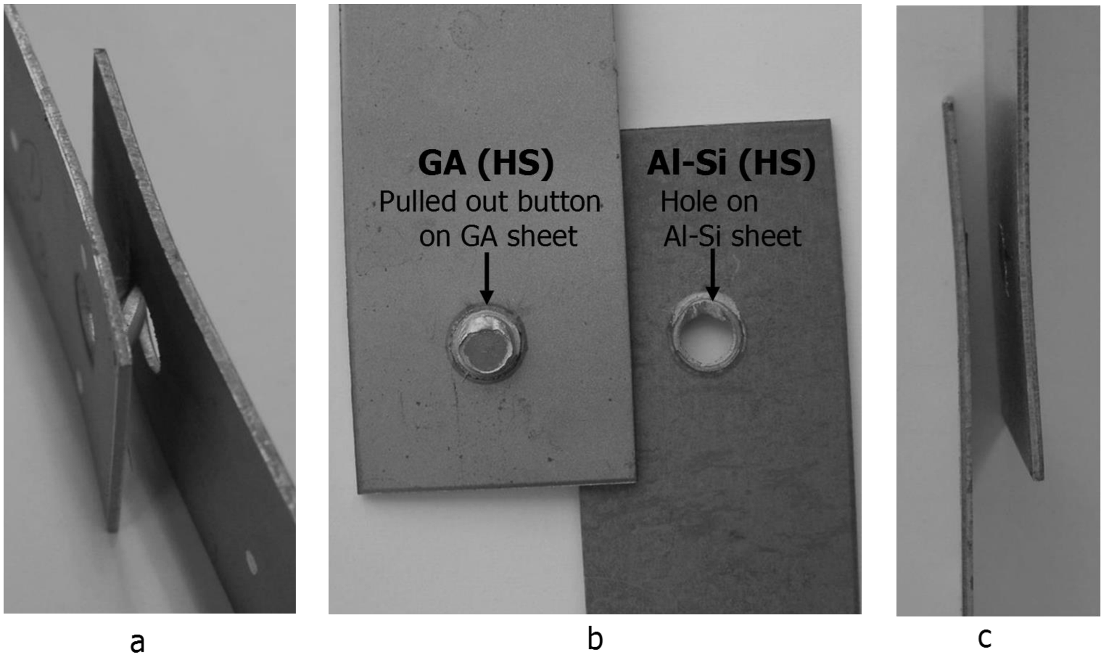

Figure 4-25 Tensile-shear failure modes of hot-stamped specimens: (a) pull-out mode with button pull-out from both sheets, (b) pull-out mode with button attached to the GA sheet while a hole is left on the AlSi sheet in AlSi/GA (HS) dissimilar welds, and (c) interfacial mode.

4.8.3 Tensile load correlations

It is known that the strength of RSW joint strongly correlates with the nugget size (73, 79). In attempt to determine the effect of coating on load versus nugget size relationship, failure load versus nugget size for all the specimens were plotted together on a single chart, shown in Figure 4-24 (AlSi/GA combinations are not included). It is shown that all the AR materials lie along a narrow belt, indicating that they can be correlated empirically by a linear law. A trendline was calculated and displayed with the data as shown. The R^2 value (coefficient of determination) for this trendline is 0.97, indicating very satisfactory correlation. Similar exercise was also conducted for the hot-stamped material, and a trendline with an R^2 value of 0.99 was obtained. These results show that coating type is not a necessary factor for predicting or designing for strength of RSW joint, provided the weldment is free from other phases influenced by the coating as is the case in this work.

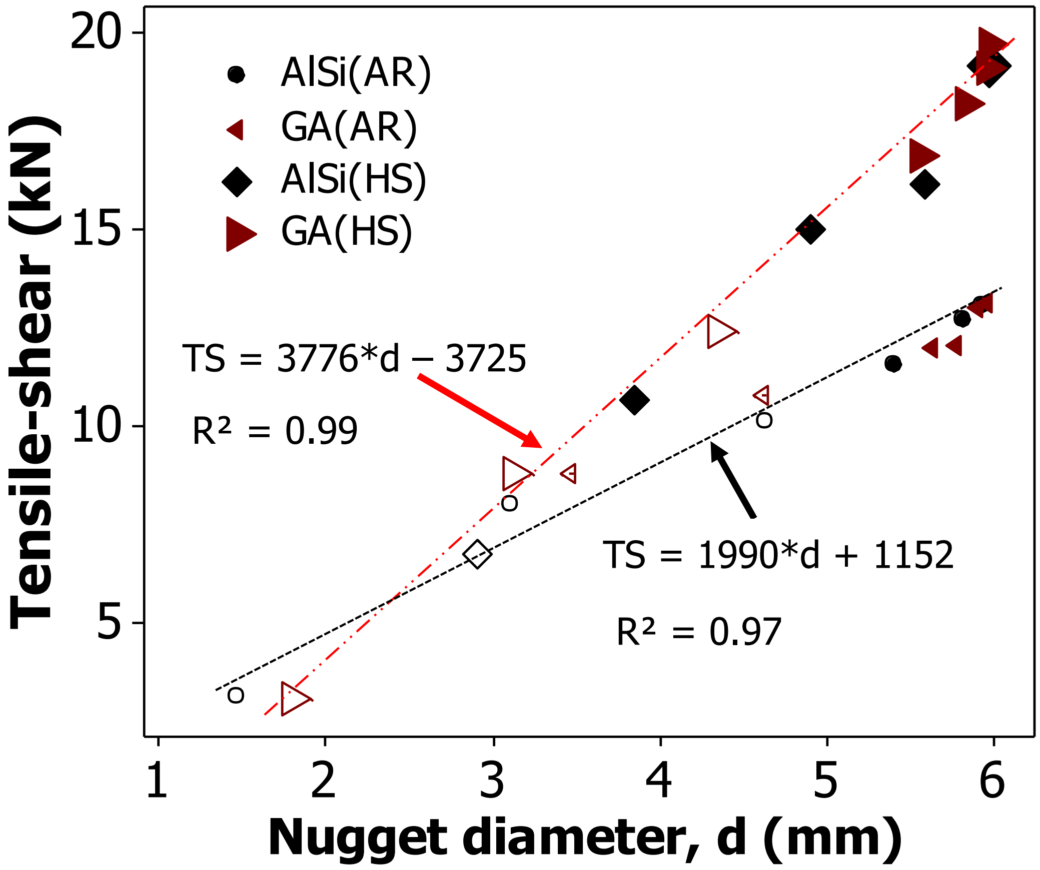

Figure 4-26 Tensile-shear load versus nugget size correlations: hollow symbols are IF mode failed coupons and filled symbols are PO mode failed coupons.

4.9 Energy absorption

In the static (or quasi-static) mode, high energy absorption of RSW joint could be a good measure of formability, e.g. for tailor welded blanks (TWB). Figure 4-27 shows the energy absorption in static mode for as-received as well as hot-stamped materials, for tensile shear specimens. It shows that the AlSi (AR) specimens exhibit the highest energy absorption capacity. This could be due to the lower hardness of the AlSi (AR) BM, which enabled the specimen to undergo higher elongation (without reduction in peak load). There is no significant difference in energy absorption between the AlSi and GA coated specimens in the hot-stamped condition. This is particularly important since these materials are designed for applications in their hot-pressed forms. The AlSi/GA performed poorly, exhibiting the least values of energy absorption both in as-received and hot-stamped conditions. This poor performance is due to the lower peak loads and lower elongations exhibited by the AlSi/GA combinations in both as-received and hot-stamped conditions.

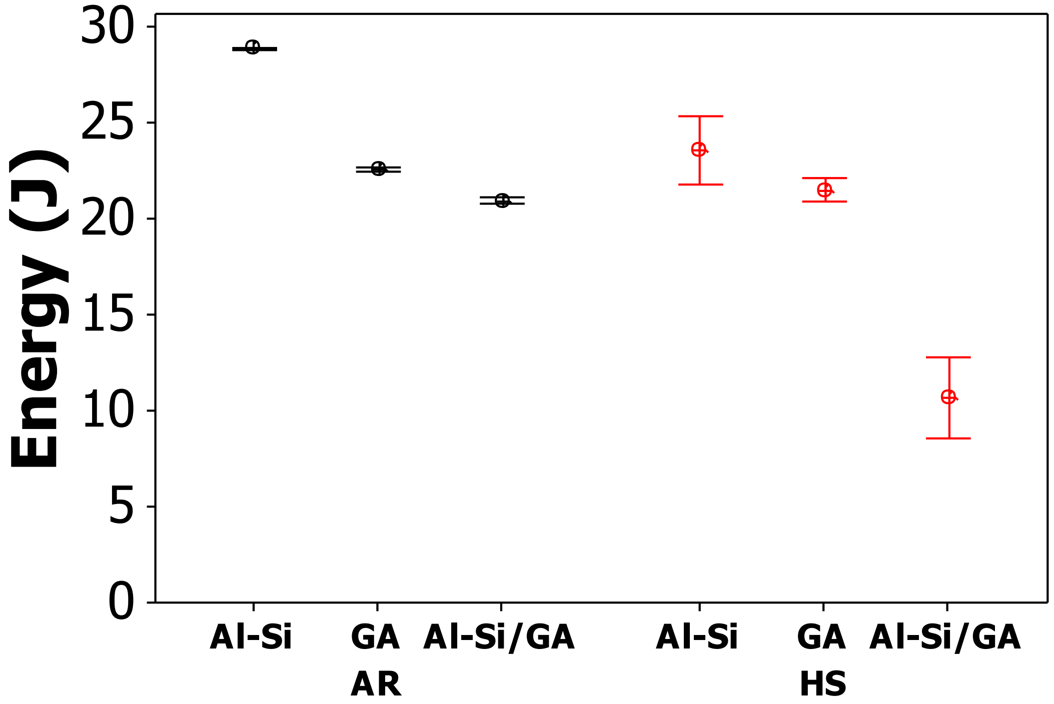

Figure 4-27   Energy absorption for as-received (AR) and hot-stamped (HS) specimens.

4.10 AlSi/GA (HS) specimen

The tensile load result in Figure 4-19 shows that the AlSi/GA (HS) specimen performed very poorly. For the failure mode, all AlSi/GA (HS) specimens that failed in PO mode had their button pulled out from the AlSi (HS) sheet as shown in Figure 4-25b. Failure initiated on the AlSi sheet in all the cases. This specimen also exhibited the poorest performance in energy absorption measurement shown in Figure 4-27. To determine the cause of this peculiar poor behaviour hardness mapping was made over an area covering the fusion zone and HAZ. Indentations were spaced 200 µm parallel to the faying surface on both the GA (HS) and AlSi (HS) side, and 200 µm apart across the sheet thickness. The hardness contour map is shown in Figure 4-28, revealing that the AlSi side exhibited significantly lower hardness value than the GA coated sheet after welding. This phenomenon is attributed to the disparity in electrical and thermal properties associated mainly with the different coatings, which caused heat imbalance during RSW of the dissimilar sheets. It will be recalled that to generate equivalent sized nuggets the AlSi (HS) coated specimens required higher heating rate than GA (HS) coated specimens. During dissimilar weld combinations of AlSi/GA, the AlSi sheet was obviously subjected to higher heating rate, which resulted in higher HAZ softening as seen in Figure 4-28. Also, the results for nugget sizes showed that the AlSi (HS) developed nugget at lower currents than the GA (HS). Therefore when both sheets are stacked together for RSW, melting commenced on the AlSi (HS) sheet earlier. This caused deeper indentation on the AlSi (HS) side and displacement of the prior interface location towards the AlSi (HS) as shown in Figure 4-29. Consequently, the GA (HS) side holds a higher fraction of the nugget while the AlSi (HS) side is left with less material. The softer sub-critical heat affected zone (SCHAZ) now forms a larger fraction of material surrounding the nugget on the AlSi (HS) side, as a result of this displacement. Thus, it is easier for cracks to initiate and propagate through the AlSi (HS) side of the specimen as exhibited by the AlSi/AG (HS) dissimilar weld specimens.

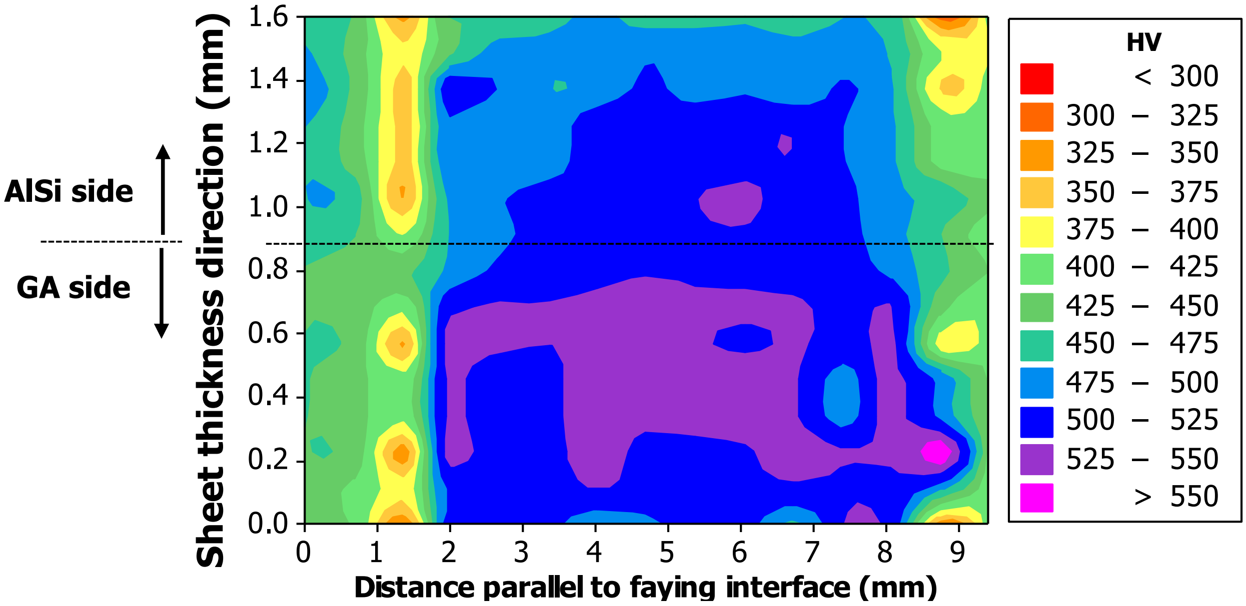

Figure 4-28 Hardness map enclosing the fusion zone and HAZ of AlSi/GA (HS) specimen. The dotted horizontal line is in the position of the faying interface.

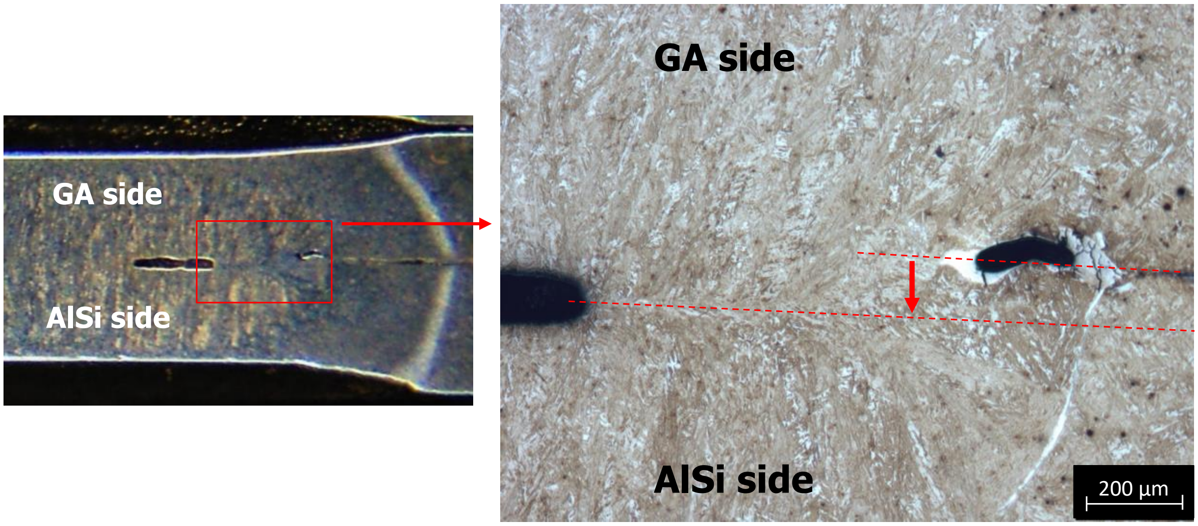

Figure 4-29 AlSi/GA (HS) specimen illustrating displacement of prior faying interface.

5 Summary and Conclusions

5.1 Summary

Other than protecting steel from effects of harsh service and processing environments, coatings have been known to be responsible for other (unpleasant) effects, such as: generating visible cracks during welding of Zn coated steel (LME effect), and sometimes, forming inclusions of other phases in fusion zone during welding of AlSi coated steel. This thesis presents new findings on the influence of AlSi and GA coatings on processing parameters and joint performance during resistance spot welding of ultra-high strength steel, Usibor, a press hardenable steel. The highlights of the findings are presented in the concluding section.

5.2 Conclusions

5.2.1 Dynamic resistance characterization and coating electrical properties

1. Dynamic resistance principles was applied for computing the magnitude of resistance associated with key sections in the set-up for RSW, and values obtained showed that in all cases, the electrode/sheet interface resistance is significantly higher than both the faying interface (i.e. sheet/sheet interface) and substrate resistances.

2. The existence of an initial heating stage prior to surface film breakdown during RSW was established. This makes the resistance values obtained from static measurement significantly different from the initial peaks obtained at the beginning of the dynamic resistance profile. Thus, static resistance values are not reliable for investigating the influence of electrical resistance during RSW; dynamic resistance measurements should be employed.

3. In as received condition, higher electrical resistance is associated with the GA coating, but after hot stamping, the AlSi coating exhibited higher electrical resistance. This occurred due

to the new high electrical resistivity phases formed after hot stamping the AlSi coated specimens. These new phases are also known to possess much higher hardness, which enhances contact resistance.

5.2.2 Coating influence on RSW parameters and joint properties

1. The coating significantly influenced the welding current requirements due to the difference in electrical resistance associated with the different coatings, and the GA coated steel exhibited wider welding current range than the AlSi coated steel in both as received and hot stamped conditions.
2. Heating rate required to form similar sized nugget was higher for AlSi than the GA coated specimens in both as received and hot stamped conditions.
3. AlSi and GA coated specimens attained similar peak nugget sizes and therefore exhibited similar peak loads, since peak load is a function of FZ size and both specimen types possess similar microstructures.
4. AlSi coated specimen exhibited failure mode transition from IF to PO at lower nugget size and lower load than the GA coated specimen in both as-received and hot-stamped conditions. This is as a result of the difference in alloy chemistry and heating rate during RSW.
5. In the as received condition, AlSi coated specimens exhibited higher energy absorption than the GA coated specimens. However, in the hot stamped form, energy absorption for the AlSi and GA specimens are similar.
6. The combination of coating types in the form AlSi/GA specimen exhibited the poorest performance due to difference in resistances of the coatings which caused thermal imbalance during RSW and consequently, poor joints.

5.3 Recommendations

The findings from this research have thrown more light into the influence of coatings on RSW process and joint performance. Based on these findings and the limited scope of this work, recommendations for further work are listed below.

1. Investigations of heat transfer properties of the coatings will be helpful (in conjunction with electrical resistance values) for developing models for predicting thermal profiles and microstructures around the weldment. This will be useful for predicting mechanical behaviour of the joint and optimizing RSW parameters.
2. Effects of coating thickness and other welding parameters such as hold time, upslope and downslope, can be studied determine optimal coating thickness for a more robust welding practice for each coating.
3. Study of the influence of the coating on mechanical performance at different strain rates will be useful, seeing that different RSW heating rates and chemistries are associated with the different coatings
4. Investigation on methods for improving the performance of the AlSi/GA dissimilar welded joint will be beneficial since this type of joint is unavoidable in the automotive industry. Probable methods for improvement include:
    i. Using sheet metals having different thicknesses of coatings to bridge the gap between resistances associated with coatings.
    ii. Using multiple pulses during RSW such that the earlier pulse(s) are aimed at eliminating the coating around the weldment before the main pulse(s) for fusion.

References

1. Tamarelli CM (2011) The evolving use of advanced high-strength steels for automotive applications. (American Iron and Steel Institute, Southfield, Michigan).
2. WorldAutoSteel (2011) Future steel vehicle-final engineering report. p 886.
3. Parezanović I (2005) Selective oxidation and segregation in commercial steels and model alloys (Tools for improving the surface wettability by liquid Zn during hot dip galvanizing. Doctoral Thesis (RWTH, Aachen).
4. Shibli SMA, Meena BN, & Remya R (2015) A review on recent approaches in the field of hot dip zinc galvanizing process. *Surface and Coating Technology* 262:210-215.
5. Hernandez VHB, Okita Y, & Zhou Y (2012) Second pulse current in resistance spot welded TRIP steel - effects on the microstructure and mechanical behavior. *Welding Journal* 91(10):278-285.
6. Williams NT & Parker JD (2004) Review of resistance spot welding of steel sheets Part 2 Factors influencing electrode life *International Materials Review* 49(2):77-108.
7. Brauser S, Pepke LA, Weber G, & Rethmeier M (2010) Deformation behaviour of spot-welded high strength steels for automotive applications. *Materials Science and Engineering: A* 527(26):7099-7108.
8. Chen Z, Shi Y, Jiao B, & Zhao H (2009) Ultrasonic nondestructive evaluation of spot welds for zinc-coated high strength steel sheet based on wavelet packet analysis. *Journal of Materials Processing Technology* 209(5):2329-2337.
9. Ji C-W*, et al.* (2014) Effects of surface coating on weld growth of resistance spot-welded hot-stamped boron steels. *Journal of Mechanical Science and Technology* 28(11):4761-4769.

10. Fan DW & Cooman BCD (2012) State-of-the-knowledge on coating systems for hot stamped parts. *Steel research int.* 83(9999):1-22.

11. Lee CW, Fan DW, Sohn IR, Lee S-J, & De cooman BC (2012) Liquid-metal-induced embrittlement of Zn-coated hot stamping steel. *Metallurgical and Materials Transaction A* 43A:5122-5127.

12. Kondratiuk J, Kuhn P, Labrenz E, & Bischoff C (2011) Zinc coatings for hot sheet metal forming: Comparison of phase evolution and microstructure during heat treatment. *Surface and Coatings Technology* 205(17–18):4141-4153.

13. Beal C, Kleber X, Fabregue D, & Bouzekri M (2012) Embrittlement of a zinc coated high manganese TWIP steel. *Materials Science and Engineering: A* 543(0):76-83.

14. Cho L, Kang H, Lee C, & De Cooman BC (2014) Microstructure of liquid metal embrittlement cracks on Zn-coated 22MnB5 press-hardened steel. *Scripta Materialia* 90–91(0):25-28.

15. Gaul H, Weber G, & Rethmeier M (2011) Influence of HAZ cracks on fatigue resistance of resistance spot welded joints made of advanced high strength steels. *Science and Technology of Welding and Joining* 16(5):440-445.

16. Yan B, Zhu H, Lalam S, Baczkowski S, & Coon T (2004) Spot weld fatigue of dual phase steels. *SAE Technical Paper 2004-01-0511* (1):1-8.

17. Silver RFd & Vieira SL (2009) Influence of the coating type on electrode life in spot welding. *Welding International* 23(3):186-192.

18. Hu X, *et al.* (2010) Effects of steel coatings on electrode life in resistance spot welding of galvannealed steel sheets. *Materials Transactions* 51(12):2236-2242.

19. Zou J, Zhao Q, & Chen Z (2009) Surface modified long-life electrode for resistance spot welding of Zn-coated steel. *Journal of Materials Processing Technology* 209(8):4141-4146.

20. Kim C, Kang MJ, & Park YD (2011) Laser welding of Al-Si coated hot stamping steel. *Procedia Engineering* 10(0):2226-2231.

21. Lee J-H, Kim J-D, Oh J-S, & Park S-J (2009) Effect of Al coating conditions on laser weldability of Al coated steel sheet. *Transactions of Nonferrous Metals Society of China* 19(4):946-951.

22. Vierstraete R & Black G (2014) Industrial Laser Solutions. (ArcelorMittal), pp 10-14.

23. Park TJ, *et al.* (2011) Effect of Al–Si coating layer on the penetration and microstructures of ferritic stainless steel, 409L GTA welds. *Journal of Materials Processing Technology* 211(3):415-423.

24. Bhat SP (2008) Advances in high strength steel designs for automotive applications, Arcelor Mittal presentation. *Great Designs in Steel Seminar*, (AUTOSTEEL).

25. Naderi M (2007) Hot stamping of ultra high strength steels. Doctoral Thesis (RWTH, Aachen).

26. Karbasian H & Tekeya AE (2010) A review on hot stamping. *Journal of Materials Processing Technology* 210:2103-2118.

27. Akerstrom P (2006) Modelling and simulation of hot stamping. Doctoral Thesis (Lulea University of Technology, Lulea, Sweden).

28. Suehiro M, Kusumi K, Miyakoshi T, Maki J, & Ohgami M (2003) Properties of aluminum-coated steels for hot-forming. in *Nippon Steel Technical Report*, pp 1-6.

29. Bardelcik A (2012) High strain rate behaviour of hot formed boron steel with tailored properties. Doctoral Thesis (University of Waterloo, Waterloo).

30. Fristad W (2014) Coil applied coating for press-hardening steel. (Great designs in steel), pp 1-22.

31. Maalekian M (2007) The effects of alloying elements on steels (I). (Christian Doppler Laboratory for Early Stages of Precipitation-Technische Universität Graz), pp 1-36.

32. Lancaster JF (1992) *Handbook of structural welding: Processes, materials and methods used in welding of major structure, pipelines and process plant* (Abington Publication, Abington, Cambridge).

33. Bain EC (1939) *Functions of the alloying elements in steel* (American Society for Metals, Cleveland, OH).

34. Thelning K-E (1984) *Steels and its Heat Treatment* (Butterworth-Heinemann, Thelning, UK (1984).) Second Ed.

35. Samans CH (1953) *Engineering Metals and Their Alloys* (The Macmillan Company, New York).

36. Lampman S ed (1997) *Weld integrity and performance* (ASM International).

37. Kurc-Lisiecka A & Kciuk M (2013) The influence of chemical composition on structure and mechanical properties of austenitic Cr-Ni steels. *Journal of Achievements in Materials and manufacturing Engineering* 61(2):210-215.

38. Hulka K (2003) The role of Niobium in multiphase-steel. *Metal*:1-9.

39. Aliakbarzadeh H, Mirdamadi S, & Tamizifar M (2010) Effect of low Zr addition on microalloyed cast steel. *Materials Science and Technology* 26(11):1373-1376.

40. El-Faramawy HS, Ghali SN, & Eissa MM (2012) Effect of titanium addition on behavior of medium carbon steel. *Journal of Minerals and Materials Characterization and Engineering* 11:1108-1112.

41. Marder AR (2000) The metallurgy of zinc-coated steel. *Progress in Materials Science* 45(3):191-271.

42. ArcelorMittal (2013) Metallic coated steel-User manual. in *ArcelorMittal Flat Carbon Europe* (Luxemburg).

43. Grabke HJ, Leroy V, & Viefhaus H (1995) Segregation on the surface of steels in heat treatment and oxidation. *ISIJ International* 35(2):95-113.

44. Notowidjojo BD (1990) A study of zinc-nickel galvanized coating of silicon steels. Doctoral Thesis (University of Wollongong).

45. An X, Cawley J, Rainforth WM, & Chen L (2003) A study of internal oxidation in carburized steels by glow discharge optical emission spectroscopy and scanning electron microscopy. *Spectrochimica Acta Part B* 58:689-698.

46. Liu H, *et al.* (2012) Challenges in hot-dip galvanizing of high strength dual phase steel: Surface selective oxidation and mechanical property degradation. *Surface and Coating Technology* 206:3428-3436.

47. Prabhudev S, Swaminathan S, & Rohwerder M (2011) Effect of oxides on the reaction kinetics during hot-dip galvanizing of high strength steels. *Corrosion Science* 53:2413-2418.

48. Nasr JB, Snoussi A, Bradai C, & Halouani F (2008) Optimization of hot-dip galvanizing process of reactive steels: Minimizing zinc consumption without alloy additions. *Materials Letters* 62:3328-3330.

49. Toledo MIS, Assunção FCR, Paciornik S, & Wroblewski T (2003) In situ observation of phase transformations in the Fe-Zn system. *Materials Research* 6(4):529-533.

50. Paramonov AV, Adamov AS, & Chernetsov VY (2010) Production problems in hot dip galvanized metal structures. *Metallurgist* 54(11-12):793-796.

51. Maeda S (1996) Surface chemistry of galvanized steel sheets relevant to adhesion performance. *Progress in Organic Coatings* 28:227-238.

52. Mandal GK, Das SK, Balasubramaniam R, & Mehrotra SP (2011) Evolution of microstructures of galvanised and galvannealed coatings formed in 0.2 wt-% aluminium–zinc bath. *Materials Science and Technology* 27:1265-1270.

53. Tumuluru M (2007) The effect of coatings on the resistance spot welding behavior of 780 MPa dual-phase steel. *Welding Journal* 86:161s-169s.

54. Xhoffer X, Dillen H, & DeCooman BC (1999) Quantitative phase analysis of galvannealed coatings by coulometric stripping. *Journal of Applied Electrochemistry* 29:209-219.

55. Jordan CE & Marder AR (1994) Morphology development in hot-dip galvanneal coatings. *Metallurgical and Materials Transactions A* 25A:937-947.

56. Alpas AT & Inagaki J (1999) Effect of microstructure on fracture mechanisms in galvannealed coatings. *ISIJ International* 40(2):172-181.

57. Eggeler G, Auer W, & Kaesche H (1986) On the influence of silicon on the growth of the alloy layer during hot dip aluminizing. *J Mater Sci* 21:3348-3350.

58. Akdeniz MV, Mekhrabov AO, & Yilmaz T (1994) The role of Si addition on the interfacial interaction in Fe-Al diffusion layer. *Scripta Metallurgica et Materialia* 31(12):1723-1728.

59. Beal C (2012) Mechanical behaviour of a new automotive high manganese TWIP steel in the presence of liquid zinc. Doctoral Thesis (INSAL).

60. Uijl ND (2015) Resistance spot welding of advanced high strength steels. Doctoral Thesis (Delft University of Technology).

61. Yang Y-P, Orth F, Peterson W, & Gould J (2014) Accurate spot weld testing for automotive applications. *Advanced Materials and Processes*:19-22.

62. Zhang H & Senkara J (2006) *Resistance Welding-Fundamentals and Applications* (CRS Taylor and Francis, Boka Raton, Florida).

63. Khan JA, Xu L, Chao Y-J, & Broach K (2000) Numerical simulation of resistance spot welding process. *Numerical Heat transfer, Part A: Application* 37(5):425-446.

64. Association EA (2002) The aluminum automotive manual. (European Aluminum Association), p 19.

65. Keams WH ed (1980) *Resistance and Solid State Welding and other Joining Processes, Welding Handbook* (American Welding Society), Seventh Ed, Vol 3.

66. AWS D8.7-88 SAE, J-1188 (1987) Recommended practices for automotive weld quality—resistance spot welding. (American Welding Society).

67. Miller (2012) *Handbook for Resistance Spot Welding* (Miller Electric Manufacturing Company, IL. USA.) pp 1-16.

68. M. Pouranvari & S. P. H. Marashi (2013) Critical review of automotive steels spot welding: process, structure and properties. *Science and Technology of Welding and Joining* 18(5):361-403.

69. Pouranvari M & Marashi SPH (2012) On failure mode of resistance spot welded DP980 advanced high strength steel. *Canadian Metallurgical Quarterly* 51(4):447-455.

70. Hernandez VHB, Kuntz ML, Khan MI, & Zhou Y (2008) Influence of microstructure and weld size on the mechanical behaviour of dissimilar AHSS resistance spot welds. *Science and Technology of Welding and Joining* 13(8):769-776.

71. Anastassiou M, Babbit M, & Lebrun JL (1990) Residual stresses and microstructure distribution in spot-welded steel sheets: Relation with fatigue behaviour. *Materials Science and Engineering: A* 125(2):141-156.

72. Shi G & Westgate SA (2004) Resistance spot welding of high strength steels. *International Journal for the Joining of Materials*:9-14.

73. Marya M, Wang K, Hector JLG, & Gayden X (2005) Tensile-shear forces and fracture modes in single and multiple weld specimens in dual-phase steels. *Journal of Manufacturing Science and Engineering* 128(1):287-298.

74. Pouranvari M, Mousavizadeh SM, Marashi SPH, Goodarzi M, & Ghorbani M (2011) Influence of fusion zone size and failure mode on mechanical performance of dissimilar resistance spot welds of AISI 1008 low carbon steel and DP600 advanced high strength steel. *Materials & Design* 32(3):1390-1398.

75. Huin T, Dancette S, Fabregue D, & Dupuy T (2016) Investigation of the failure of advanced high strength steels heterogeneous spot welds. *Metals* 6(111):1-19.

76. Noh W, Yoo D, Koh Y, Chung K, & Yang X (2012) Failure evaluation of spot welds for advanced high strength steel sheets. *Key Engineering MAterials* 504-506:131-136.

77. Khan MI, Kuntz ML, & Zhou Y (2008) Effects of weld microstructure on static and impact performance of resistance spot welded joints in advanced high strength steels. *Science and Technology of Welding and Joining* 13(3):294-304.

78. Pouranvari M & Marashi SPH (2011) Failure mode transition in AHSS resistance spot welds. Part I. Controlling factors. *Materials Science and Engineering: A* 528(29–30):8337-8343.

79. Chao YJ (2003) Failure mode of spot welds: interfacial versus pull out. *Science and Technology of Welding and Joining* 8(2):113-117.

80. Chao YJ (2003) Ultimate strength and failure mechanism of resistance spot weld subjected to tensile, shear, or combined tensile/shear loads. *Journal of Engineering Materials and Technology* 125:125-132.

81. ANSI/AWS/SAE/D8.9M (2012) Recommended practice for test method for evaluating the resistance spot welding behavior of automotive steels. in *AWS* (Miami Fl, USA).

82. William D. Callister J & Rethwisch DG (2010) *Materials Science and Engineering: An Introduction* (John Wiley & Sons Inc.) 8th Ed.

83. Eller TK*, et al.* (2016) Plasticity and fracture modeling of the heat-affected zone in resistance spot welded tailor hardened boron steel *Materials Processing Technology* 234:309-322.

84. Jong Y-S*, et al.* (2011) Microstructural evolution and mechanical properties of resistance spot welded ultra high strength steel containing boron. *Materials Transactions* 52(6):1330-1333.

85. Kim EW & Eagar TW (1989) Measurement of transient temperature response during resistance spot welding. *Welding Research Supplement*:303s-312s.

86. Babu SS, Riemer BW, Santella ML, & Feng Z (1998) Integrated thermal-microstructure model to predict the property gradients in resistance spot steel welds. *Proc. 8th Sheet Metal Welding Conf.*, (AWS), pp 1-10.

87. Pouranvari M & Ranjbarnoodeh E (2012) Dependence of the fracture mode on the welding variables in the resistance spot welding of ferrite-martensite DP980 advanced high strength steel. *Materials and Technology* 46(6):665-671.

88. Svensson LE (2004) Prediction of hardness of spot welds in steels. *Welding in the World* 48(11):31-35.

89. Gould JE, Khurana SP, & Li T (2006) Predictions of microstuctures when welding automotive advanced high strength steels. *Welding Journal* 85(5):111s-116s.

90. Kasuya T & Hashiba Y (2007) Carbon equivalent to assess hardenability of steel and prediction of HAZ hardness distribution. (Nippon Steel), pp 53-61.

91. Ion JC, Easterling KE, & Ashby MF (1984) A second report on diagrams of microstructure and hardness for heat affected zones in welds. *Acta metall.* 32(11):1949-1962.

92. Vignier S, Biro E, & Hervé M (2014) Predicting the hardness profile across resistance spot welds in martensitic steels. *Weld World* 2014(58):297-305.

93. Khan MI, Kuntz ML, Biro E, & Zhou Y (2008) Microstructure and Mmchanical properties of resistance spot welded advanced high strength steels. *Materials Transactions* 49(7):1629-1637.

94. Yurioka N, Suzuki H, Ohshita S, & Saito S (1983) Determination of necessary preheating temperature in steel welding. *Supplement to the Welding Journal*.

95. Pouranvari M (2011) Effect of resistance spot welding parameters on the HAZ softening of DP980 ferrite-martensite dual phase steel welds. *World Applied Sciences Journal* 15(10):1454-1458.

96. Kasuya T & Yurioka N (1993) Carbon equivalent multiplying factor for hardenability of steel. *The Welding Journal*:263s-268s.

97. Bhattacharya S & Andrews DR (1974) Significance of dynamic resistance curves in the theory and practice of spot welding. *Welding and Metal Fabrication*:296-301.

98. Dickinson DW, Franklin JE, & Stanya A (1980) Characterization of spot welding behavior by dynamic electrical parameter monitoring. *Welding Research Supplement* 59(6):170s-176s.

99. S. A Gedeon CDS, K. T. Ulrich and T. W. Eagar (1987) Measurement of dynamic electrical and mechanical properties of resistance spot welds. *Welding Research Supplement*:8.

100. Gedeon SA & Eagar TW (1986) Resistance Spot Welding of galvanized Steel: Part II. Mechanism of Spot Weld Nugget Formation. *Metallurgical and Materials Transaction B* 17B:887-901.

101. Ma C, *et al.* (2006) Expulsion monitoring in spot welded advanced high strength automotive steels. *Science and Technology of Welding and Joining* 11(4):40-487.

102. Savage WF, Nippes EF, & Wassell FA (1978) Dynamic contact resistance of series spot welds. *Welding Research Supplement*:43s-50s.

103. Tan W, Zhou Y, & Kerr HW (2002) Effects of Au Plating on Small-Scale Resistance Spot Welding of Thin-Sheet Nickel. *Metallurgical and Materials Transaction A* 33:2667-2676.

104. Tan W, Zhou Y, Kerr HW, & Lawson S (2004) A study of dynamic resistance during small scale resistance spot welding of thin Ni sheets. *J. Phys. D: Appl. Phys.* 37:1998-2008.

105. Xu G, Wen l, & Wang C (2009) Quality monitoring for resistance spot welding using dynamic signals. in *International conference on mechatronics and automation* (IEEE, Changchun, China), pp 1-5.

106. Luo Y, Wan R, Yang Z, & Xie X (2016) Study on the thermo-effect of nugget growing in single-phase AC resistance spot welding based on the calculation of dynamic resistance. *Measurement* 78:18-28.

107. Windmann M, Röttger A, & Theisen W (2014) Formation of intermetallic phases in Al-coated hot-stamped 22MnB5 sheets in terms of coating thickness and Si content. *Surface and Coatings Technology* 246(0):17-25.

108. Danzo II, Houbaert Y, & Verbeken K (2014) Diffusion driven columnar grain growth induced in an Al–Si-coated steel substrate. *Surface and Coatings Technology* 251(0):15-20.

109. Gui Z-x, Liang W-k, Liu Y, & Zhang Y-s (2014) Thermo-mechanical behavior of the Al–Si alloy coated hot stamping boron steel. *Materials & Design* 60(0):26-33.

110. Kobayashi S & Yakou T (2002) Control of intermetallic compound layers at interface between steel and aluminum by diffusion-treatment. *Materials Science and Engineering: A* 338(1–2):44-53.

111. Ghiotti A, Bruschi S, Sgarabotto F, & Bariani PF (2014) Tribological performances of Zn-based coating in direct hot stamping. *Tribology International* 78(0):142-151.

112. Hajaligol MR, Deevi SC, Sikka VK, & Scorey CR (1998) A thermomechanical process to make iron aluminide (FeAl) sheet. *Materials Science and Engineering: A* 258(1–2):249-257.

113. Lilly AC, Deevi SC, & Gibbs ZP (1998) Electrical properties of iron aluminides. *Materials Science and Engineering: A* 258(1–2):42-49.

114. Pithawalla YB, El Shall MS, & Deevi SC (2000) Synthesis and characterization of nanocrystalline iron aluminide particles. *Intermetallics* 8(9–11):1225-1231.

115. Elzanaty H (2014) Effect of different Si content on the mechanical properties in Al-based alloy. *International Journal of Research in Engineering and Technology* 2(7):49-54.

116. Holm R (1967) *Electric Contacts: Theory and Applications* (Spriger-Verlag, Berlin Heidelberg) 4 Ed p 484.

117. Tsalf A (1981) *Combined properties of conductors* (Elsevier Scientific, New York).

118. Wei PS (2014) Effects of electrode contact condition on electrical dynamic resistance during resistance spot welding. *Science and Technology of Welding and Joining* 19(2):173-180.

119. Shen J, Zhang Y, Lai X, & Wang PC (2011) Modeling of resistance spot welding of multiple stacks of steel sheets. *Materials and Design* 32:550-560.

120. Radakovic DJ & Tumuluru M (2008) Predicting resistance spot weld failure modes in shear tension tests of advanced high strength automotive steels. *Welding Research* 87:96s-105s.

121. Li C & G S (1984) The silicon effect in the tempering of martensite in steels. *Journal de physique Colloques* 45(C9):C9-397-C399-401.

122. Grange RA, Hribal CR, & Porter LF (1977) Hardness of tempered martensite in carbon and low alloy steels. *Metallurgical Transactions A* 8A:1775-1784.

123. Campbell FC ed (2008) *Elements of metallurgy and engineering alloys* (ASM International, OH), p 672.